Hall A Status Report - 2004

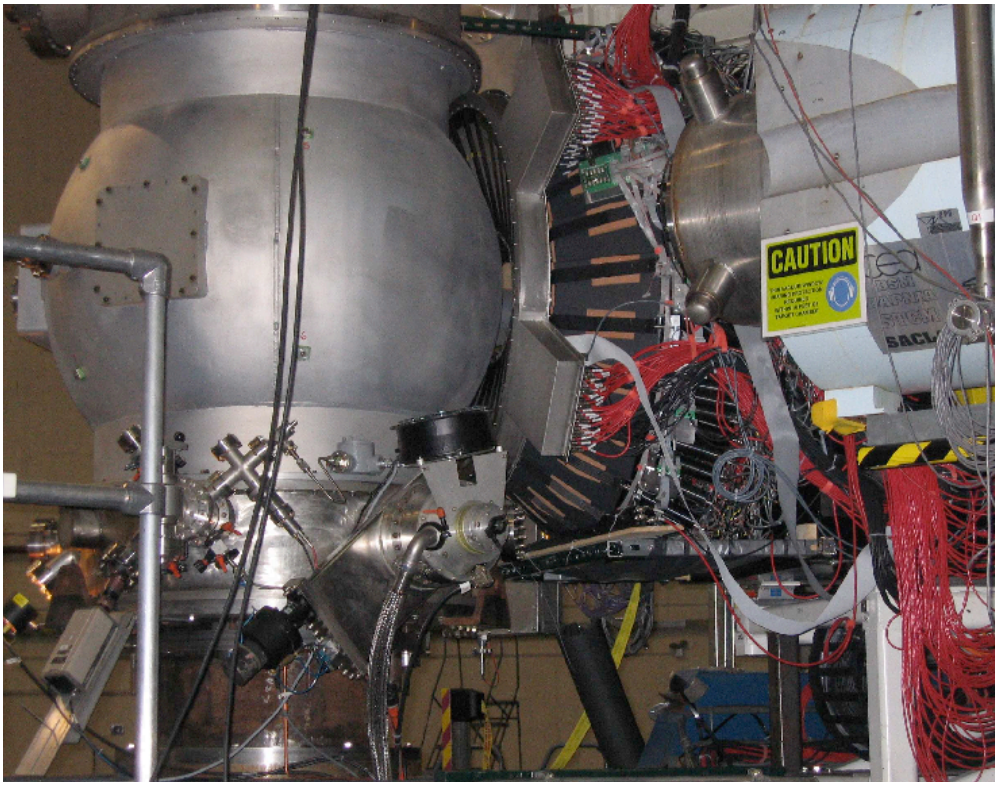

Edited by Kees de Jager and Ronald Ransome

February 2005

Contents

1 Introduction **10**
1.1 Introduction . . . 10

2 Standard Hall A Facilities **12**
2.1 New Hall A Beamline Instrumentation . . . 12
2.1.1 Beam Position Detector (Pavelometer) . . . 12
2.1.2 Beam Energy Spread Monitoring (SLI Monitor) . . . 12
2.1.3 Beam Charge Calorimeter . . . 17
2.2 Septum Magnets . . . 18
2.2.1 Overview . . . 18
2.2.2 Developments in 2004 . . . 18
2.2.3 Outlook . . . 18
2.3 Cryogenic Target . . . 20
2.3.1 Target Density Fluctuations Due to Beam Heating . . . 20
2.4 Coincidence Time Measurement with S2m . . . 22
2.4.1 Signal Processing . . . 22
2.4.2 Results . . . 22
2.4.3 Prospects . . . 23
2.5 The Hall A Compton Polarimeter . . . 25
2.5.1 Overview . . . 25
2.5.2 Detectors . . . 25
2.5.3 Data Acquisition . . . 26
2.5.4 Control System . . . 26
2.5.5 Recent Data . . . 26
2.5.6 Green Laser Upgrade . . . 29
2.5.7 Upgrade Status . . . 35
2.6 BigBite Spectrometer . . . 36
2.6.1 Introduction . . . 36
2.6.2 Magnet . . . 36
2.6.3 Stand . . . 36
2.6.4 Detector Packages . . . 36
2.6.5 Contributions . . . 38
2.6.6 Summary . . . 38
2.7 BPM Bandpass and Triangular Raster . . . 41
2.8 Podd — C++/ROOT Analysis Software . . . 43
2.9 Hall A Luminosity Monitor for Parity-Violating Experiments . . . 45
2.10 Instrumentation for the G_E^n (E02-013) Experiment . . . 48

3 Summaries of Experimental Activities **54**
3.1 E89-044 54
3.2 E91-011 55
3.3 E94-107 59
3.4 E97-110 68
3.5 E97-111 70
3.6 E99-114 73
3.7 E99-115 and E00-114 76
3.8 E00-007 80
3.9 E00-102 83
3.10 E00-110 and E03-106 85
3.11 E01-001 88
3.12 E01-012 93
3.13 E01-020 95
3.14 E04-012 98

4 References **104**

5 Hall A Collaboration Member List **108**

6 Publications **114**

7 Theses **115**

List of Figures

1 A photo of the prototype Pavelometer. 13
2 Data from the Hall C Pavelometer, comparing the X,Y beam position as measured with the dump viewer [green] with that as measured by the Pavelometer [red]. 14
3 Cartoon schematic of the synchrotron light interferometer. 15
4 Control screen for the SLI showing the horizontal and vertical interferograms. The beam-size values above the interferogram are the result of a simple search algorithm to determine I_{max} and I_{min}. The values below the interferogram result from a fit to the expected functional form. 15
5 Plot of the beam width as measured by the SLI vs. OTR. The green dashed curve is a line with slope of one and intercept of zero. 16
6 He target density fluctuations; the RMS width (in ppm) of the helicity-pairs measured in the luminosity monitors is shown as a function of beam current in μA. Data were taken with 48 Hz target fan speed. Below 20 μA the data obey counting statistics, falling as $I^{-1/2}$; above that the widths increase again indicating density fluctuations. 21
7 The distribution of time-differences between the left and right PMTs on the upper eight paddles of S2 on the HRS-R, after correcting for the signal propagation through the scintillator. The other paddles were similar. 23
8 The distribution of coincidence-times between the left and right HRS spectrometers for $(e, e'\pi^+)$ events. The beam's intrinsic microstructure is visible in the peaks every 2 ns from accidental coincidences. 24
9 Schematic layout of the Hall A Compton polarimeter. 25
10 Typical Compton spectrum in the central crystal of the photon calorimeter and signal-to-background ratio during DVCS runs at 5.75 GeV. 27
11 Singles counting rates in the four planes of the electron detector as a function of micro-strip number during DVCS runs at 5.75 GeV. The green points are with the cavity on (Compton events) and the red points are with cavity off (background events). 28
12 Beam polarization measurement performed at 3 GeV for the HAPPEx-Helium run. Blue points are results of the coincidence analysis, red points are electron-only. 29
13 Beam-polarization measurement performed at 3 GeV for the HAPPEx-Hydrogen run. Blue points are results of the coincidence analysis, red points are electron-only. 30

14 Preliminary beam polarization measurement taken during the Hall A DVCS experiments performed at 5.75 GeV. The results are for electron-photon coincidence analysis. Only statistical errors are represented . . . 30
15 Lay-out of the optics table for the green Compton polarimeter. . . 33
16 Expected performances of the integrated and energy-weighted method with the upgraded polarimeter. The beam energy is fixed at 850 MeV. . . . 34
17 The BigBite spectrometer stand. The stand makes use of custom rollers that allow the system to easily rotate along a track located on the floor and the top of the central hub. . . . 37
18 A CAD drawing and a photo of the BigBite detector package for the SRC experiment. . . . 38
19 The BigBite scattering chamber while it was under construction (left) and the chamber during its JLab pressure test (right). . . . 39
20 The short-range correlation experiment as installed in Hall A. Located left of center is the new scattering chamber which matches BigBite's large out-of-plane acceptance. The BigBite dipole magnet is located right of the chamber with the auxiliary and trigger planes mounted behind. . . . 40
21 Calculated response of the BPM electronics to the triangle raster wave form. The top figure shows the amplitude vs time for the 30 kHz low-bandpass frequency response that we have. This is compared to an infinite-bandpass response. The bottom figure shows the amplitude distribution that would be observed, e.g. with the online program raster++. It is also compared to the infinite-bandpass result. . . . 42
22 Drawing of the forward-angle lumi and the exit beam pipe. . . . 46
23 Picture of the inside of the exit beam pipe showing the 8 cups where the lumi detectors were put in. . . . 46
24 The lumi widths versus beam current during a hydrogen run in summer 2004. . . . 47
25 The lumi widths versus the target fan speed during a hydrogen run in summer 2004. . . . 47
26 World data on the neutron electric from factor with planned values of Q^2 in E02-013 and expected accuracy of results. . . . 48
27 Schematic layout of experiment E02-013. . . . 49
28 Magnet for the polarized target. . . . 50
29 A hybrid (K+Rb) cell with ^{3}He . . . 51
30 A prototype high-temperature oven. . . . 52
31 BigBite detector frame with the first drift chamber installed. . . . 52
32 The neutron bars in the cassettes. . . . 53
33 The veto paddles in the cassette. . . . 53

34 Pseudo-data for response functions at $W = 1.23 \pm 0.01$ GeV and $Q^2 = 1.0 \pm 0.2$ GeV^2 are compared with the input model (MAID2000) at the central kinematics and neighboring values of Q^2 representative of the x dependence of acceptance averaging. See text for details. 56
35 Response functions at $W = 1.23$ GeV are compared with recent models and with fits. The units are μb. The labeling distinguishes L, T, LT, and TT contributions to the unpolarized (0) cross section and to transverse (t), normal (n), or longitudinal (l) components of recoil polarization with an h to indicate helicity dependence, if any. Linear combinations that cannot be resolved without Rosenbluth separation are identified by L+T. Black dash-dotted, dotted, short-dashed, and long-dashed curves represent the MAID, DMT, SAID and SL models, respectively. The green mid-dashed curves show a Legendre fit while the solid red curves show a multipole fit. 57
36 Fitted 1+ multipole amplitudes are compared with MAID2003 (red solid), DMT (green dashed) , SAID (blue dash-dot), and SL (cyan dotted) models. Black short-dashed curves show Born baseline amplitudes. 58
37 Fitted 0+ and 1− multipole amplitudes are compared with MAID2003 (red solid), DMT (green dashed) , SAID (blue dash-dot), and SL (cyan dotted) models. Black short-dashed curves show Born baseline amplitudes. 58
38 PID with threshold aerogel Čerenkov counters. 61
39 Hypernuclear spectra of ^{12}C and ^{9}Be with and without RICH. . . 62
40 RICH scheme and event display. 63
41 The role of the RICH for kaon identification: many pions and protons are still present if RICH cuts are not applied. 64
42 RICH performance. On the left side the number of photoelectrons for pions and protons is shown. On the right side the distribution of the Čerenkov angle reconstruction is reported, showing a resolution of 5 mrad. 65
43 ^{9}Li$_\Lambda$ missing-energy spectrum with and without the RICH selection. 66
44 Left: ^{12}B$_\Lambda$ missing-energy spectrum, the solid and dashed lines represent the theoretical data (see text). Right: ^{9}Be$_\Lambda$ missing-energy spectrum, the solid and dashed lines represent the theoretical data (see text). 66
45 Sieve-slit data of x_{sieve} vs ϕ_{tg} for the central foil at 2.24 GeV and 9° with $dp/p = 3\%$. The line crossings are the expected positions of the sieve holes. 69

46 Preliminary results for the reduced cross sections at a beam energy of 3170 MeV. The error bars only show the statistical uncertainty. The dashed line shows the theoretical prediction by Laget in PWIA, the dotted line includes FSI, and the solid line depicts the full calculation. 71
47 Our result for K_{LL} compared with calculations in different approaches: ASY and COZ both from pQCD [46], GPD [52], extended Regge model [53], and CQM [54]. The curve labeled KN is K_{LL}^{KN}, the Klein-Nishina asymmetry for a structureless proton. . 74
48 Extracted RCS form factor R_V, the solid line is a calculation [50]. 75
49 Overview of the HAPPEx-II experiment. 78
50 Preliminary HAPPEx-H and HAPPEx-He results from the 2004 run, with results from PVA4 [56] and SAMPLE [57]. The three ellipses correspond to contours at the 68%, 90% and 99% confidence level. 79
51 The FPP configuration in E00-007. 80
52 Projected A_{LT} data compared to E89-003 results and calculations of Udias *et al.* Open circles are anticipated data points from E00-102, solid squares are E89-003 data obtained at slightly different kinematics. 84
53 E00-102 kinematics. HRS-L remained fixed at 12.5° throughout the experiment while HRS-R varied around the direction of parallel kinematics. 84
54 Left: $\mathrm{H}(e,e'\gamma)X$ coincidence time spectrum for events with a 1 GeV cut in the calorimeter. Right: Electron-proton coincidence time spectrum for events with a true coincidence time cut on the $\mathrm{H}(e,e'\gamma)X$ spectrum. The blue histogram labeled "Mapped Events" is obtained selecting only those blocks in the proton array that lie within a loose footprint of $\mathrm{H}(e,e'\gamma p)$ events, as defined by the position of the photon shower in the calorimeter. 86
55 $\mathrm{H}(e,e'\gamma)X$ missing-mass squared spectrum. 87
56 Missing momentum spectrum for the low ε point at $Q^2 = 3.20\ \mathrm{GeV}^2$. The black circles indicate the data from the LH2 target while the red histogram indicates the total simulated spectrum. The spectrum is decomposed into contributions from the elastic peak (blue), protons from the $\gamma p \to \pi^0 p$ reaction (green) and protons coming from the Aluminum end caps of the target (magenta). 89
57 Reduced cross sections as a function of ε. The solid line is the best linear fit to the data, the dashed line gives the slope assuming $\mu G_E = G_M$, and the dotted line is the slope one obtains using the polarization transfer fit to G_E/G_M. 91

58 Extracted values of $\mu G_E/G_M$ from the present measurement (solid circles), a global analysis of previous Rosenbluth extractions ('×') [63], and the polarization transfer measurements (triangles). 92
59 The Q^2 and W coverage for E01-012 94
60 Preliminary results for ^{3}He virtual photon asymmetry A_1 from E01-012. Radiative corrections and Nitrogen dilution corrections have not been applied. 94
61 Relative yield normalized to beam charge as a function of beam current for a nominal 2 mm × 2 mm raster size. 96
62 Relative yield normalized to beam charge as a function of beam current for a nominal 4mm × 4mm raster size. 96
63 Preliminary distributions *vs.* the neutron angle relative to $\vec{q}$ normalized to a PWIA calculation. The curves are calculations from Laget based on a Glauber treatment of FSI. 97
64 Proposed antidecuplet symmetry group (Diakonov *et al.* [90]). . . 99
65 Experimental setup for E04-012. 100
66 Performance of the hadron PID system for E04-012 (see text for details). 101
67 Neutron calibration spectrum (upper panel), illustrating the achieved missing-mass resolution, and mass calibration of the well-known Λ and Σ resonances (lower panel). 102
68 Preliminary missing-mass spectrum obtained in the $\Sigma^{\circ}_{\overline{10}}$ search. The upper and lower panels show a fit to the background and to a candidate peak, respectively, to illustrate the search technique. The broad structures across the region are known wide resonances. No statistically significant narrow peak has been observed in our preliminary analysis. 103

List of Tables

1 Table of operating range and capabilities of the three energy-width measuring devices. 12
2 Main design parameters of the green Compton polarimeter upgrade compared to the present infra-red system. 31
3 Specification of the Prometheus green laser. 32
4 Specifications for the green Compton polarimeter optical cavity. . . 33
5 Expected single and random coincidence rates compared to the $^{12}\mathrm{C}(e,e'K)^{12}\mathrm{B}_\Lambda$ and $^{9}\mathrm{Be}(e,e'K)^{9}\mathrm{Li}_\Lambda$ events. 60
6 Expected asymmetries and errors for H and ^{4}He targets. When not specified all asymmetries are quoted in ppm units. 77
7 Polarization transfer components in the reaction plane P_t and P_l. The expected values (e.-val.) at bin-center are calculated based on a fit to the Hall A G_E^p-II data, the extracted values from both the CH_2 analyzer and the Carbon analyzer are listed. 81
8 The extracted form factor ratio $\mu_p G_E^p/G_M^p$ and the averaged analyzing power $\langle A_c \rangle$ are listed for both the CH_2 analyzer and the Carbon analyzer, the expected values of $\mu_p G_E^p/G_M^p$ from a fit to the Hall A G_E^p-II data are also listed 81
9 Proposed isotensor multiplet (Capstick *et al.* [91]). 98

1 Introduction

1.1 Introduction

2004 turned out to be again a quite taxing year for Hall A. The year started auspiciously, with both septa installed on the pivot, superconducting and trained to ∼350 A, a current high enough to run all experiments scheduled for 2004, the hypernuclear spectroscopy experiment E94-107 (Frullani, Garibaldi, LeRose and Markowitz) and both HAPPEx experiments, E99-115 (Kumar and Lhuillier) and E00-114 (Armstrong and Michaels). Then, on January 28, a few weeks into running E94-107, a cryo-leak developed in the third quadrupole of the left HRS spectrometer. The leak, probably induced by the forced warm-up after Hurricane Isabel, was so large that Q3 could not be kept superconducting and hence the run had to be aborted. It was decided to replace the waterfall target by the cryotarget, simultaneously with repairing the leak in Q3, in order to regain some of the time lost. As a result of this, further hypernuclear spectroscopy on ^{16}O (which requires the waterfall target) had to be postponed to a future run. Thanks to the heroic (and professional) efforts of the technical support crew the Hall was ready to take beam again on April 15.

Until May 16, E94-107 collected high-quality hypernuclear data on ^{12}C and ^{9}Be, supported by the excellent beam properties, both in energy spread and energy stability, and by the successful operation of the newly installed RICH detector. We then took advantage of the available instrumentation (septa, cryotarget and RICH) to successfully run E04-012 (Reimer and Wojtsekhowski), a high-resolution search for penta-quark partners, for two weeks. The next setback occurred when it was discovered that the right septum quenched at a beam current of $\sim 35\ \mu$A on the 20 cm long racetrack target cells. Because of this the two HAPPEx experiments could only acquire 10% of the total statistics in the beam time allocated. Still, this resulted in a measurement of a quality comparable to that of the available results from the Bates SAMPLE experiment and of the Mainz A4 experiment. In August and early September the septa were removed from the pivot and the instrumentation for the DVCS experiments, E00-110 on the proton (Bertin, Hyde-Wright, Ransome and Sabatié) and E03-106 on the neutron (Bertin, Hyde-Wright, Sabatié and Voutier), was successfully installed. Both these experiments collected high-quality data through Thanksgiving. In December, the installation of BigBite and its associated instrumentation was completed in preparation for running E01-015 (Bertozzi, Piasetzky, Watson and Wood), measuring triple coincident (*e,e'pN*) events from ^{12}C in a study of short-range correlations.

At the time of writing this report, Ed Folts and his crew had discovered and removed a contaminant (a wad of tissue covered by plastic tape) in the helium lines of the right septum. Further tests, however, have indicated that this was not the last problem remaining in the right septum. The schedule for 2005 shows that E01-015, E94-107, E99-115 and E00-114 will be run to completion, followed

by the installation of the instrumentation for E02-013 (Cates, McCormick, Reitz and Wojtsekhowski), a measurement of G_E^n at high Q^2.

Notwithstanding these setbacks in running experiments because of the septum magnets, the research program in Hall A remains extremely productive.

2 Standard Hall A Facilities

2.1 New Hall A Beamline Instrumentation

Contributed by A. Saha and A. Freyberger

2.1.1 Beam Position Detector (Pavelometer)

The Pavelometer is a radiation-hard position monitor located at the entrance to the Hall-A and Hall-C dump. The concept and design were done by Pavel Degtiarenko of the RadCon group here at JLab. The device consists of two CVD silicon carbide plates, $50 \times 200 \times 0.25$ mm^3 which are read out at each end.

Silicon carbide is a semiconductor and the resistance of the plates is a function of temperature. In addition the plates act similar to a thermocouple and produce a potential when there is a temperature gradient across the plate. The extraction of the beam position has been complicated by the fact that there is cross-talk between the plates and that the calibration constant appears to be a function of beam current. The goal is to get a position measurement with a few mm accuracy at currents above a few μA.

Figure 1 shows the prototype detector, while Fig. 2 shows data from the Hall-C Pavelometer, comparing the X,Y beam position as measured with the dump viewer [green] with that as measured by the Pavelometer [red].

2.1.2 Beam Energy Spread Monitoring (SLI Monitor)

Several pieces of instrumentation have been installed in the end-station beam-lines to measure and monitor the beam energy spread during experiments. The instrumentation includes wire scanners, optical transition radiation (OTR) monitors and synchrotron light interferometers (SLI). Table 1 lists this instrumentation and its respective properties. Of this, the SLI monitor is new and will be described here. See Ref. [1] for a more detailed overview of all monitors.

Device	Current range	Beam Interaction	Measures
Harps/Quad Scan	$\leq 20\mu A$	Invasive	$\sigma_E/E.\alpha, \beta, \gamma$
OTR	8 to 180 μA	Slightly Invasive	σ_{beam}
SLI	20 to $\infty\mu A$	Non-Invasive	σ_{beam}

Table 1: Table of operating range and capabilities of the three energy-width measuring devices.

The transverse beam size, σ_{beam}, measured in a dispersive location has two sources:

$$\sigma_{beam} = \sqrt{\sigma_\beta^2 + \sigma_\delta^2},$$

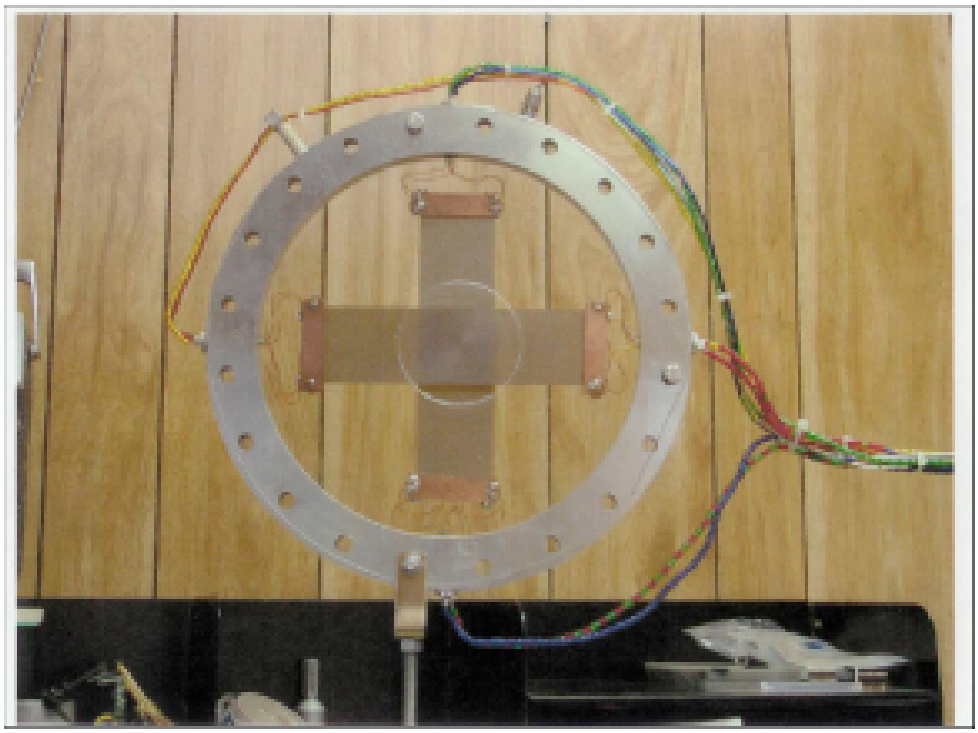

Figure 1: A photo of the prototype Pavelometer.

where $\sigma_\beta = \sqrt{\epsilon\beta}$ is the betatron size and σ_δ is the size due to dispersion. The energy spread is $\frac{\sigma_E}{E_0} = \frac{\sigma_\delta}{D}$, where D is the local dispersion. Ignoring the betatron contribution (which is safe to do when $\frac{\sigma_\beta}{\sigma_\delta} << 1$) the upper limit on the energy spread is:

$$\frac{\sigma_E}{E_0} < \frac{\sigma_{beam}}{D}.$$

When the beam has a small energy spread, as with the JLab beam, σ_β can be comparable to σ_δ and the betatron contribution to the transverse beam size must be taken into account to determine the central value of the energy spread.

In order to minimize the betatron contribution to the beam size, as well as the effect of incoming dispersion, a special optics was devised for the end station transport line to increase the dispersion from 4 m (nominal) to 8 m (high dispersion).

The use of synchrotron light interferometry makes it possible to measure the very small transverse beam size in a completely non-invasive manner. SLI installations at storage rings have an abundant amount of synchrotron light due to the large stored beam current. The lower JLab beam current is advantageous in that beam heating of the SLI optical components is no longer an issue as it is at

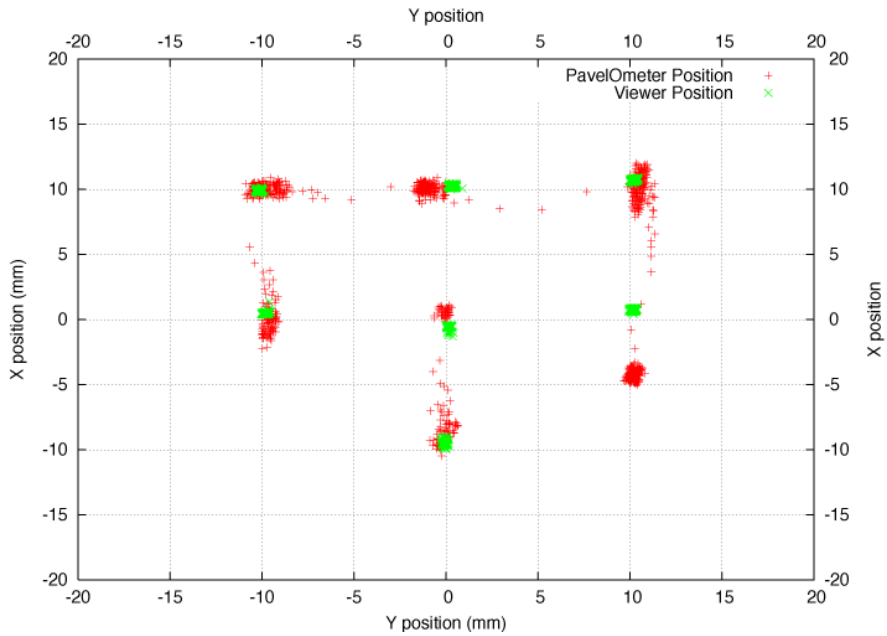

Figure 2: Data from the Hall C Pavelometer, comparing the X,Y beam position as measured with the dump viewer [green] with that as measured by the Pavelometer [red].

storage rings. However, at these lower beam currents the intensity of the light is so diminished that a cooled CCD camera is necessary to image the interferogram.

The difference in light intensity and the choice of CCD camera is the major difference between the JLab SLI and that of T. Mitsuhashi at KEK [2]. A sketch of the components used to make a SLI is shown in Figure 3 and details of the design are found in Ref. [3].

The beam size is a function of the visibility, $\bigvee$, of the interference pattern:

$$\bigvee = \frac{I_{max} - I_{min}}{I_{max} + I_{min}},$$

where I_{max} (I_{min}) is the maximum (minimum) of the interference pattern. Since $\bigvee$ is a ratio, most systematics involved in digitization cancel. However, noise terms contribute to the sum [denominator] leading to a reduced $\bigvee$, or larger calculated beam size and therefore must be kept small.

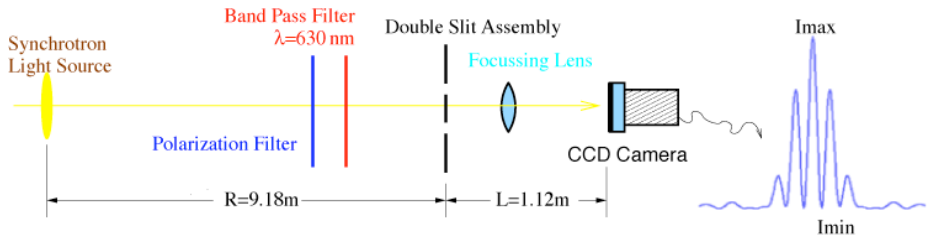

Figure 3: Cartoon schematic of the synchrotron light interferometer.

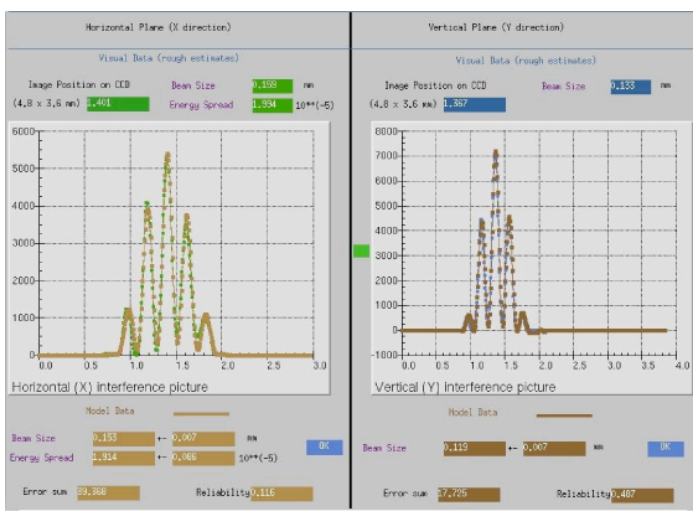

Figure 4: Control screen for the SLI showing the horizontal and vertical interferograms. The beam-size values above the interferogram are the result of a simple search algorithm to determine I_{max} and I_{min}. The values below the interferogram result from a fit to the expected functional form.

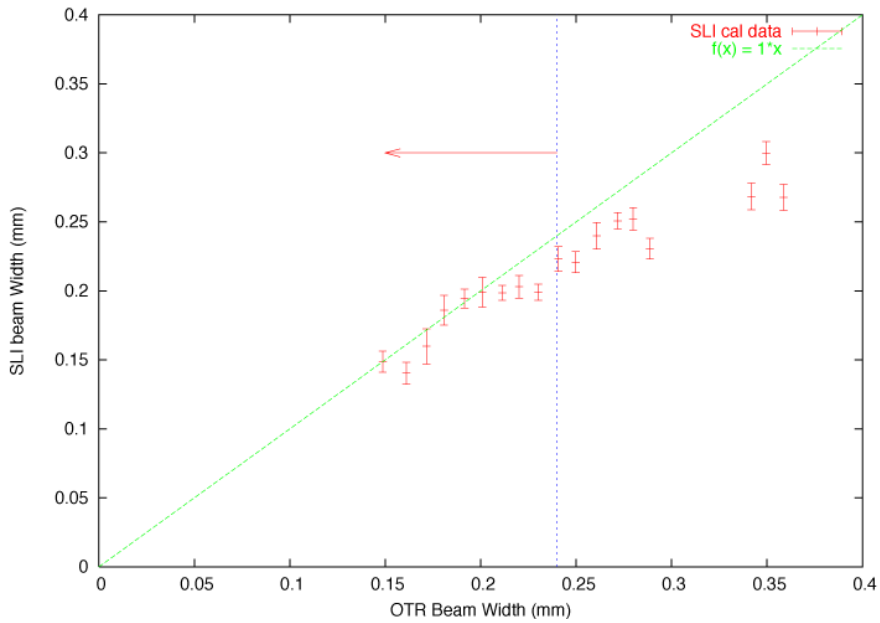

Figure 5: Plot of the beam width as measured by the SLI vs. OTR. The green dashed curve is a line with slope of one and intercept of zero.

For a Gaussian beam distribution the beam size is found to be:

$$\sigma_{beam} = \frac{\lambda_0 R}{\pi d}\sqrt{0.5\ln(1/\bigvee)},$$

where λ_0 is the wavelength of the bandpass filter, R is the distance from the light source to the double slit assembly, d is the slit separation and $\bigvee$ is the measured visibility.

The JLab SLI uses a grid pattern for the double slit assembly. This allows the simultaneous measurement of horizontal and vertical beam sizes. Figure 4 shows the real-time display of the interferogram data and fits to the data. The data update rate is a function of the beam current; as fast as 0.5 seconds at 120 μA and tens of seconds for beam currents less than 20 μA. Figure 5 is a plot of the beam sizes as measured by the OTR and SLI. There is an discrepancy with the larger beam sizes that is presently being investigated.

2.1.3 Beam Charge Calorimeter

The present effort is to develop a low current ($\sim 1\mu$A) calibration device with 0.5% absolute accuracy. Its concept is based on the SLAC silver calorimeter device used many years ago to measure the absolute flux on photons. A design review was held in May 2004 [chaired by Charlie Sinclair] and the review committee returned a favorable review of the design.

The design differs from the SLAC calorimeter in the following ways:

1. tungsten in stead of silver.
2. vacuum in stead of foam insulation.
3. six or more temperature measurements in stead of one.
4. contact cooling in stead of embedded cooling tubes.

Since May, most of the electronics, a NIST traceable thermometer and several types of resistive temperature devices (RTDs) have been procured. Presently the technique for cross calibrating the RTDs against the NIST traceable thermometer is being developed. The goal is to obtain 0.025 °C accuracy (two bits) on the six or more RTDs.

2.2 Septum Magnets

Contributed by J.J. LeRose

2.2.1 Overview

The two septum magnets (left and right) were manufactured by BWXT Technologies of Lynchburg (Virginia) under contract with INFN Rome. They were designed to allow access to scattering angles from 6° to 12.5° up to the maximum momentum of each spectrometer with no degradation in the optical properties of either spectrometer (except for some reduction in solid-angle acceptance). With the septa in place the target is moved 80 cm upstream from its normal position at the Hall A pivot, precluding the use of one HRS with a septum and the other without.

2.2.2 Developments in 2004

During 2004 the septum magnets became operational accessories to the Hall A HRSs. Data were successfully taken for Hypernuclear spectroscopy (E94-107), HAPPEx Helium and Hydrogen (E00-114 and E99-115), and PQE: High Resolution Study of the 1540 Exotic State and Its Partners (E04-012). Data were also taken during 2003 for Small Angle GDH (E97-110) using only the right septum.

The newer left septum has been trained up to 387 A, more than the 370 A needed to get 4 GeV/c at 6°. Training the left to currents as high as achieved in the right, 438 A, does not appear to be problematic.

2.2.3 Outlook

While data taking in 2004 can be characterized as successful, it was not without septum associated problems. These included random failures of the controls computer in the Hall, (these are believed to be radiation induced), cooling of the right septum was slow, and HAPPEx was limited to less than 40 μA of beam current when running with very thick cryogenic targets (at beam currents greater than 40 μA the septa quenched due to beam induced heating), significantly less than what was hoped for. To alleviate these problems the following steps are being taken.

The magnet controls are being reworked to eliminate reliance on the standalone PC in the Hall. At the time of this writing the new controls had not yet been tested.

The cooling problem on the right septum appeared externally to be a faulty check valve in the helium cooling circuit. However, when the magnet was warmed and partially disassembled it was discovered that there was a clog in the helium circuit in the vicinity of the suspicious check valve. This would have produced the same symptoms as a faulty check valve. The check valve itself was found to be in

good working order. The offending clog was removed and the magnet reassembled and leak checked. As of this writing preparations are underway to cool and test the right septum during the February 2005 down.

The beam heating of the septa was studied via a GEANT simulation by Eugene Chudakov [4]. Those studies indicated that a significant amount of septum heating was the result of very low-energy Møller electrons impinging on the bore of the septa. Those studies further indicated that a small sweeper magnet (0.3 T over 0.1 m) would eliminate those electrons with only very little effect on the "good" trajectories (a 3 GeV/c electron is deflected 3 mrad). The sweeper magnet has been designed and is being built at JLab. It is expected to be ready for the next HAPPEx run later in 2005.

Another small improvement underway is the design and development of a remote sieve insertion system to go with the septa at 6°. This will greatly streamline optics studies as a Hall access will no longer be required to insert or remove the sieves.

2.3 Cryogenic Target

Contributed by J. P. Chen and D. Armstrong

The Hall A cryotarget system [5] usually consists of 3 loops: loop 1 is often for gaseous helium (either ^{3}He or ^{4}He) at 6 K and 15 atm, loop 2 liquid hydrogen at 19 K and loop 3 liquid deuterium at 22 K. Both the LH2 and LD2 loops are operating at pressures above 20 psi. Each of the LH2 and LD2 loops has two target cells with typical lengths of 15 cm or 4 cm.

In 2004, the cryotarget system was used for a number of experiments: Pentaquark Partner Search, HAPPEx-II and HAPPEx-He (first period), and DVCS. The Pentaquark and DVCS experiments used the standard target cells (machined 4 and 15 cm "beer cans"). HAPPEx-II and HAPPEx-He used 20 cm new race-track cells which were designed by the Cal State LA group. During the HAPPEx-II and HAPPEx-He running, loop 1 had a 10 mil thick single race-track cell for high pressure helium running. Loop 2 had a 5 mil thick single race-track cell for liquid hydrogen. Loop 3 was the original beer can type double-cell (4 cm and 15 cm) as a backup for LH2 running. The flow is vertical (perpendicular to the beam direction) for the race-track cells. Due to the additional length the required cooling power would exceed the End Station Refrigerator limitation at 100 μA, so that a supplement from the Central Helium Liquefier (CHL) was needed. For the HAPPEx-II and HAPPEx-He running, both LH2 and helium targets were cooled with 4.2 K coolant from CHL, which is expected to provide enough cooling power for beam currents up to 100 μA. Due to other limitations (the beam heating of the septum magnets), the beam current was restricted to below 40 μA for the first run period.

Density fluctuation is a major concern for the parity experiments, especially the LH2 parity. This was the first time the race-track style cells were used. The race-track cell worked pretty well for the first run period. A study was done with beam current up to 60 μA, a raster size up to 4 mm $\times$ 4 mm and fan speed of up to 60 Hz for both LH2 and helium targets. Details of this study are presented in the next section.

2.3.1 Target Density Fluctuations Due to Beam Heating

Target density fluctuations on the time-scale of the helicity reversal are a source of concern for parity-violation experiments, since they increase the statistical error beyond pure counting statistics. Tests in Nov. 2002 [6] had shown that the standard cigar-shaped machined target cells exhibited unacceptably large density fluctuations ("boiling") with liquid hydrogen even at moderate beam currents with large raster sizes and large fan speeds. Consequently, for HAPPEx-II and HAPPEx-He, a new "race-track" style cell, with transverse fluid flow was designed and built by the Cal State LA group along with the JLab targets group. Similar racetrack cells of 20 cm in length were built for both liquid hydrogen and (with

thicker windows) for high-pressure cold helium gas. Density fluctuations were studied during the summer HAPPEx-II and HAPPEx-He runs using the luminosity monitors. For hydrogen, the racetrack cells had dramatically reduced density fluctuations compared to the standard cells; under similar raster and fan speed settings the fluctuations were smaller by an order of magnitude. With a slightly increased raster size (we were limited to 4 mm by 4 mm) it appears that density fluctuations will contribute negligibly for the hydrogen experiment, even at the design (100 μA) beam current.

More surprisingly, with the cold helium gas target, similar density fluctuations were observed (clearly, there can be no phase change, so the phenomenon cannot be called boiling!). As seen in Fig. 6, a non-statistical behavior was observed at even modest currents for a typical raster size. The detailed physics of these fluctuations is not understood; presumably the flow is not sufficiently turbulent to average out local beam-heating induced temperature increases in the gas. Fortunately, fluctuations on this scale (a few hundred ppm) are not a serious problem for HAPPEx-He, since the counting-statistics width of the helicity-pair distribution at the design luminosity is 1000 ppm, so added in quadrature the effect is not large. For the next HAPPEx-He run, we will attempt to optimize the combination of the raster size, target fan speed, and target operating conditions (temperature/pressure) to minimize this effect.

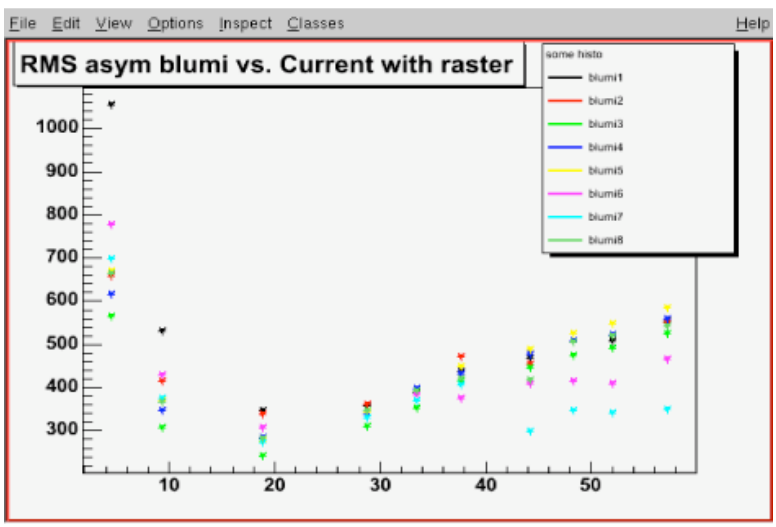

Figure 6: He target density fluctuations; the RMS width (in ppm) of the helicity-pairs measured in the luminosity monitors is shown as a function of beam current in μA. Data were taken with 48 Hz target fan speed. Below 20 μA the data obey counting statistics, falling as $I^{-1/2}$; above that the widths increase again indicating density fluctuations.

2.4 Coincidence Time Measurement with S2m

Contributed by R. Feuerbach

The need for an improved time-of-flight resolution was recognized after the initial set of experiments in Hall A. To address this need the high-resolution S2m detectors were constructed and installed in the HRS spectrometers in 2003 in preparation for the Hypernuclear Spectroscopy experiment (E94-107), which ran in early 2004 [7]. In addition to improving the intrinsic timing resolution of the trigger plane, the signal pathway for measuring the relative timing of the two spectrometers was improved.

2.4.1 Signal Processing

The signal-path for S2m was designed so as to best preserve the timing of the pulses. Each S2m plane consists of 16 2-inch thick paddles of plastic scintillator EJ-230 [8], read out by PMTs [9] on both ends. The signals from each photomultiplier tube are sent to a passive 90/10% splitter, with the greater portion sent to a P/S 706 discriminator on the detector frame and the lesser portion sent to the Fastbus ADCs. To form S2's contribution to the trigger, the first discriminator output for each paddle's left- and right-side PMTs are logically AND'ed, and an OR over these results is performed. The right-side PMTs determine the timing of this trigger since their trigger-cables from the discriminator are 30 ns longer than those for the PMTs on the left side. The second output from the discriminator is sent through a NIM-ECL convertor and an active ECL-delay module before being readout out by LeCroy 1875A TDC modules set to 50 ps/channel.

In order to minimize the jitter of the trigger-gate timing, the gate for the spectrometer is "retimed" by forming a logical AND of the trigger from the Trigger Supervisor and the input of the local S2-plane to the trigger. This gate is then used to control the TDC and ADC digitization and readout. A copy of this gate is also sent to the other HRS, where the relative timing between the gates of the two spectrometers are measured by a TDC. This is performed for both spectrometers, so there is a redundant readout of the relative timing of the gates.

2.4.2 Results

During the Hypernuclear Spectroscopy (E94-107) experiment, the S2m planes were used in the primary trigger on both arms. To measure the inherent timing resolution, the time difference between the left and right PMTs of each paddle were measured. After correcting for the signal propagation time through the scintillator, the width of the timing-difference distribution was typically better than $\sigma_{l-r} \approx 200$ ps. The distributions for the upper eight paddles of the HRS-R, which are representative for all 32 paddles between both spectrometer, are shown in

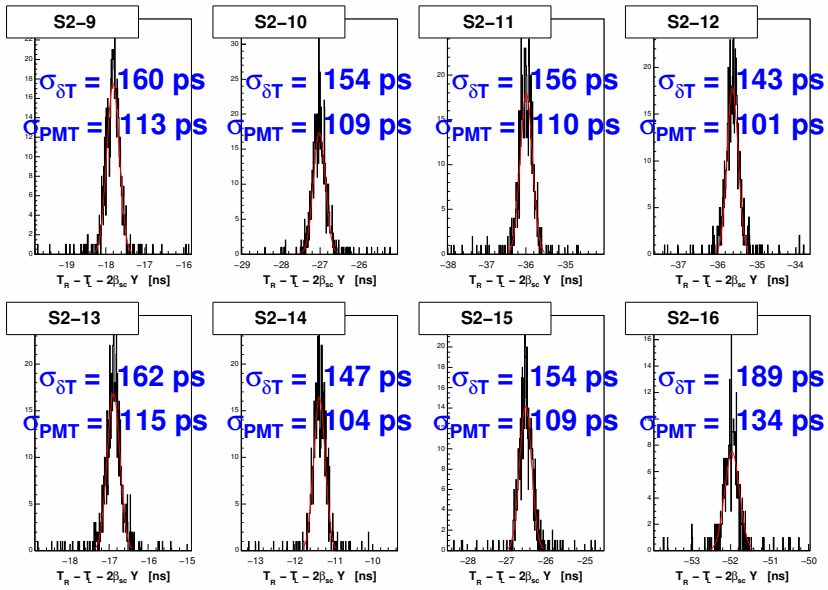

Figure 7: The distribution of time-differences between the left and right PMTs on the upper eight paddles of S2 on the HRS-R, after correcting for the signal propagation through the scintillator. The other paddles were similar.

Fig. 7. Since the time at the plane is calculated from the average of the measurements from both PMTs, the expected reconstructed time resolution for each paddle is $\sigma_{s2} = \frac{1}{2}\sigma_{l-r} \approx 100$ ps.

The coincidence time, the difference between when the particles measured in the spectrometers left the target, is used to aid in particle identification and select only tracks from the same beam-bucket. A coincidence-time distribution from E94-107 for $(e, e'\pi^+)$ events is shown in Fig. 8, where the e' and π^+ were selected by gas and aerogel Čerenkov detectors. The achieved 500 ps (FWHM) timeresolution permits the direct observation of the beam 2 ns micro-structure, and the clean selection of events from the same beam bucket.

2.4.3 Prospects

In addition to measuring the relative time between the two spectrometers, the accelerator's RF signal can also be used to provide a reference time, albeit with a 2 ns cycle. The advantage of this measurement is the time resolution depends solely on the measurements from a single arm and on the intrinsic resolution of the TDCs. This was attempted during E94-107 and provided valuable information for correcting the flight-path calculation, but instrumental difficulties with the Lecroy TDCs prevented its full implementation. Next year we will be installing new VME-based F1-TDCs to read out S2m, the relative gate-timing of the HRSs, and the

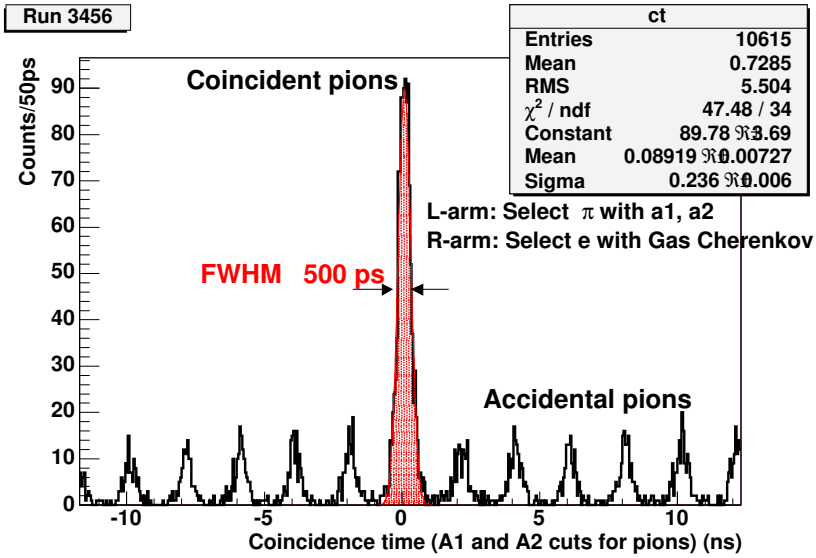

Figure 8: The distribution of coincidence-times between the left and right HRS spectrometers for $(e, e'\pi^+)$ events. The beam's intrinsic microstructure is visible in the peaks every 2 ns from accidental coincidences.

timing of the RF-pulses; this technique will be explored more fully.

2.5 The Hall A Compton Polarimeter

Contributed by S. Nanda

2.5.1 Overview

Many of the Hall A experiments at JLab using polarized electron beams require measurement of beam polarization as fast and as accurately as possible. The Hall A Compton Polarimeter provides such measurements in a continuous and non-invasive manner via Compton scattering of polarized electrons from polarized photons trapped in a Fabry-Perot cavity.

A schematic layout of the Compton polarimeter is shown in Fig. 9. The electron beam is transported through a vertical magnetic chicane consisting of four dipole magnets. A high-finesse Fabry-Perot cavity housed on a optical table in the straight section of the chicane serves as the photon target. A 240 mW, 1064 nm infrared laser feeds the cavity where it is amplified to about 1000 W. The electron beam interacts with these intra-cavity photons. The Compton back-scattered photons are detected in an electromagnetic calorimeter consisting of 25 $PbWO_4$ crystals. The recoil electrons, separated from the primary beam by the fourth dipole of the chicane are detected in a silicon micro-strip detector. The electron beam polarization is deduced from the counting rate asymmetries of the detected particles.

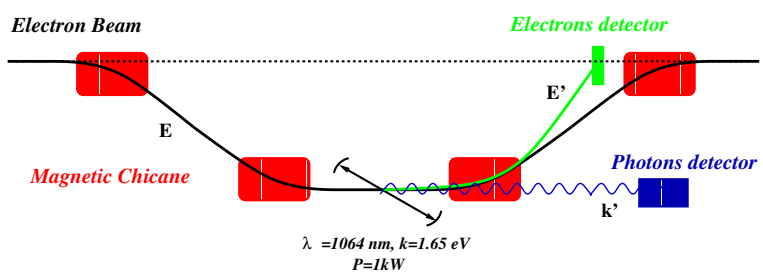

Figure 9: Schematic layout of the Hall A Compton polarimeter.

During 2004, the Compton polarimeter configuration has seen substantial upgrades in its hardware as well as software, improving overall performance and reliability of the system. Generally, the polarimeter performed reasonably well down to 2.5 GeV beam energy. In the following sections, developments in the Compton Polarimeter, results from recent experiments, and future plans are presented.

2.5.2 Detectors

In the previous setup, the electron detector was moved closer to the primary beam to provide more efficient coverage of the Compton spectrum for the lower energy

operation of the GDH experiment. In spring 2004, the electron detector chamber was opened to reposition the micro-strips assembly to its original position i.e. 5 mm from the primary beam. The photo-multiplier tube of the central crystal of the calorimeter had dropped its gain considerably. During this time the photo-tube was replaced. After the changes, both detectors were tested successfully.

2.5.3 Data Acquisition

The data acquisition, analysis, and slow control packages for the Compton polarimeter have been integrated into a single Linux platform which provides more efficient handling of Compton data. The earlier system, adaqs1, that served as a backup system for much of the year was retired in the fall of 2004.

In summer of 2004, the Compton platform was upgraded to Redhat Enterprise Linux 3 system. The CODA acquisition software was upgraded to version 2.5 for the new system with Compton specific patches. Spyacq, the TCL application for configuring the acquisition trigger, monitoring on-line events, and automating optics functions was also upgraded for the new system. Furthermore, the data analysis software, has been upgraded to ROOT version 4.0. Several improvements have been made to the software package eventSelection, the main analysis engine, to analyze coincidence data more reliably. The package has been ported to the new Compton machine. The analyzer is capable of analyzing electron-only of electron-photon coincidence data.

A new feature was added to the Compton acquisition software to relay the online counting rates of the Compton detectors through the EPICS system to accelerator operators. This has facilitated beam tuning with a marked improvement in beam halo minimization.

2.5.4 Control System

The migration of the EPICS control software, originally developed by the Saclay group, to Jefferson Lab EPICS software group launched last year, was completed in summer of 2004. The original EPICS IOC cptaq3, has been replaced by the new IOC iochacp, which is managed by the EPICS group. The Compton polarimeter EPICS control screens have now been incorporated into the main Hall A Menu.

The optics control hardware developed several problems during operation. The rotary motion control mechanism, used to orient a quarter-wave plate for control of the polarization of the laser, developed intermittent failures. In addition, the cavity servo-control system used to keep the cavity locked, showed drop outs in cavity lock acquisition. Both were traced to poor cabling and were repaired.

2.5.5 Recent Data

The Hall A Compton polarimeter has been in production for much of the running time in the hall during 2004. Continuous measurement of beam polarization for the

HAPPEx (E00-114 and E99-115), and DVCS (E00-110 and E03-106) experiments has been carried out successfully.

The primary limitation to the operation of the polarimeter bas been unacceptable backgrounds in the Compton detectors arising from beam halo. However, for all four experiments during the year, the overall beam quality delivered by the accelerator has been substantially improved compared to previous years. The beam tuning procedure has been refined to optimize the beam quality for compton operation. A careful alignment of the orbit in the injector and path-length optimization in the recirculating arcs with "dog-leg" corrections have proven to be effective in reducing the beam background rates in the Compton detectors to well below 100 Hz/μA. With typical Compton interaction rates of about 1 kHz/μA, signal-to-background ratios have shown marked improvements during the experiments. A typical Compton photon spectrum obtained during the DVCS experiment at 5.75 GeV is shown in Fig. 10, along with signal-to-background ratio. Average signal-to-background ratio for the year's running was about 20.

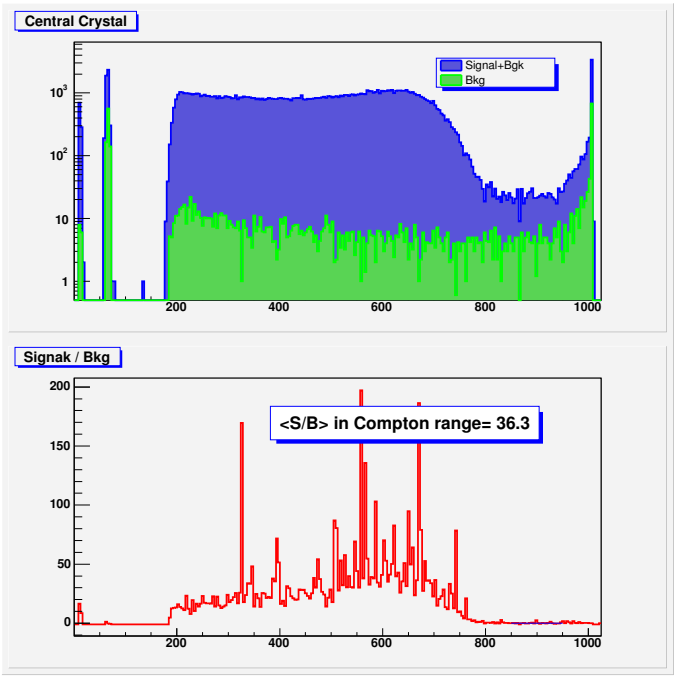

Figure 10: Typical Compton spectrum in the central crystal of the photon calorimeter and signal-to-background ratio during DVCS runs at 5.75 GeV.

A beam halo, characterized by its exponential shape, has been measured typically 10 times higher than the Compton rate in the electron detector in 2003 [10]. A possible origin of this halo could be the continuous offset of the diode laser at the source which doesn't turn off completely between two beam pulses. With the

improved beam tuning procedure, this halo has been substantially reduced. Illustrated in Fig. 11 are the singles counting rates in the four planes of the electron detector as a function of micro-strip number during DVCS runs at 5.75 GeV for a typical measurement. The green points are with the cavity on representing Compton events whereas the red points are with cavity off representing background hits from the beam halo. The usual exponential shape for the background events is noticeably absent in these spectra demonstrating the superb beam quality.

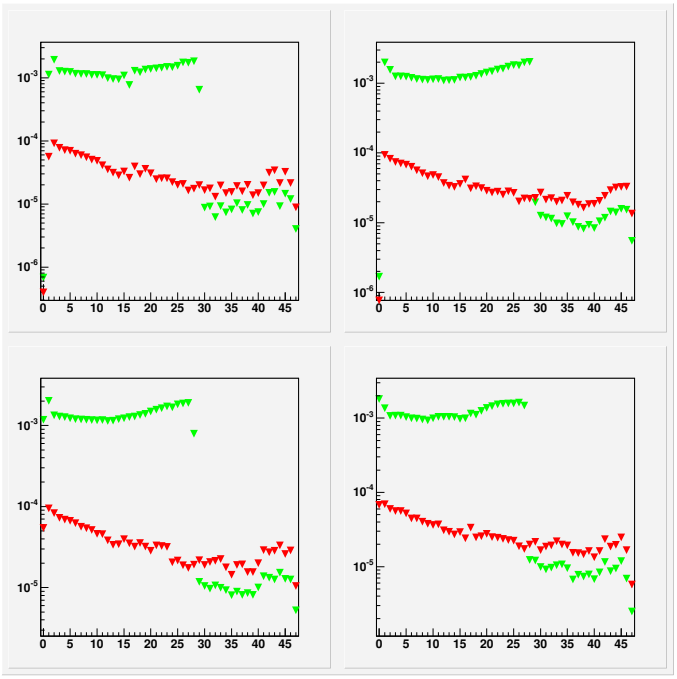

Figure 11: Singles counting rates in the four planes of the electron detector as a function of micro-strip number during DVCS runs at 5.75 GeV. The green points are with the cavity on (Compton events) and the red points are with cavity off (background events).

Compton polarimeter data taken for HAPPEx between June 10 and July 25, 2004 have been analyzed for both electron-only and electron-photon coincidence triggers. Figure 12 shows results obtained at 3 GeV for the HAPPEx-Helium runs. Blue points are results of the coincidence analysis, red points of the electron-only analysis. The two methods are in good agreement although they have different systematic errors. During this period, the so-called super-lattice photo-cathode in gun 3 was used at the injector. This cathode yielded an impressively high polarization of about 86%. Nonetheless, the photo-cathode had poor life time requiring moving the laser spot frequently.

As a result, shorty after the HAPPEx-II experiment the electron source was

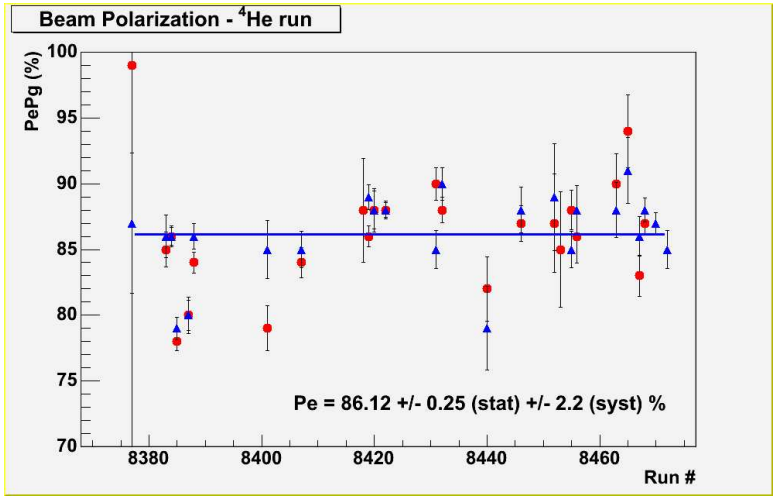

Figure 12: Beam polarization measurement performed at 3 GeV for the HAPPEx-Helium run. Blue points are results of the coincidence analysis, red points are electron-only.

changed to gun 2. Shown in Fig. 13 are the results obtained at 3 GeV for the HAPPEx-II runs. The first period is with gun 3 and and the last period is with gun 2. With gun 2 the beam polarization dropped to about 75%. The signal-to-background ratio for the photon detector during both HAPPEx runs was typically about 16.

The Compton polarimeter took measurements for the DVCS experiments on the proton and the neutron from September 24 to December 5, 2004. Shown in Fig. 14 are the results obtained at 5.7 GeV for the DVCS runs. The top figure is electron beam polarization and the bottom one is the signal-to-background ratio in the photon detector, as a function of time. The source of electrons during this period was gun 2. The average polarization was about 75%. The first few data points showing about 68% polarization were the result of an incorrect orientation of the polarization vector. This was corrected for the rest of the experiment after the inital measurement. As seen from the measurements the beam polarization stayed stable during the two and half month period. The signal-to-background, averaging at about 26, was considerably better than during the HAPPEx runs. This is primarily due to the almost double beam energy which produces less background from residual gases in the beam path.

2.5.6 Green Laser Upgrade

The upgrade of the Compton polarimeter is motivated by upcoming high accuracy experiments with a very demanding requirement on the beam polarization.

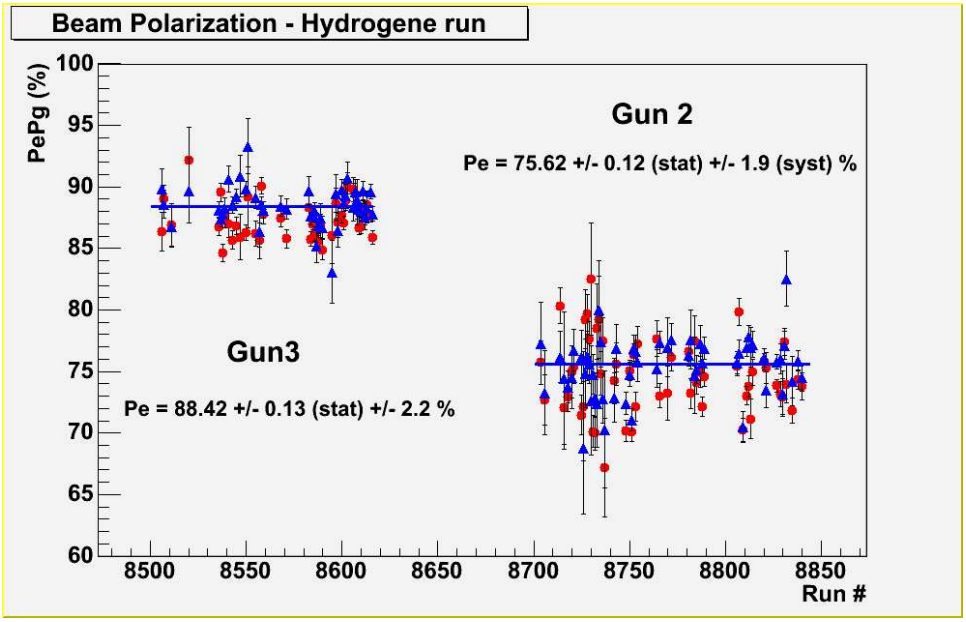

Figure 13: Beam-polarization measurement performed at 3 GeV for the HAPPEx-Hydrogen run. Blue points are results of the coincidence analysis, red points are electron-only.

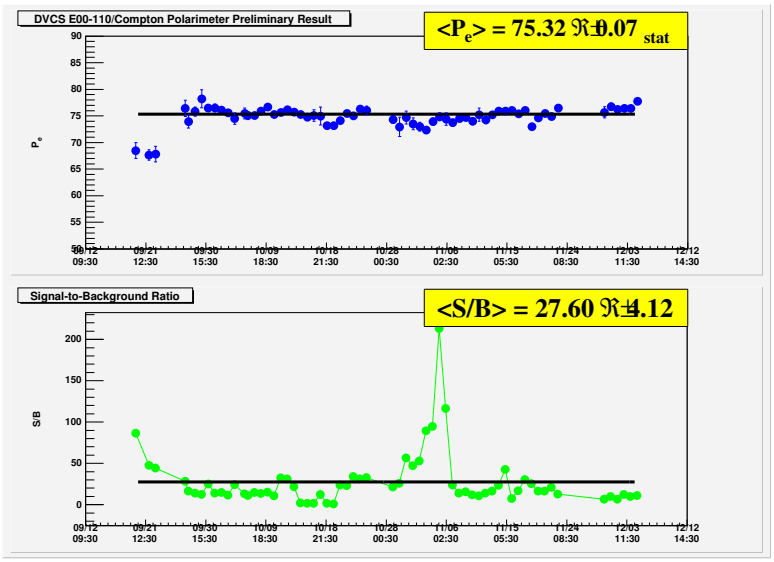

Figure 14: Preliminary beam polarization measurement taken during the Hall A DVCS experiments performed at 5.75 GeV. The results are for electron-photon coincidence analysis. Only statistical errors are represented

Defining k as the photon energy and E as the electron beam energy, the figure of merit of a Compton measurement scales with $k^2 \times E^2$, making high accuracy polarimetry a real challenge at low energy. The proposed upgrade is driven by the requirement of the Lead Parity experiment of 1% relative accuracy at 850 MeV. The present infra-red system, while capable of achieving such accuracies at higher energy ($\geq$ 6 GeV), falls far short at lower energies. We plan to upgrade the existing Fabry-Perot cavity operating at 1064 nm (IR) with about 1.5 kW power to a 532 nm (green) cavity with 3 kW power. The figure of merit will increase 4 times compared to the IR system, for the same photon density in the cavity. In addition, improvements to the electron detector and photon calorimeter combined with the development of a new integrated method shows promise of absolute accuracies approaching 1% at 0.85 GeV beam energy. The main parameters of the green Compton upgrade are shown in Table 2.

Parameter	Present	Upgrade
Wavelength (nm)	1064	532
Cavity Power (W)	1500	3000
Cavity Q	1.0×10^{11}	1.8×10^{11}
Luminosity @50μA (μb.s)$^{-1}$	0.26	0.26
FOM (σ.A^2) @.85Gev	0.57	2.2
Energy Range (GeV)	2 - 6	0.8 - 6
$\delta P_e/P_e$ @.85Gev	-	1%

Table 2: Main design parameters of the green Compton polarimeter upgrade compared to the present infra-red system.

The conceptual design [11] of the green Compton polarimeter utilizes much of the design philosophy and the existing infrastructure of the present Compton polarimeter. The optical layout of the green Compton polarimeter is shown in Fig. 15. The laser will be an Innolight Prometheus [16] laser which is a compact solid-state diode-pumped, frequency-doubled Nd:YAG laser that provides single-frequency green (532 nm) continuous wave (CW) output of 100 mW. It offers superb spectral line width (1 kHz) in the green and fast frequency tuning capability via a piezo-electric transducer (PZT). These features, essential for locking the laser beam to a high-finesse cavity, make the Prometheus an ideal choice for our design. The specifications of the Prometheus laser are shown in Table 2.5.6.

The heart of the upgrade plan is to replace the infrared cavity with a 532 nm green cavity fed by the new laser. The specifications of the proposed cavity are shown in Table 2.5.6. Such a cavity represents the state of the art in cavity technology. Nonetheless, recent advances in the manufacturing of high-reflectivity and low-loss dielectric mirrors as well as availability of narrow line width green lasers facilitates the feasibility of our challenging design goal. High-gain cavities

Wavelength	532	nm
Output Power	100*	mW
Beam diameter	0.38	mm
Beam divergence	2.8	mrad
Polarization	> 100:1	
Thermal tuning coefficient	-6	GHz/K
Thermal tuning range	60	GHz
Thermal response bandwidth	1	Hz
PZT tuning coefficient	2	MHz/V
PZT tuning range	±200	MHz
PZT response bandwidth	100	kHz
Spectral line width	1	kHz/100 ms
Coherence length	>1	km
Frequency drift	2	MHz/min

Table 3: Specification of the Prometheus green laser.

at 532 nm have been successfully demonstrated by the KEK-ATF group [12] and very high gain super cavities are being planned [13]. Recently, the PVLAS [14] group has successfully constructed a 532 nm cavity with geometry and gain comparable to our proposed design here.

We plan to implement the well-proven Pound-Drever-Hall [17] (PDH) method to lock the laser to the cavity. While the cavity itself remains monolithc with fixed mirrors, the reflected light from the cavity will be monitored with a photo-diode to sense the cavity detune. This sgnal will be fed back to the laser to change its frequency so as to keep the resonance locked. We will implement an adaptation of the PVLAS [14] servo-lock system for the PDH locking scheme.

In addition, as part of the upgrade both the electron and the photon detectors will be replaced with higher performance detectors. The electron detector will be upgraded to micro-strips of finer pitch. We want to keep 48 channels per plane with the same front-end electronics in order to reduce the cost of the upgrade. Going to very small strip size would then shrink the active area of the detector and define a too narrow operating range in beam energy. Therefore our goal is to achieve a 150 μm resolution on the vertical position of the scattered electrons using 300 μm wide micro-strips. At 850 MeV, the edge of the Compton spectrum is expected to stand at 6.8 mm above the primary beam.

The present photon calorimeter has shown good performances at photon energies of 50 MeV or higher. With a green laser this corresponds to beam energies $\geq$ 2 GeV. In that range, the interactions of the photons with a dense detector are dominated by the e^+e^- pair creation process. The high multiplicity of the secondary particles leads to a Gaussian distribution of the deposited energy with a tail at lower energy due to leakage of the electromagnetic showers in the back and

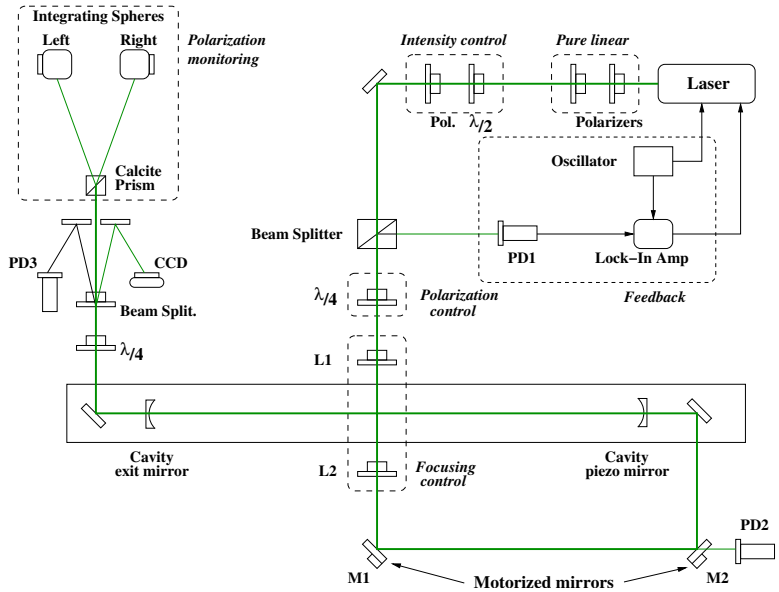

Figure 15: Lay-out of the optics table for the green Compton polarimeter.

Parameter	Symbol	Specification
Fabry-Perot Resonator		
Finesse	F	49,000
Power Gain	G	14,990
Q-factor	Q	1.8×10^{11}
Length	L	0.98 m
Free Spectral Range	$\Delta\nu_{FSR}$	153 MHz
Cavity Bandwidth	$\delta\nu_{cav}$	3.12 kHz
Mirrors		
Radius of curvature	ρ	0.5 m
Diameter	d	7.75 mm
Thickness	t	4 mm
Reflectivity	r	99.9936%
Loss	a	$<$ 5 ppm
Damage Threshold		10 kW/mm^2, CW

Table 4: Specifications for the green Compton polarimeter optical cavity.

on the side of the calorimeter. The main systematic errors of the semi-integrated method are from the calibration of the electron detector, the parametrization of the response function and pile-up. The calibration is improved by the upgrade proposed in the previous section. A better control of the parametrization of the response function can be achieved by using a calorimeter of larger transverse dimensions as compared to the existing $2 \times 2 \times 23$ cm^3 $PbWO_4$ crystal. The detailed design of the new photon detector has not been finalized. We are in the process of evaluating various options.

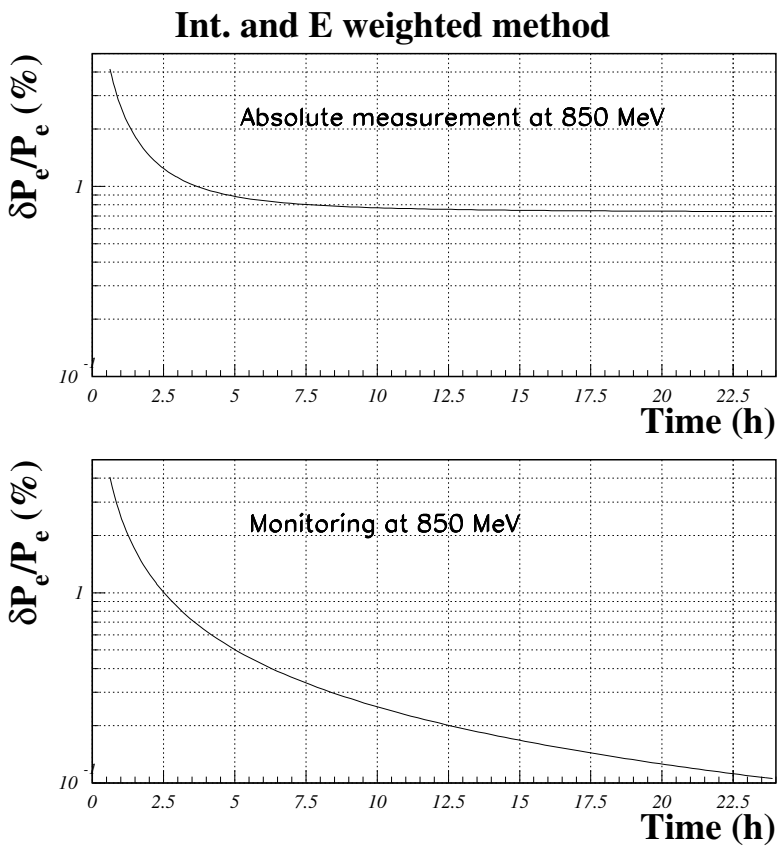

Figure 16: Expected performances of the integrated and energy-weighted method with the upgraded polarimeter. The beam energy is fixed at 850 MeV.

Integrating the signal of the photon calorimeter between a low threshold and the Compton edge has numerous advantages for the reduction of the systematic errors [11]. We have tested the concept during the DVCS Compton polarimeter runs with prototype front-end integrating electronics for pre-integration of the photon signal. This signal was then read out with v-to-f converters gates by the usual helicity cycle of the electron beam. Preliminary results indicate that this approach yields the same beam polarization as the counting method with a clean

beam tune. Systematic errors associated with backgrounds and non-linearilties in the integrating electronics are under study.

A detailed discussion on the expected performance of the green Compton polarimeter can be found in the conceptual design report [11]. With the planned upgrade and the incorporation of the integrating method, the expected accuracies of the polarimeter are shown in Fig. 16.

2.5.7 Upgrade Status

The major sub-systems for the green Compton optics have been procured. The Prometheus laser has been delivered to the lab and we are in the process of setting up a dedicated green laser lab. A set of twelve high-finesse mirrors have been delivered by Research Electro Optics [15]. The servo-system for cavity lock has been completed at Saclay and will be delivered to JLab soon. Design of a prototype cavity is underway at JLab. Our goal is to complete the test setup in the new green laser lab and evaluate the performance of the prototype cavity in the year 2005. In addition, we plan to complete final design studies of the new electron and photon detectors during 2005.

2.6 BigBite Spectrometer

Contributed by D.W. Higinbotham

2.6.1 Introduction

Presently, there are seven fully approved Hall A experiments that require the BigBite spectrometer [18, 19, 20, 21, 22, 23, 24] along with one conditionally approved experiment [25]. This new spectrometer consists of a single large dipole magnet combined with various detector packages. In its most standard configuration, the spectrometer will have an angular acceptance of 96 msr with a vertical acceptance of ±300 mrad and a horizontal acceptance of ±80 mrad. The momentum acceptance of the spectrometer is nearly unlimited, though the momentum resolution, dp/p, and acceptance decreases linearly for momenta greater than 1 GeV/c. The spectrometer will have an extended target capacity of ± 10 cm at 90°. In general, the BigBite spectrometer is a very flexible, large acceptance device which can easily be reconfigured for different experiments.

2.6.2 Magnet

The dipole magnet for the BigBite spectrometer was originally built for the NIKHEF internal target program and was subsequently purchased by Hall A. At JLab, the magnet has been tested up to 550 A and the magnet has operated successfully in the Hall for over one month with a current of 518 A and a central field of 0.92 T. A Hall probe has been attached to the magnet to provide a read-back measurement of the field. In late April, there will be a test to determine the maximum current and field that can be achieved with the magnet.

2.6.3 Stand

The stand for the BigBite magnet and a carriage for the various detector packages have been built and tested in the Hall. In addition to being used for the BigBite experiments, the DVCS collaboration used the BigBite stand for mounting their experiment. With an HRS between BigBite and the beam line, the BigBite spectrometer can be located between 99° and 65° as 52.5° of clearance is required between the spectrometer and BigBite with BigBite located 1.1 m from target. A photo of the stand is shown in Fig. 17.

2.6.4 Detector Packages

For the approved experiments, there are already three different detector packages being built. The first package, which was built for the short-range correlation experiment [18] and has already been tested in the Hall, is comprised solely of scintillator planes. The first plane, known as the auxiliary plane, is placed immediately after the BigBite magnet. A segmented trigger plane, which is located

Figure 17: The BigBite spectrometer stand. The stand makes use of custom rollers that allow the system to easily rotate along a track located on the floor and the top of the central hub.

1 m further back, is comprised of 3 mm and 30 mm scintillating layers to provide dE/E particle identification and has timing resolution better than 0.5 ns. The auxiliary and trigger planes together will provide approximately 5% momentum resolution at 300 MeV/c with approximately 10 mrad angular resolution. The auxiliary plane only has one-sided read-out, so the spectrometer in this configuration will not be able to determine the reaction vertex by itself. A design drawing along with a photograph of these detectors installed in their frame is shown in Fig. 18.

The second detector package, optimized for detecting low-energy hadrons, will use the same trigger plane but the auxiliary plane will be replaced by two drift chambers. The chambers will allow BigBite to provide approximately 1% momentum resolution, approx. 3 mrad angular resolution in θ and ϕ, and 3 mm y-target resolution. This package will be used for measurements of threshold pion production [19], threshold deuteron electro-disintegration [21], and detailed measurements of the ^{3}He system [22].

The third detector package is being optimized for detecting high-energy electrons and will be used for the G_E^n and transversity experiments [20, 23, 24, 25]. This package will use three drift chambers to give the spectrometer multi-track capabilities. In addition, this package will have a shower calorimeter. Further details of this system can be found in the G_E^n section.

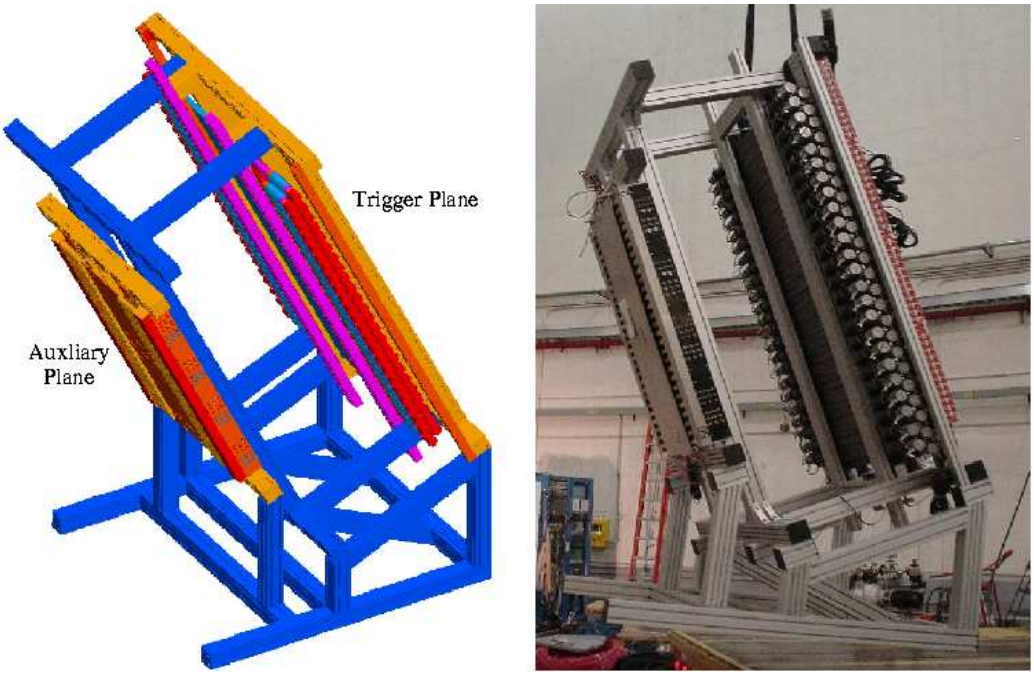

Figure 18: A CAD drawing and a photo of the BigBite detector package for the SRC experiment.

2.6.5 Contributions

Many groups have already built or are building various parts for the BigBite spectrometer. Eli Piasetzky and the Tel Aviv group have built the auxiliary scintillator plane. John Annand and the Glasgow group have built the trigger plane. For experiments which require a cyrotarget, Richard Lindgren and the University of Virginia built a new scattering chamber, shown in Fig. 19, which has a larger vertical opening to match the large out-of-plane acceptance of the BigBite spectrometer. Nilanga Liyanage and the University of Virginia are building the wire chambers. The G_E^n collaboration is constructing the shower calorimeter and is building a polarized ^{3}He target for use with the BigBite spectrometer. William Bertozzi and the M.I.T. Nuclear Interaction Group have taken charge of building and testing the BigBite data-acquisition system. In addition to the groups mentioned above, many members of the BigBite working group have helped build and test the various systems and JLab has done a majority of the design work.

2.6.6 Summary

A flexible, large-acceptance BigBite spectrometer has been constructed for use in Hall A. The spectrometer has been commissioned and the first BigBite experiment, the short-range correlation experiment, started in early January 2005 and will be

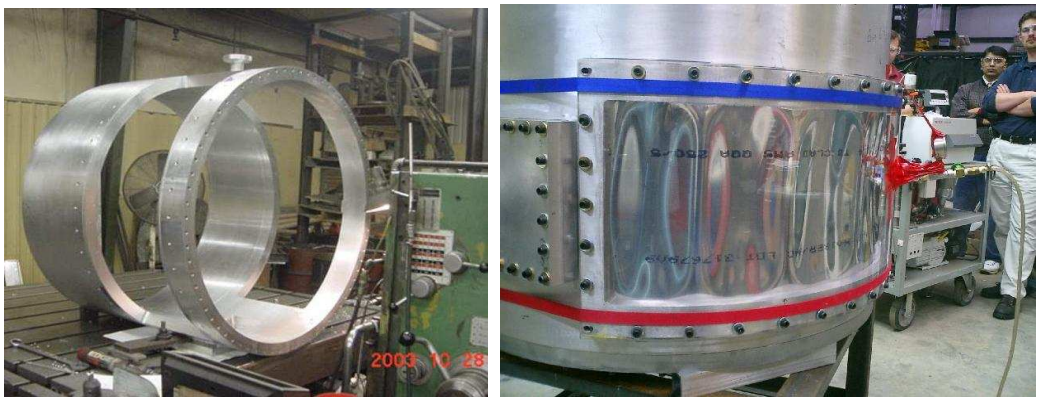

Figure 19: The BigBite scattering chamber while it was under construction (left) and the chamber during its JLab pressure test (right).

completed in mid-April 2005. The second BigBite experiment is expected to be the G_E^n experiment which presently is scheduled to begin installation in early 2006. With five other approved experiments and new experiments being proposed, the BigBite spectrometer is expected to become an integral part of the Hall A physics program for years to come.

Figure 20: The short-range correlation experiment as installed in Hall A. Located left of center is the new scattering chamber which matches BigBite's large out-of-plane acceptance. The BigBite dipole magnet is located right of the chamber with the auxiliary and trigger planes mounted behind.

2.7 BPM Bandpass and Triangular Raster

Contributed by R. Michaels

The implementation of a new triangle-wave raster pattern in late 2003 exposed an old and somewhat forgotten problem with the BPM measurements which affects experiments that need to measure beam position to 100 μm accuracy. This report reminds the collaboration of the history of the raster upgrades and identifies the issues with the BPM electronics.

Recall that the beam is rastered on target with an amplitude of several millimeters to prevent overheating of the target and to reduce the effects of density fluctuations. The raster is a pair of horizontal and vertical air-core dipole magnets located 23 m upstream of the target. Prior to 2003, the raster was used in two different modes, sinusoidal and amplitude modulated. Since then, the raster was upgraded to use a triangle wave pattern. For the old sinusoidal pattern both the X and Y magnets were driven with sine waves with frequencies chosen to not produce a repetitive pattern, i.e. the so-called "TV" pattern. For the old amplitude modulated mode both the X and Y magnets were driven at 18 kHz with a 90° phase between X and Y producing a circular pattern whose radius was amplitude-modulated at 1 kHz. The upgraded triangle wave-pattern raster, invented to Chen Yan and collaborators and provided to Hall A, achieves a uniform rectangular density distribution of beam on the target by moving the beam with a time-varying magnetic field whose waveform is triangular with essentially zero dwell time at the peaks. The electronics design is an "H-bridge" in which switches are opened and closed at 25 kHz, to switch between two directions of current (40 A peak) through the raster coils.

While the new design provides a superior target heating performance, it introduces new problems with the beam position measurements which collaborators should be aware of. The electronics used to process the stripline BPMs have a low-bandpass with a characteristic frequency cutoff of $\nu_0 \sim 30$ kHz. Actually it is a 2-stage amplification with a somewhat complicated transfer function, but we will estimate the effect with a simple transfer function for a low-bandpass filter:

$$f(\nu) = \frac{1}{\sqrt{1 + (\nu/\nu_0)^2}} \tag{1}$$

The rastered magnetic field and hence the position on target is a triangle waveform with frequency $\nu = 25$ kHz and period $T = 1/\nu$ which may be decomposed into a Fourier series to yield the following function of time t:

$$f(t) \quad = \quad \frac{8}{\pi^2} \sum_{\text{odd } n} \frac{(-1)^{(n-1)/2}}{n^2} \sin(\frac{2n\pi t}{T}) \tag{2}$$

Folding Eq. 2 with Eq. 1 leads to the BPM response shown in Fig. 21. The position distribution seen by the BPMs is reduced in amplitude compared to the

true amplitude by a factor of ∼1.5. The shape of the calculated BPM amplitudes looks similar to what is measured with the online program "raster++" except that the real data has more smearing presumably due to resolution of the BPMs. See for example halog 140165 on Jan 27, 2005.

One important implication is that those experiments who care about the position at the ±100 μm level should use the raster pickoff current, calibrated for position and phase shifts, to compute the beam position on target. This procedure has been used before, though it is more complicated and less convenient than using BPM measurements. Clearly an upgrade to faster electronics for the stripline BPMs would be desirable but this is not foreseen at this time.

In 2005 we expect to receive new electronics for the cavity monitor BPMs. They have a 100 kHz bandpass, which using the same calculation leads to a 10% reduction of the BPM measurements. For the "old" sinusoidal raster, the reduction was also about 10%, as was first noted by the VCS experiment. The much larger reduction factor of the triangle raster is due to the high-frequency components that make a triangle.

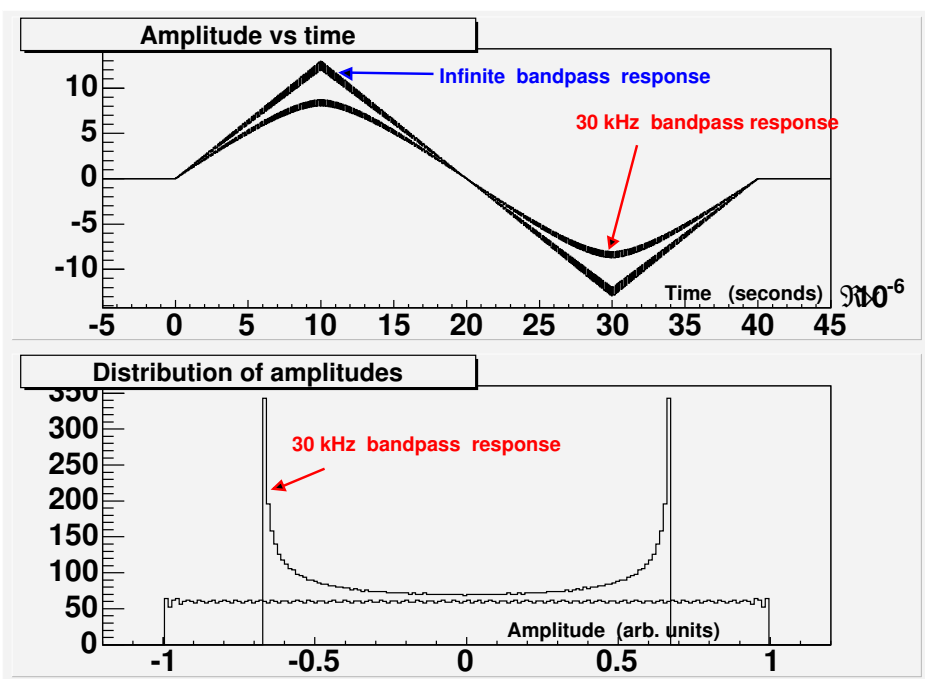

Figure 21: Calculated response of the BPM electronics to the triangle raster wave form. The top figure shows the amplitude vs time for the 30 kHz low-bandpass frequency response that we have. This is compared to an infinite-bandpass response. The bottom figure shows the amplitude distribution that would be observed, e.g. with the online program raster++. It is also compared to the infinite-bandpass result.

2.8 Podd — C++/ROOT Analysis Software

Contributed by J.-O. Hansen

The C++/ROOT-based analysis software package reached maturity during 2004 and has been proven to be suitable for production work. Perhaps the best evidence for this is that all production experiments that ran during 2004, *viz.* E94-107 (Hypernuclear Spectroscopy), E04-012 (Search for Pentaquark Partners), HAPPEx, DVCS, and the Short-Range Correlations experiment (SRC), have used the software package for both their online and offline data analysis.

By popular demand, the C++/ROOT analyzer got a name in 2004: Podd. This is simply a name, not an acronym, although interpretations of it are welcome.

The user community took to the new software with virtually no resistance. New experiments readily adopted the Podd framework as the de facto standard. This can certainly be attributed in part to the familiarity of younger collaborators with C++ and possibly ROOT.

As part of their analysis work, the experiments running in 2004 developed several major extension packages for Podd: Analysis code for the RICH detector was finalized by E94-017 and E04-012. Extensive code for the analysis of their special detector system was merged into Podd by DVCS. Likewise, the SRC experiment developed a complete new package for the analysis of the BigBite spectrometer. (HAPPEx only used Podd for the spectrometer data analysis, not for the parity-violating asymmetry measurements.) These contributions could be seamlessly integrated into Podd as external, experiment-specific plug-in modules, while the core Podd code base remained un-touched. The notorious code-base splintering ("private versions"), which was common with the old software ESPACE, was completely avoided.

In part motivated by the needs of the running experiments, the core part of Podd was continuously improved throughout the year. Each experiment used a certain major release of Podd, and updates/patches to that release were kept binary-compatible to the base version, allowing the Podd shared libraries to be updated live and without any need for users to recompile their experiment-specific modules. Release 1.1.0, completed in November 2003, was used by E94-107 and was developed up to version 1.1.12, published in February 2004. E04-012 used Release 1.2.0 (April 2004) with updates up to 1.2.8 (June 2004). Subsequent experiments used Podd version 1.3.0 (June 2004) and 1.3.1 (September 2004).

Many limitations of the early versions of Podd have been removed with the more recent releases. For example, beam information (momentum vector magnitude and direction) can be passed through the physics module chain and be modified by corrections modules. One application of this is energy loss corrections, which are now available in Podd via several physics modules. Furthermore, event filtering is now possible, allowing copying of raw data events from one CODA file to another according to cuts on analyzed quantities. ROOT objects can now

be written to the output file. Analysis of scalers is fully implemented, including modules for deadtime calculations. Similarly, slow control (EPICS) data are now properly handled. EPICS quantities can be used in tests and cuts, and both scaler and EPICS records can be written to the output ROOT file. ROOT version 4 is supported, which allows the writing of ROOT files larger than 2 GB in size. Podd is officially supported on Linux and Solaris platforms, and there are unofficial ports to IRIX and MacOS X.

As an experimental feature, a custom "decoder" has been written that allows input of digitized simulation data into the Podd analysis chain. As with software for experiment-specific experimental equipment, such a simulation front-end is implemented as a plug-in module that can be developed independently of the core Podd system. Tests with simulated idealized VDC data demonstrated perfect track reconstruction. This makes possible studies of the performance of the tracking code in the presence of noise, degraded resolution, and spurious tracks, for example. These studies will be carried out as time permits.

As part of the commissioning efforts for the septa, the optimization routines that were available for ESPACE have been adapted to the Podd framework. For this purpose, an external optimization program, `optimize++`, is available. It is now possible to perform the entire optics optimization procedure within the ROOT/C++/Podd environment, avoiding any legacy FORTRAN software.

In 2005, efforts will focus on documentation and possibly on improvements of the VDC tracking code. Up-to-date information about this project can be found on the Web [26]. Our manpower is very limited, and volunteers are always welcome to join, especially those with some background in C++ programming.

The work reported here was carried out in collaboration with R. Feuerbach and R. Michaels from Hall A. Contributions from and discussions with F. Cusanno, M. Iodice, N. Liyanage, V. Mamyan, Yi Qiang, B. Reitz, K. Rossato, V. Sulkosky, and G. Urciuoli are gratefully acknowledged.

2.9 Hall A Luminosity Monitor for Parity-Violating Experiments

Contributed by R. Suleiman

A new set of luminosity monitors (lumis) have been installed on the beam line downstream of the target. There are two sets: one at 0.5° and one at 45° scattering angles. The most forward-angle detectors (blumi) will provide strong sensitivity to noise in beam parameters (more sensitive than the primary detectors), but because they are located downstream of significant amounts of iron in the field of the septum magnet, they are not useful for as a true "false asymmetry" measurement. The signal in blumi set of detectors is dominated by Møller and elastic electrons. The larger-angle set (flumi) will monitor density fluctuations in the target and provide a test of electronics false asymmetry with an extremely narrow width signal. The signal in flumi set of detectors is dominated by low energy electrons. Each detector in both sets will be receiving rates in the range of 10 GHz at the HAPPEx luminosity and a radiation dose of few MRads per day.

The monitors consist of individual small quartz Čerenkov detectors made of Spectrosil 2000 quartz material with air light guides made of Anolux Miro IV PVD aluminum to direct photons to a PMT. The blumi uses an 8-stage 2-inch R7723 PMT with quartz windows for improved radiation resistance while the flumi uses the same PMT type but with UV glass window for improved radiation resistance with better resistance for helium gas penetration. The flumi PMTs were shielded with 4 inches of lead bricks. No lead shielding was put around the flumi PMTs, although some shielding was provided by the septum and the first quadrupole magnets of the HRSs. All PMTs were flushed with nitrogen gas to protect against helium damage. The signals were carried with twinax shielded (Belden 9207) cables from Hall A exit beam pipe to the right HRS where current-integrating ADCs were used for readout. To reduce further the electronic noise, a 100 pF capacitor was put between the PMT-BNC ground and the twinax cable ground to isolate the ground loops.

Eight such detectors were installed in the low-angle lumi, which sits approximately 7 m downstream of the target, see Fig. 22 and Fig. 23, while the large-angle lumi consists of 2 detectors about 1 m from the target. All the detectors in both sets of lumis were installed before HAPPEx 2004 run. Fig. 24 shows lumi widths versus beam current during a hydrogen run. The lumi widths versus the fan speed during a hydrogen run is shown in Fig. 25.

The presence of the septum structure and field between the target and the detectors modified the observations of each of the forward-angle detectors; for example, the expected azimuthal symmetries in these detectors were not evident. This system performed as required and no significant upgrades are expected before the next HAPPEx run.

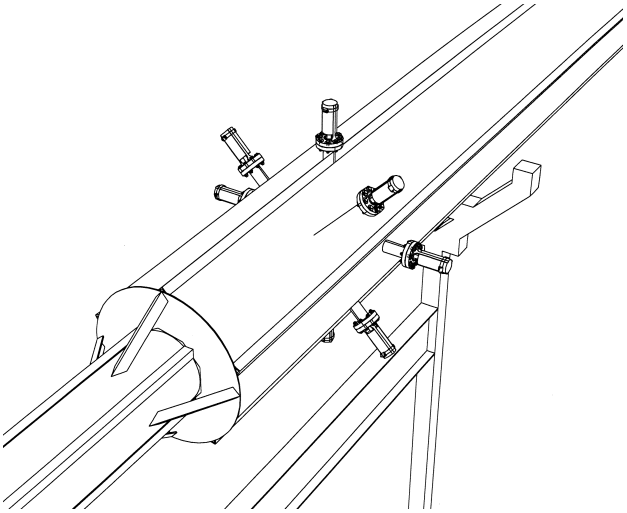

Figure 22: Drawing of the forward-angle lumi and the exit beam pipe.

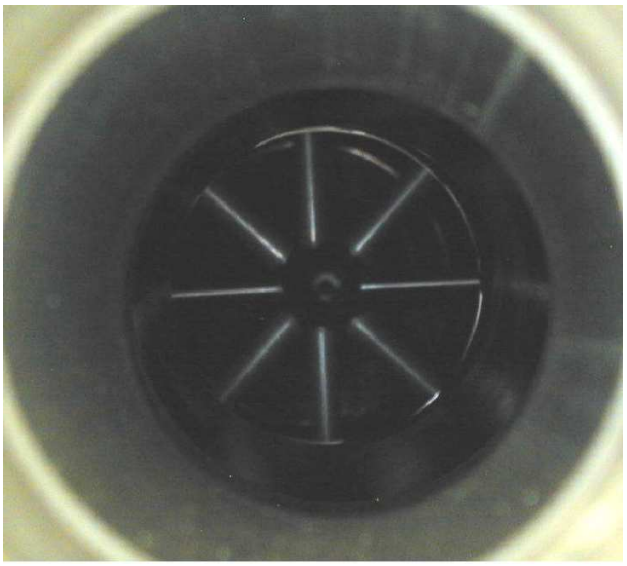

Figure 23: Picture of the inside of the exit beam pipe showing the 8 cups where the lumi detectors were put in.

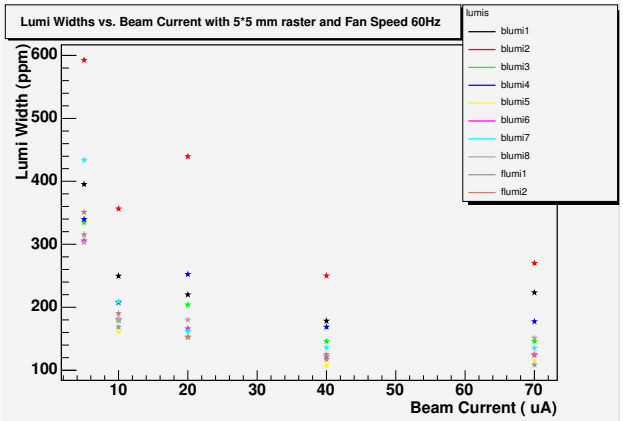

Figure 24: The lumi widths versus beam current during a hydrogen run in summer 2004.

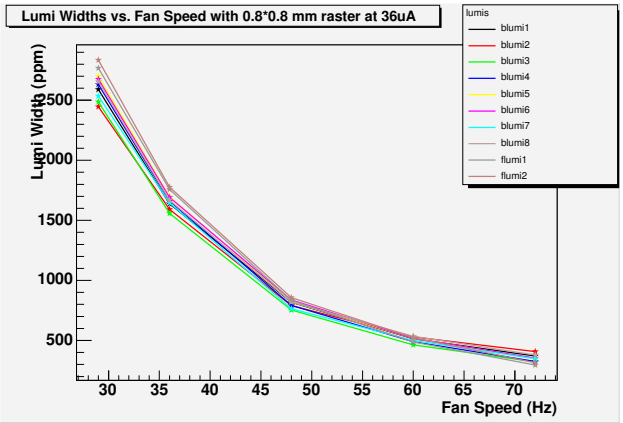

Figure 25: The lumi widths versus the target fan speed during a hydrogen run in summer 2004.

2.10 Instrumentation for the G_E^n (E02-013) Experiment

Contributed by B. Wojtsekhowski

Experiment overview Measurement of the neutron electric form factor will be done using a polarized ^{3}He target and polarized electron beam for Q^2 up to 3.4 $(GeV/c)^2$ with expected accuracy shown in Fig. 26. An optimized experimental

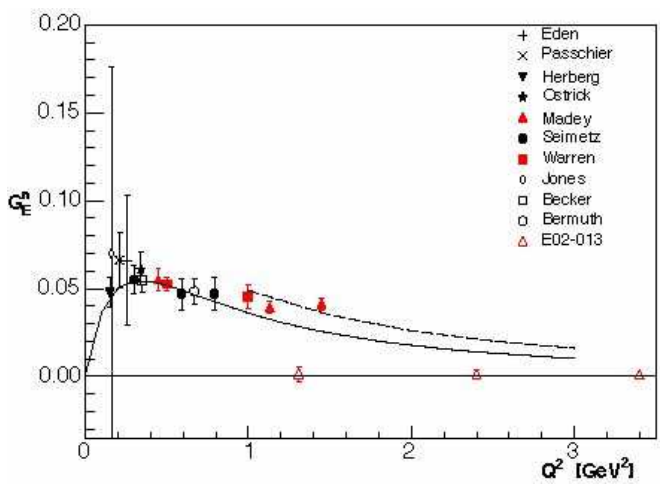

Figure 26: World data on the neutron electric from factor with planned values of Q^2 in E02-013 and expected accuracy of results.

setup consists of the BigBite spectrometer, with a solid angle of 76 msr, a 40 cm long target, and a large neutron detector. This system will operate at a luminosity of 10^{37} Hz/cm^2 and will provide a Figure-of-Merit which is at least 25 times larger than that of any other known G_E^n experiments.

Collaboration Last year the collaboration had a large number of biweekly meetings and one general meeting on 12/14. detailed information about these meetings can be found at http://hallaweb.jlab.org/experiment/E02-013. The five Ph.D. students on the E02-013 experiment are N. Thompson (Glasgow University), S. Riordan (Carnegie Mellon University), A. Kelleher (College of William and Mary), A. Kalarkar (University of Kentucky), B. Craver (University of Virginia).

Beam tests An additional beam test was performed on 02/01/05 with a prototype neutron detector N-20 detector and HRS-L. Data were collected at 4.6 GeV beam energy for the processes H(e,e'p) and D(e,$\pi^- n$). The information will allow us to investigate detector time resolution, veto efficiency, neutron detection efficiency, and the effect of hadronic interactions in the detector steel structure.

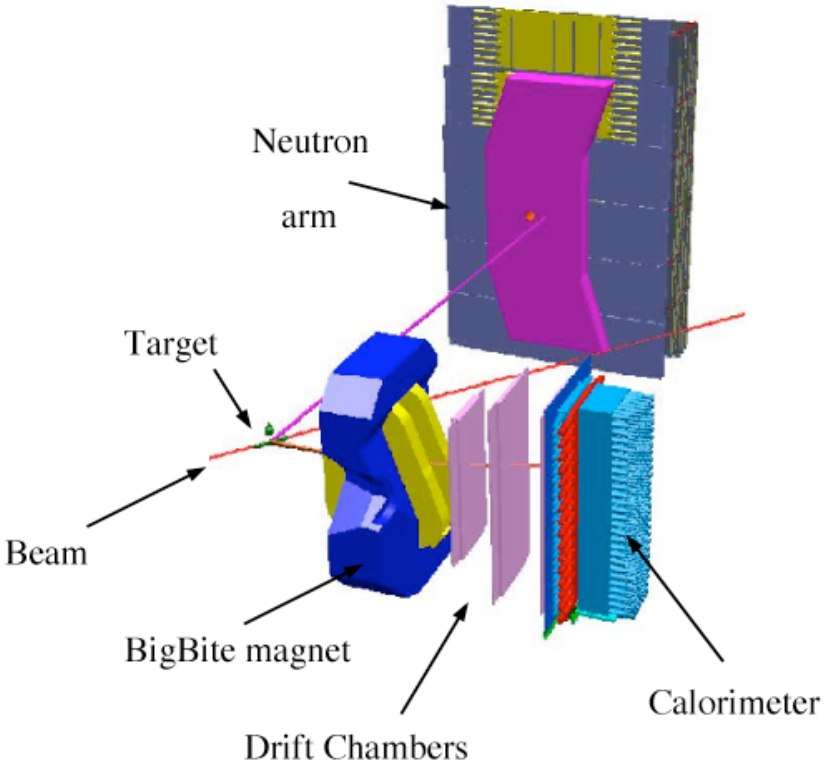

Figure 27: Schematic layout of experiment E02-013.

Design The design of both detector arms has been completed. The steel holders for the lead wall still have to be ordered. The concept of the target has been finalized. An initial design of the high temperature oven has been completed. A long list of remaining design projects includes the target ladders, target alignment systems, the beam line elements, a final design of the oven, and laser light optics.

Target A special magnet was constructed. Field characteristics were found to be in good agreement with the calculations. A technology for a novel hybrid (K+Rb) cell of polarized He-3 was developed. Several cells were produced and tested at UVA. Field sweep NMR was realized for the ^{3}He target at KU and W&M. A high temperature oven was designed and a prototype was constructed.

The fibers for transmission of polarized light from the lasers to the target were obtained and tested. A device to merge five fibers into one was tested. A new building for the lasers and target tests is under construction. Its expected completion will allow the magnet to be installed in this building in April 2005.

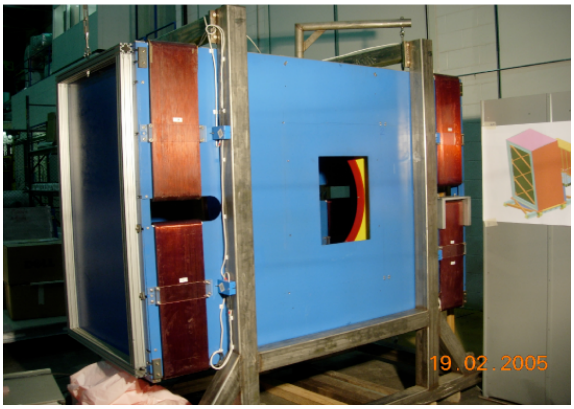

Figure 28: Magnet for the polarized target.

Electron arm detectors The frame for the detector package has been constructed. The first wire chamber for BigBite has been mounted on the frame. A cosmic test of this chamber is underway. A test in Hall A at full luminosity is expected in spring 2005. The second chamber is operational at UVa. All planes of the third chamber have been constructed. A calorimeter for the trigger and electron identification has been assembled. Construction of the timing plane and of the preshower plane is expected to be done in May 2005.

Neutron arm detectors All cassettes, in which the neutron and veto counters will be placed, have been constructed. The first 100 counters have been installed in the cassettes (see Fig. 32). Seventy five more counters have been tested and are ready for installation. The remaining 69 counters are expected to be ready for installation in April-May 2005. All 192 veto paddles have been constructed and tested. The first group of veto paddles installed in cassette is shown in Fig. 33.

Electronics Detailed schematics have been developed. All electronics modules are in house. Assembly of the full electronic system will start in May after completion of the SRC experiment, which is using a large portion of the electronics needed.

Figure 29: A hybrid (K+Rb) cell with ^{3}He

Software Components of the analyzer have been written. Data from the N-20 detector test run will be used for debugging the software.

Figure 30: A prototype high-temperature oven.

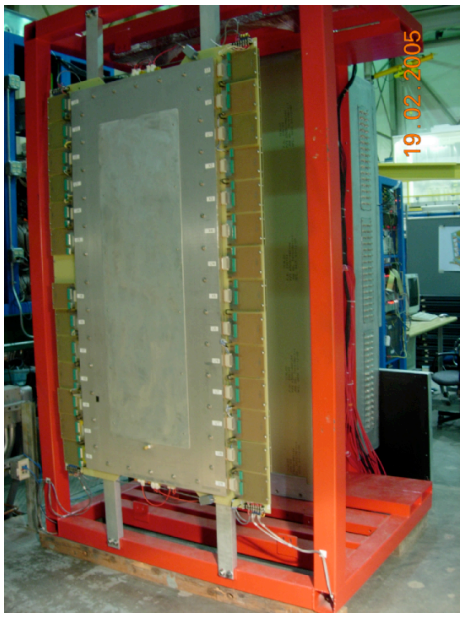

Figure 31: BigBite detector frame with the first drift chamber installed.

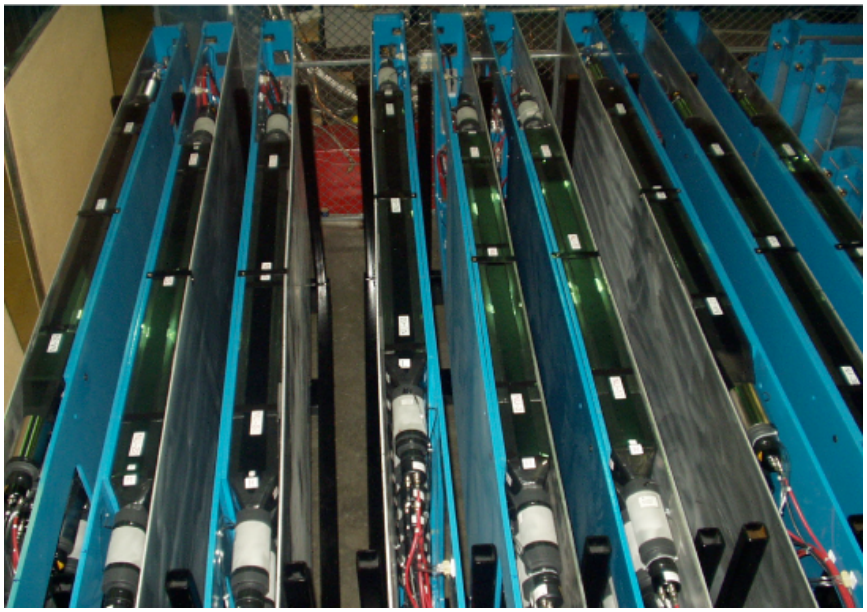

Figure 32: The neutron bars in the cassettes.

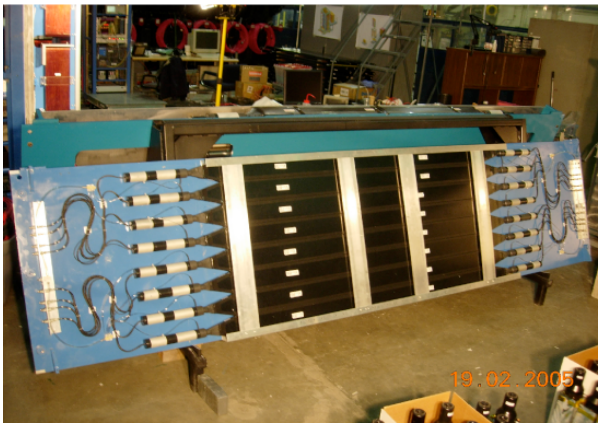

Figure 33: The veto paddles in the cassette.

3 Summaries of Experimental Activities

3.1 E89-044

The ^{3}He(e,e′p) Reaction at High Momentum Transfer

M. Epstein, A. Saha, and E. Voutier, spokespersons,
and
the Hall A Collaboration

The goal of the E89-044 experiment is to investigate the response of the ^{3}He nucleus to electromagnetic excitations in the quasi-elastic regime. The experiment took data from December 1999 to April 2000, in perpendicular and parallel kinematics, exploring the 2-body and 3-body electro-disintegration of ^{3}He through the (*e,e'p*) process.

The analysis of the experiment in the different channels has been completed and 3 Ph.D. theses have been defended: Marat Rvachev (MIT, 2003), Emilie Penel-Nottaris (LPSC Grenoble, 2004), Fatiha Benmokhtar (Rutgers, 2004). Two articles [27, 28] have been submitted to Physical Review Letters describing the experimental results in the continuum region and in the 2-body breakup region of ^{3}He. The continuum paper has recently been published. An additional short communication on the by-product ^{3}He(e,e′d) process is foreseen. The conclusion of these studies is that the reaction process at quasi-elastic kinematics is dominated by final- state interactions in the form of on-shell nucleons and pion propagation in the nuclear medium at very high momentum. Several calculations in different frameworks confirm these results: a Glauber calculation from R. Schiavilla *et al.*, a relativistic approach from J. Udias *et al.*, a generalized eikonal approximation from C. Cioffi degli Atti *et al.*, and a diagrammatic expansion from J.-M. Laget.

Work remains to be done for the parallel kinematics where a first attempt at the separation of the longitudinal and transverse response functions at small missing momenta indicated problems that need to be addressed. This will be done during the current year in close collaboration with Rutgers University, with the aim of definitely determining our capabilities to perform the LT separation in the Q^2 range 1-4 GeV^2. In addition, the response function separation for the continuum region data will be completed in 2005.

3.2 E91-011

Investigation of the $N \to \Delta$ Transition via Polarization Observables in Hall A

S. Frullani, J.J. Kelly, and A.J. Sarty, spokespersons,
and
the Hall A Collaboration.

We have measured recoil polarization in the $p(\vec{e}, e'\vec{p})\pi^0$ reaction at $Q^2 \approx 1$ GeV^2 near the Δ resonance, obtaining angular distributions for a total of 16 independent response functions. The past year has been spent trying to resolve inconsistencies between polarizations and response functions extracted using the method of maximum likelihood. The primary problem is that response functions deduced from the ϕ dependence of polarization data do not always agree well enough with response data extracted directly from replaying the raw data. We wrote a new streamlined version of the analysis code in C++, called PALM++, and performed many internal consistency checks. The most important pseudo data test uses the acceptance-rejection algorithm to replace measured values for $(\theta_{fpp}, \phi_{fpp})$ with a simulated distribution based on a model with known polarization at the target. The reliability of the polarization and response data can then be gauged by analyzing the pseudo-data like real data. We found that the extracted responses reproduce acceptance-averaged model responses but that the extracted polarizations sometimes do not. The pattern of problems in the polarization pseudo-data is the same as for the real data. The most important problem for polarization appears to be binning with respect to ϕ_π — the most difficulty is encountered for (W, Q^2, x) bins in which scatter plots of the ϕ_π dependence of spin-transport matrix elements are broad. Extracted response functions are more reliable because the ϕ_π dependence is accommodated event-wise without binning. Therefore, we have abandoned binned polarization and are focusing on completing the analysis of the response data.

Previous versions of the analysis reported 5 bins in W times 2 bins in Q^2. However, the Q^2 dependence is relatively mild while the W dependence across the resonance would benefit from a finer spacing. Therefore, more recent analyses employ 10 bins in W for $Q^2 = 1.0 \pm 0.2$ GeV^2. Corrections for the differences between central and acceptance-averaged kinematical variables are made according to

$$R(W, Q^2, \bar{x}, \bar{\epsilon}) = R(\overline{W}, \overline{Q^2}, \bar{x}, \bar{\epsilon}) - \frac{\partial R}{\partial W}(\overline{W} - W) - \frac{\partial R}{\partial Q^2}(\overline{Q^2} - Q^2) \qquad (3)$$

where overlines indicate acceptance averaging and where the derivatives are evaluated at central kinematics using a model, such as MAID. The primary effect is to compensate for the x dependence of $\overline{Q^2}$ which, though small, reduces systematic irregularities in the data. This procedure is illustrated in Fig. 34 using pseudo-data. The open squares show raw response functions extracted from pseudo-data while open red circles show acceptance-averaged response functions from

MAID2000. The agreement between these data sets, modulo statistical fluctuations, demonstrates the internal consistency of the simulation/analysis program. However, the x dependence of $\overline{Q^2}$ can produce significant systematic deviations from the input model (solid curves) evaluated at central kinematics, especially for R'^t_{TT}. Recognizing that $\overline{Q^2} \approx 0.94$ for $x > 0.5$ or 1.06 GeV^2 for $x < -0.5$, we observe that the pseudo-data for R'^t_{TT} do cluster around the model curve for the appropriate Q^2. Even the abrupt transition across $x = 0$ is reproduced. The solid circles show that "centered" pseudo-data adjusted according to Eq. (3) cluster better around the model curves for central kinematics. Therefore, distortion of multipole amplitudes by the x dependence of $\overline{Q^2}$ should be minimized by fitting centered data.

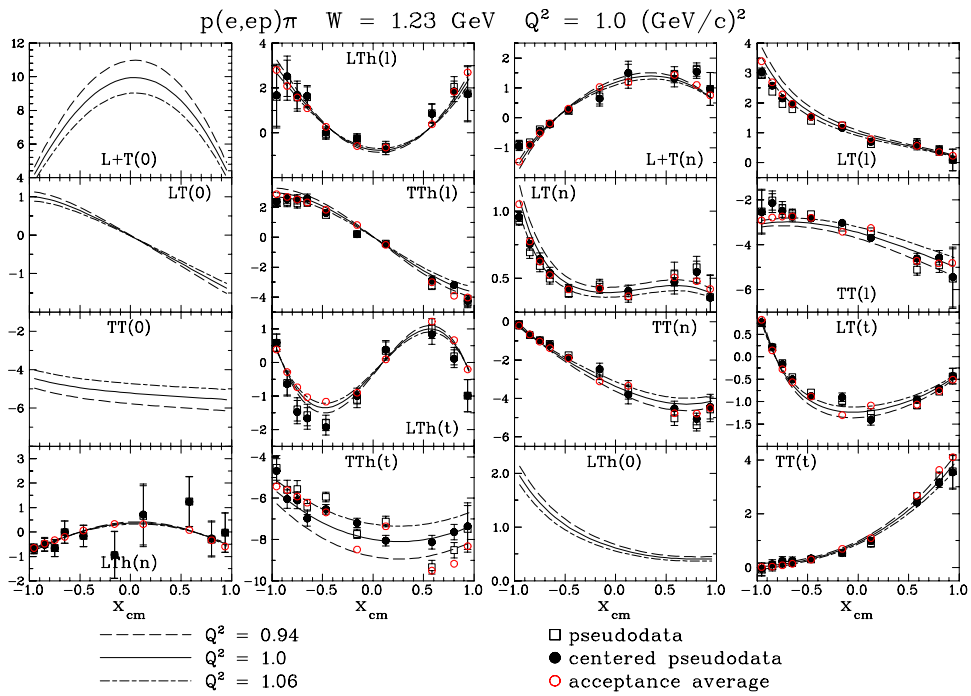

Figure 34: Pseudo-data for response functions at $W = 1.23 \pm 0.01$ GeV and $Q^2 = 1.0 \pm 0.2$ GeV^2 are compared with the input model (MAID2000) at the central kinematics and neighboring values of Q^2 representative of the x dependence of acceptance averaging. See text for details.

Response functions for $W = 1.23$ GeV are compared in Fig. 35 with representative models: MAID2003 [29], DMT [30], SAID [31], and Sato-Lee [32]. (Note that this representation removes leading $\sin\theta_{cm}$ dependencies.) The first two columns are governed by real parts of interference products which emphasize resonant amplitudes with relatively little model dependence whereas the last two columns based upon imaginary parts emphasize non-resonant amplitudes and dis-

play much more variation among models. None of the current models provides a uniformly good fit to these data. The solid red curves show a multipole analysis that begins with a baseline model and fits adjustments to selected multipole amplitudes. To minimize bias, we start with Born amplitudes for pseudovector coupling. All s- and p-wave amplitudes plus the real parts of $2-$ amplitudes were fit. Imaginary parts of $2-$ amplitudes are small for all models considered and the data show little sensitivity to variation of $2+$ or higher partial waves. The resulting fit reproduces the data well, with $\chi^2_\nu = 1.5$.

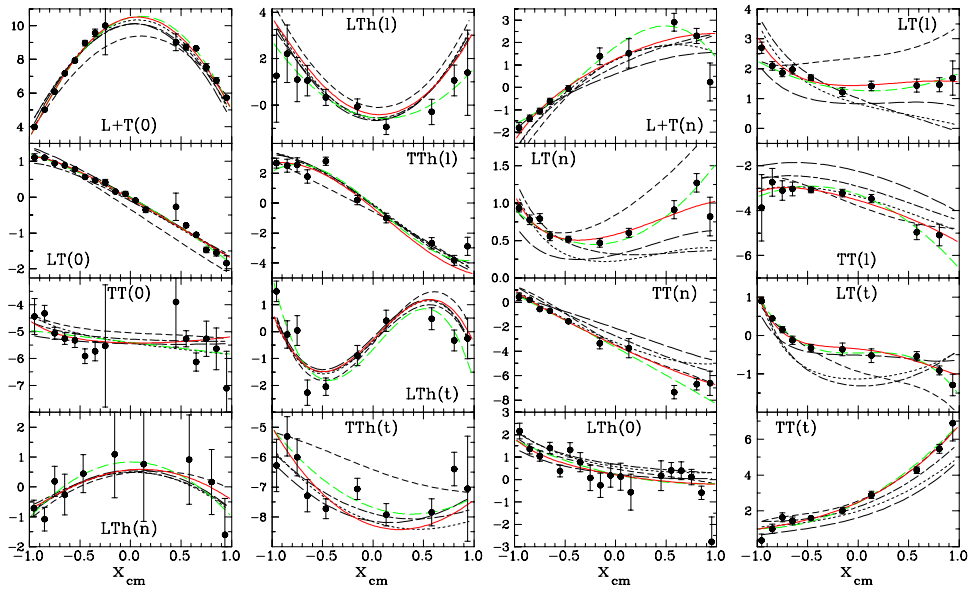

Figure 35: Response functions at $W = 1.23$ GeV are compared with recent models and with fits. The units are μb. The labeling distinguishes L, T, LT, and TT contributions to the unpolarized (0) cross section and to transverse (t), normal (n), or longitudinal (l) components of recoil polarization with an h to indicate helicity dependence, if any. Linear combinations that cannot be resolved without Rosenbluth separation are identified by L+T. Black dash-dotted, dotted, short-dashed, and long-dashed curves represent the MAID, DMT, SAID and SL models, respectively. The green mid-dashed curves show a Legendre fit while the solid red curves show a multipole fit.

Fitted multipole amplitudes are compared in Figs. 36-37 with representative models. The anomalies at $W = 1.29$ GeV are caused by a couple of data points with inexplicably small error bars that suggest a matrix inversion problem in PALM++; further investigation is needed to resolve that issue. The fitted $1+$ amplitudes show the Δ resonance clearly without coaching. Model variations are relatively small for M_{1+} and S_{1+}, but there is significant variation for E_{1+} with the fit tending to disfavor SAID. The spread among models is especially large

for 1− amplitudes, the partial wave in which the Roper resonance is supposed to live, and the data disfavor SAID rather strongly. Interestingly, the fitted M_{1-} amplitudes are closer to the Born model than to the more sophisticated isobar or dynamical models, but the present precision does not exclude MAID or DMT. Conversely, the slope in $\Re S_{0+}$ is similar to SAID and opposite the Born model.

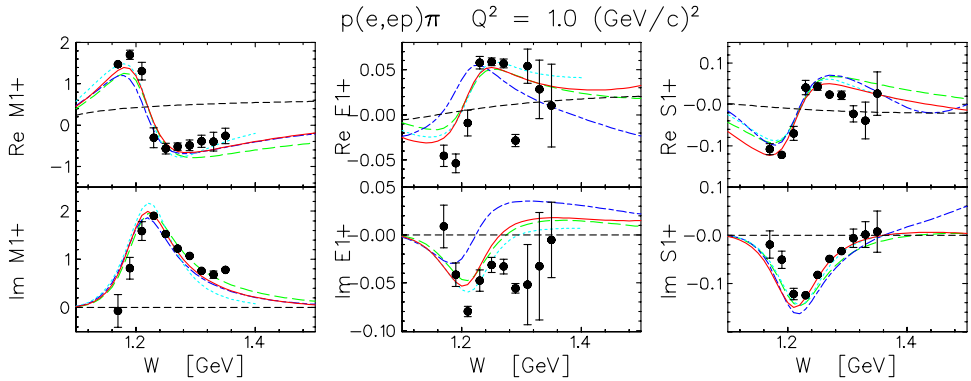

Figure 36: Fitted 1+ multipole amplitudes are compared with MAID2003 (red solid), DMT (green dashed) , SAID (blue dash-dot), and SL (cyan dotted) models. Black short-dashed curves show Born baseline amplitudes.

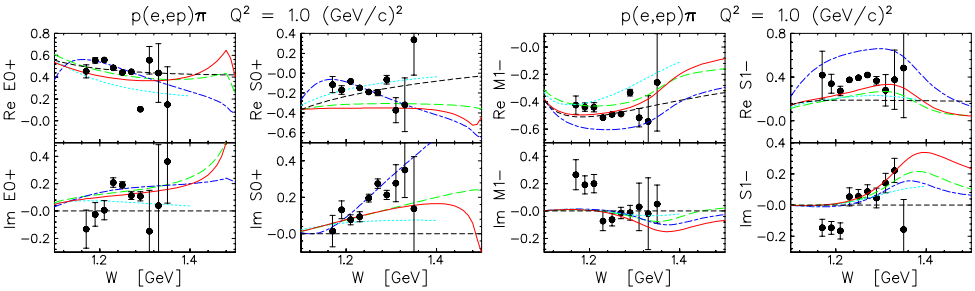

Figure 37: Fitted 0+ and 1− multipole amplitudes are compared with MAID2003 (red solid), DMT (green dashed) , SAID (blue dash-dot), and SL (cyan dotted) models. Black short-dashed curves show Born baseline amplitudes.

We are now working on final details of the data analysis and on evaluation of systematic errors in response functions and multipole amplitudes. Drafts of a PRL paper on the quadrupole ratios and an archival PRC paper have been prepared and we hope to circulate them within the Hall A collaboration long before the next progress report is due.

3.3 E94-107

High-resolution hypernuclear $1p0$ shell spectroscopy

S. Frullani, F. Garibaldi, J. LeRose, P. Markowitz, spokespersons

Introduction The Lambda hypernucleus, a nuclear system with strangeness S=-1 in which the Lambda hyperon replaces one of the nucleons, is a long-living baryon system and provides a variety of phenomena. The strange quark is an impurity in the system and the study of its propagation can reveal configurations or states not seen in other ways. The study also gives interesting important insight into the structure of ordinary nuclear matter. The hyperon is not excluded from the filled nucleon orbitals by the Pauli principle and can penetrate deep inside the nucleus. Moreover, the high-resolution spectroscopic study of light hypernuclei allows access to important information on the nature of the force between nucleons and strange baryons, i.e. the $\Lambda - N$ interaction. The nucleus provides a unique laboratory for this study. From low-energy $\Lambda - p$ scattering studies we obtained information about the s-state $\Lambda - N$ interaction, but the non-central part of the $\Lambda - N$ force is not well established. Especially useful information comes from the spin-dependent part of the interaction [33]. Hypernuclear experimental studies up to now have been carried out essentially by hadron-induced reactions with limited energy resolution (1.5 MeV at the best). Moreover, the spin-flip transition excitation was weak so doublets have not been detected. In the electromagnetic case, the spin-flip transitions are strong, so doublet-splitting detection is possible in principle because both members are populated. The disadvantage of smaller electromagnetic cross sections is partially compensated by the high-current, continuous beam available at JLab. The feasibility of these experiments has been recently demonstrated by the Hall C E89-009 experiment [35]. The aim of the Hall A experimental program is the first "complete" study in $1p$ shell nuclei: ^{9}Be, ^{12}C, ^{16}O [7]. A missing-mass resolution as good as 350 keV - 400 keV (FWHM) can be attained, with a beam energy stability of 2.5×10^{-5} (σ_E/E) and the High Resolution Spectrometers (HRS) momentum resolution, $\Delta p/p \simeq 10^{-4}$ (FWHM) [40]. In the following we describe the experimental difficulties and the challenging modifications made to the Hall A apparatus. Then, preliminary results on ^{12}C and ^{9}Be will be presented.

The experiment The experiment took place in JLab Hall A. The HRS spectrometers were used to detect the electrons and kaons. In order to get reasonable counting rates the electron scattering angle has to be small to get a high virtual photon flux and the kaon angle has to be close to the virtual photon direction to minimize the momentum transfer. The momentum transfer to the hypernucleus in electroproduction is rather large and decreases steadily with increasing energy

of the virtual photon so high energies are preferable. Since the cross section depends strongly on Q^2, the measurements have to be made at low Q^2. To keep a reasonable kaon survival fraction the kaon momenta have to be fairly high. Scattering angles of 6° for both electron and kaons, an incident energy of 3.77 GeV, a photon energy of 2.2 GeV, a scattered electron momentum of 1.86 GeV/c, a kaon momentum of 1.96 GeV/c, and $Q^2 = 0.079$ GeV^2 have been used. The expected counting rates for the two nuclei are reported in Table 5 . The C4 model [36] of the elementary process is used in the calculation. The electron-nucleus lumi-

Background	(Hz)	^{12}C$(e,e'K)^{12}$B$_\Lambda$			^{9}Be$(e,e'K)^{9}$Li$_\Lambda$		
(e,e')	$1.5 \cdot 10^5$	E	J	counts	E	J	counts
(e,π)	$2.0 \cdot 10^5$	(MeV)		(per hour)	(MeV)		(per hour)
(e,K)	$3.6 \cdot 10^3$	0	1^-	5.9	0	$3/2^+$	1.78
(e,p)	$1.8 \cdot 10^5$	0.03	2^-	34.6	0.69	$5/2^+$	9.7
(e,e'π)	$\sim 1.0 \cdot 10^2$	2.54	1^-	14.9	1.42	$1/2^+$	1.95
(e,e'K) (QF)	$\sim 0.1 \cdot 10^1$	5.46	2^-	4.5	1.71	$3/2^+$	2.8
(e,e'p)	$\sim 5.0 \cdot 10^1$	6.04	1^-	1.0	2.43	$5/2^+$	1.07
		10.03	3^+	5.8	2.78	$7/2^+$	3.04
		10.63	3^+	27.1			

Table 5: Expected single and random coincidence rates compared to the ^{12}C$(e,e'K)^{12}$B$_\Lambda$ and ^{9}Be$(e,e'K)^{9}$Li$_\Lambda$ events.

nosity, obtained with a constant beam current of 100 μA and target thickness of 100 mg/cm^2, ranges from 2.4×10^{36} to 5.4×10^{36} cm^{-2}s^{-1}. The single and accidental coincidence counting rates are about constant for all the investigated nuclei and the numbers reported in Table 5 represent upper limits for our conditions.

Experimental challenges

Forward angle. Septum magnets In order to allow experiments at very forward angles, smaller than the actual HRS minimum angle (12.5°), two septum magnets were added to the HRSs. The two magnets deflect particles scattered over angles as small as 6° in order to make their trajectories overlap with trajectories detectable by the HRSs. This overlapping as well as the room for the septum magnets has been achieved by moving the target upstream. The chosen target shift makes the new HRS angular acceptance $\sim$ 4.5 msr and the maximum field $\sim$ 3.3 T. The septum magnetic length is 84 cm. This new spectrometer configuration provides a general purpose device that extends the HRS features at small scattering angles [39] while maintaining the HRS optical performance.

The challenge of Particle IDentification As previously mentioned a very powerful PID system is mandatory for this experiment. In the electron arm Čerenkov counters were expected to give pion rejection ratios up to 10^3. The

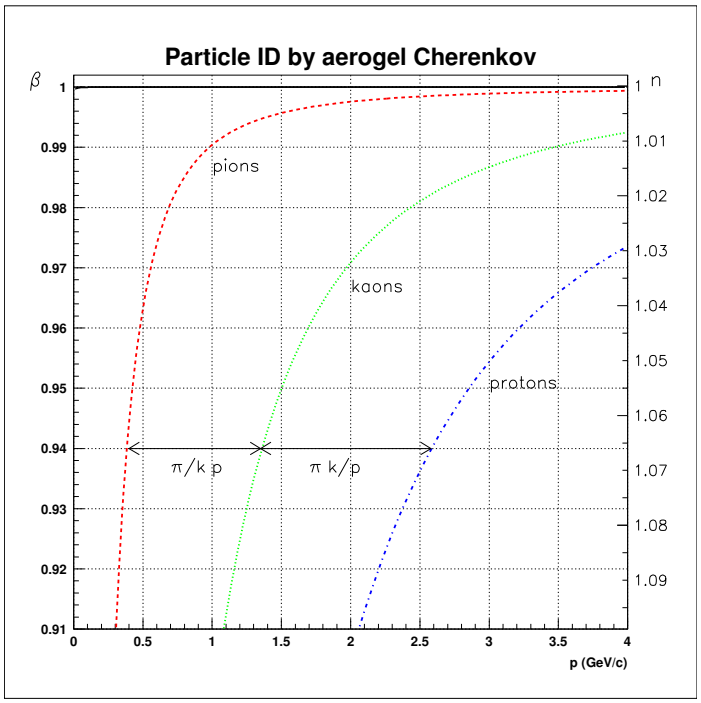

Figure 38: PID with threshold aerogel Čerenkov counters.

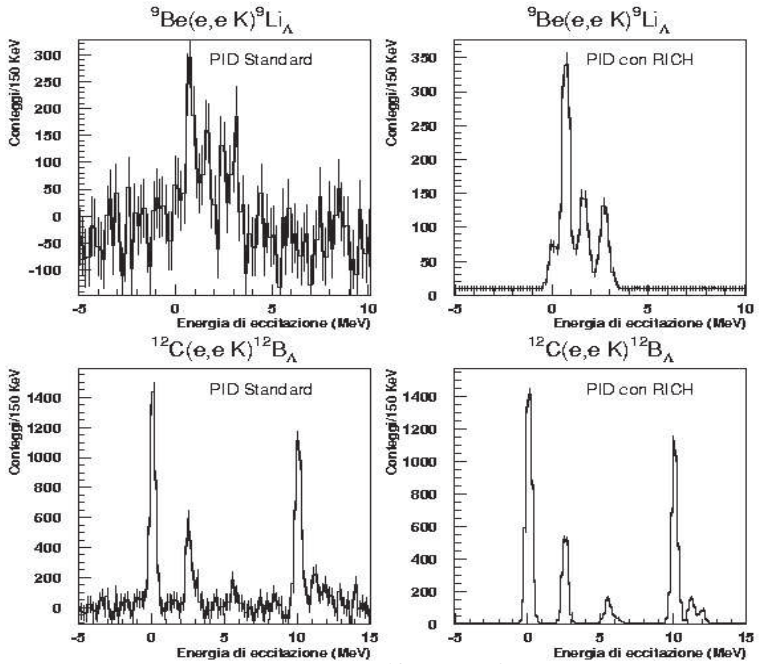

Figure 39: Hypernuclear spectra of ^{12}C and ^{9}Be with and without RICH.

dominant background (knock-on electrons) can be reduced another 2 orders of magnitude by the lead glass shower counters, giving a total pion rejection ratio $\geq 10^5$. In the hadron arm two aerogel Čerenkov counters with $n = 1.015$ and $n = 1.055$ have been used. Figure 38 shows the velocity β vs the momentum of pions, kaons and protons. With the choice of $n = 1.05$ it is possible to separate kaons (above threshold) from protons (below threshold) in the range 1.6 - 3.0 GeV/c. Using n = 1.01 allows the separation between pions and kaons so that with the combination of the two, kaons can be identified. Neverthless, it has been shown that TOF and threshold Cherenkov counters are not sufficient for the unambiguous kaon identification needed to obtain "background free" missing mass spectra.

Improving the PID: RICH detector Simulations performed to understand how to improve the kaon identification capability showed that a Ring Imaging Čerenkov (RICH) detector would provide the required PID capability. Figure 39 shows the advantage of using the RICH. It can be clearly seen, in the case of ^{9}Be$_\Lambda$ how the low signal to noise ratio makes the spectroscopic measurements particularly hard. A clear assignment can be only given to the second component of the first doublet, losing any (important) information on the position of the first component. It should be realized that a standard PID system capable of rejecting pions and protons only at a 95% level is probably not enough to extract

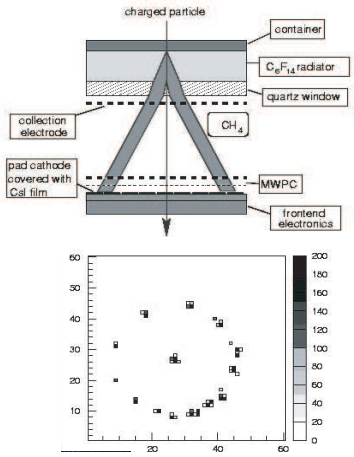

Figure 40: RICH scheme and event display.

outstanding physics information. The choice was a proximity focusing CsI/freon gaseous detector. The RICH discriminates particles by differentiating between different values of Čerenkov emission angle. The Čerenkov radiation, emitted in a trasparent medium (the radiator) whose refractive index is appropriate for the range of particle momentum being specifcally studied, is transmitted through optical elements, which could be either focusing with a spherical or parabolic mirror or not focusing (proximity focusing), onto a photon detector that converts photons into photoelectrons with high spatial and time resolution (Fig. 40). In our case the proximity-focusing geometry was chosen. The Čerenkov photons, emitted along a conic surface in the radiator (C_6F_{14} with n=1.29), chosen because of the momentum of the particles to be identified (2 GeV/c), are refracted by the freon-quarz methane interfaces and strike a pad plane after traveling through a proximity gap of 10 cm filled with methane. A dedicated evaporation facility, with on-line quantum efficiency (QE) measurement capability was built for this [41].

Detector performances In Fig. 41 the Time of Coincidence (TOC) spectra between the electron and the hadron arm are shown. The top left spectrum is

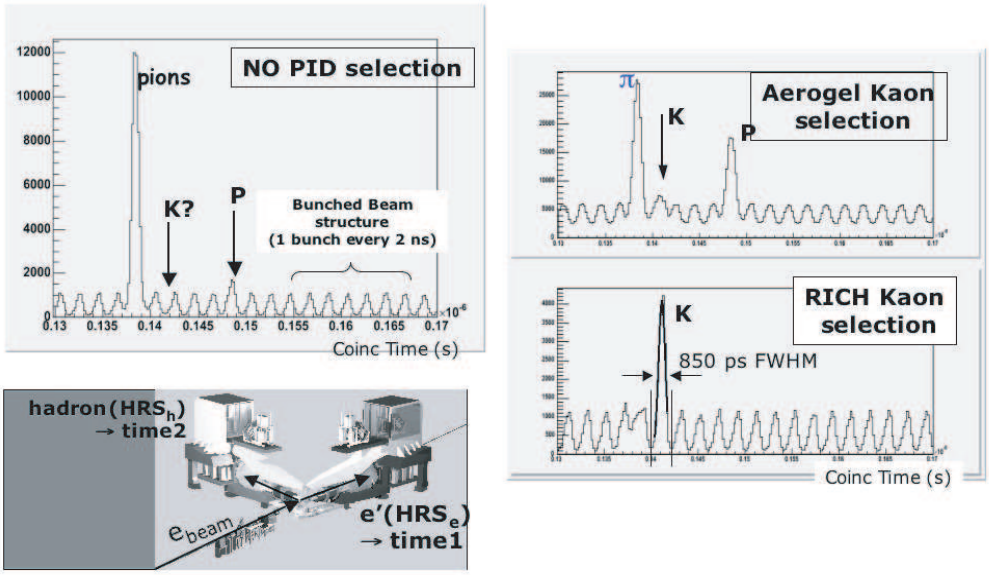

Figure 41: The role of the RICH for kaon identification: many pions and protons are still present if RICH cuts are not applied.

obtained without any PID selection. Kaons are not visible. In the top right plot the aerogel kaon selection is applied showing that kaons are barely visible. When the RICH selection is applied (bottom right plot) only the kaon contribution survives. In Fig. 42 the RICH performance is shown: a separation of pions from kaons at level of 6 σ has been attained. The role of the detector in cleaning up the pion and protons is evident. A rejection factor of 1000 for pions has been measured. It should be considered that the RICH analysis has not been fully optimized yet.

Preliminary results The physics information that can be extracted from the spectra strongly depends on the energy resolution, determined by the beam energy spread (σ_E/E); by the spectrometer momentum resolution, and by the capability of reducing background with PID. Data were taken for both ^{12}C and ^{9}Be$(e, e'K^+)$ reactions. The analysis is still in a preliminary stage. Figure 43 shows the missing-mass spectrum with and without the RICH. The crucial role of the detector in cleaning the background is evident. Figure 44 shows the preliminary physics analysis of the missing energy spectra of the ^{12}C$(e, e'K^+)^{12}$B$_\Lambda$ (left plot) and ^{9}Be$(e, e'K^+)^{9}$Li$_\Lambda$ reactions (right plot).

The first large peak, in the left plot, and another peak at ~10 MeV are clearly visible, corresponding to the substitution of a p shell proton with a Λ in a s state

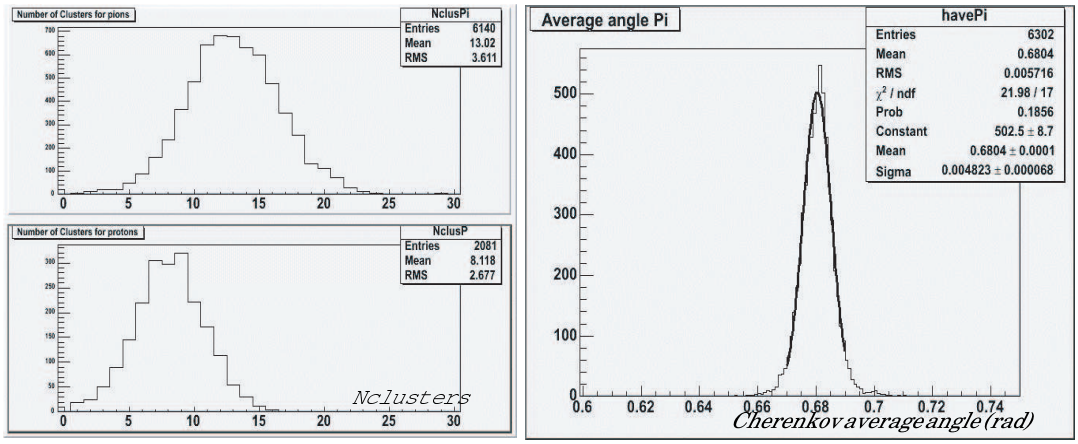

Figure 42: RICH performance. On the left side the number of photoelectrons for pions and protons is shown. On the right side the distribution of the Čerenkov angle reconstruction is reported, showing a resolution of 5 mrad.

and p state, respectively. In between two levels at ∼2.4 MeV and ∼6 MeV are also evident. The background is evaluated by fitting the 'not-physical' region (negative region of the missing-energy spectrum). The resulting values of the signal-to-noise ratio (SNR) for the two identified core-excited-state peaks are 7.5 at 2.6 MeV and 6.5 at 5.4 MeV.

Two theoretical curves have been superimposed on both spectra, differing in the model used for the elementary $K^+ - \Lambda$ production on protons. The hypernuclear wave function is the same for the two curves as computed by M. Sotona. The solid line uses the model of Bennhold-Mart(K-MAID) [38], the dashed line the one by Saghai Saclay-Lyon (SLA) [37]. Both curves have been normalized to the first (ground state) experimental peak. In the $^{12}\mathrm{C}(e, e'K^+)^{12}\mathrm{B}_\Lambda$ reaction, the relative intensities (with respect to the ground state) of the first excited peak at 2.6 MeV and of the strongly populated $p - \Lambda$ state at 11 MeV seem to be better reproduced by the MAID model than the SLA one. Another peak at $6 - 7$ MeV is underestimated by both models.

Of course, for any conclusion one has to wait for the final results of the analysis.

In the reaction $^9\mathrm{Be}(e, e'K^+)^9\mathrm{Li}_\Lambda$ the relative strength of the doublets is different from theoretical prediction. At the present stage of the analysis it is not possible to select the "best" model. In fact the analysis and the interpretation of the measured missing-mass spectra is still at a preliminary stage and not ready for final conclusions. Improvements in the energy resolution as well as statistics are crucial.

A first evaluation of the cross section has been extracted from the carbon

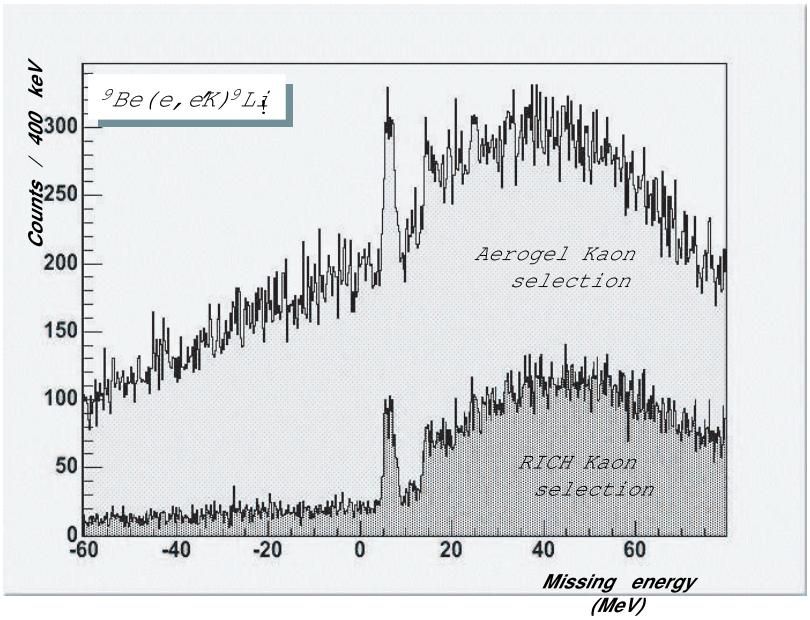

Figure 43: ^{9}Li$_\Lambda$ missing-energy spectrum with and without the RICH selection.

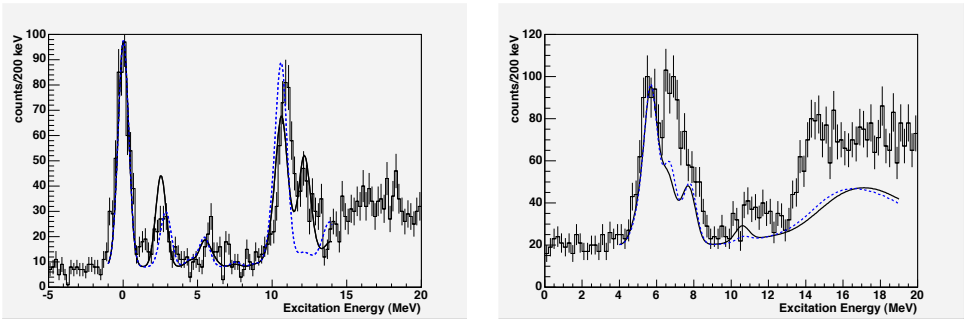

Figure 44: Left: ^{12}B$_\Lambda$ missing-energy spectrum, the solid and dashed lines represent the theoretical data (see text). Right: ^{9}Be$_\Lambda$ missing-energy spectrum, the solid and dashed lines represent the theoretical data (see text).

data. Considering the ground state of the $^{12}\mathrm{C}(e, e'K^+)^{12}\mathrm{B}_\Lambda$, the cross section is $\sigma_{g.s.}(^{12}\mathrm{B}_\Lambda) = 5.0 \pm 0.2\ (stat) \pm 1.0\ (syst)$ nb/(msr^2 GeV), to be compared with a prediction of [7],$\sigma_{g.s.} \sim 5.4$ nb/(msr^2 GeV).

Conclusion The first 'systematic' study of $1p$ shell hypernuclei with an electromagnetic probe has begun. Experiment E94-107 in Hall A at Jefferson Lab, designed to perform hypernuclear spectroscopy of light hypernuclei, took data on ^{12}C and ^{9}Be targets. The new experimental devices (septum magnets and RICH detector) have proven to be very effective. The RICH detector provided excellent kaon identification and a clean kaon signal over large pion and proton backgrounds. The analysis is still at a preliminary stage. Further work is needed to attain a missing energy resolution of the order of ∼500 keV. The optimization of event selection for the beam-energy stability, as well as the acceptance cuts, requires further work. The RICH analysis can be further improved. The esperiment is schedueled to take more data, primarily on ^{16}O in June 2005. During that run, if possible, some time may be dedicated to improving the statistics on ^{9}Be and/or ^{12}C.

3.4 E97-110

The GDH Sum Rule, the Spin Structure of ^{3}He and the Neutron using Nearly Real Photons

J.-P. Chen, A. Deur, F. Garibaldi, spokespersons
and
the E97-110 Collaboration.

The goal of the experiment is to measure the generalized Gerasimov-Drell-Hearn integral (GDH) at low Q^2 on the neutron and ^{3}He. It provides a check of chiral perturbation theory at low Q^2 and of the original ($Q^2 = 0$) GDH sum rule. A brief description of the physics goals and the experimental running was given in the previous Hall A report.

The experiment The experiment ran in April-May and July-August 2003. Part of the low Q^2 data were acquired in the first run period (April-May 2003). There were experimental complications due to a set of mis-wired coils in the septum magnet. The septum was repaired in June. Most data were taken in the second run period with the septum magnet problem corrected.

Present state and outlook The analysis is under way focusing on the data from the second run period first. The only effort for the first run period data is the optics study, which is on-going at the University of Virginia (H. Zaidi, N. Liyanage, UVa). For the second run period, the optics analysis for both 6 deg and 9 deg is completed and checked (V. Sulkosky, William and Mary). One example of the optimized sieve-slit data is shown in Fig. 45. This completes one of the major tasks of the analysis. The next task is an acceptance study and modeling of the spectrometer-septum combination. Particle Identification analysis is nearly done (J. Yuan, Rutgers U. and independently checked by H. Lu, USTC). The VDC analysis is just starting (S. Dhamija, U. of Kentucky). Given the large rates seen in the experiment, procedures will have to be developed to deal with the large number of multi-track events. Modeling of the collimator punch-through is complete (A. Deur, JLab and S. Dhamija) and was found acceptable for the second run. A more sophisticated simulation is needed for the first run period. Studies of the BCM linearities and Hall C current bleed-through have been done (T. Holmstrom, William and Mary) and beam charge normalization does not appear to be a problem for the experiment in spite of the low beam current used and the bleed-through. Beam charge asymmetries were also found to be under control.

Our near-term plan includes spectrometer acceptance studies (V. Sulkosky), target analysis (NMR and EPR polarimetries and density (V. Sulkosky and P. Solvignon, Temple U.), finalizing the first run optics (H. Zaidi, N. Liyanage), the PID analysis (J. Yuan and H. Lu) and the VDC study (S. Dhamija). An analysis of the scalers and scintillators will also be carried out (J. Yuan).

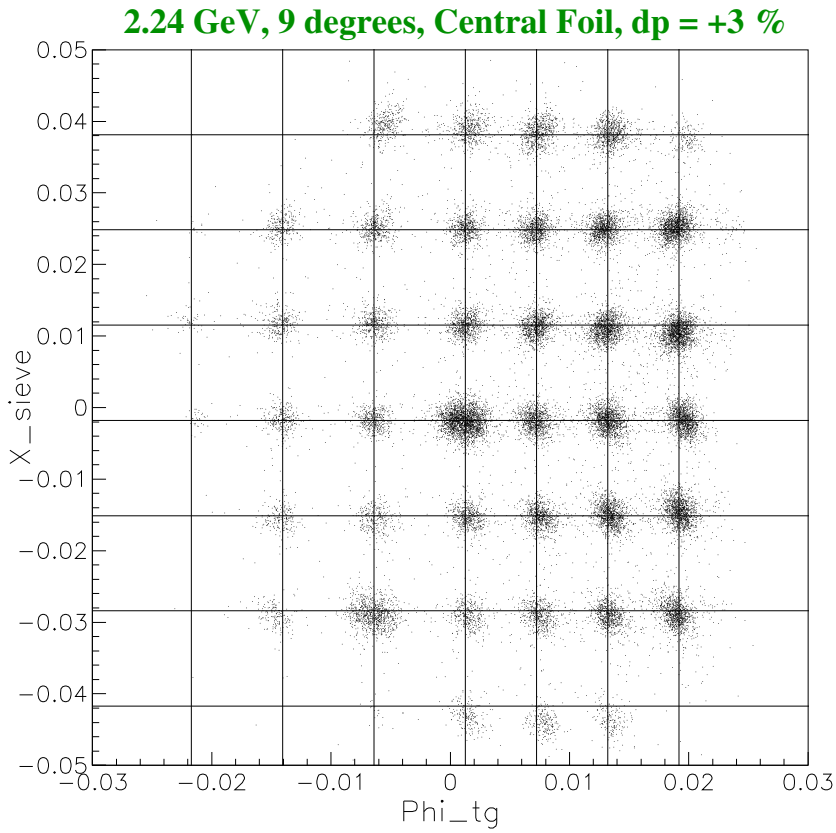

Figure 45: Sieve-slit data of x_{sieve} vs ϕ_{tg} for the central foil at 2.24 GeV and 9° with $dp/p = 3\%$. The line crossings are the expected positions of the sieve holes.

The longer term plan includes a final elastic analysis and refined background studies (J. Singh, UVa), independent analysis of the target (J. Singh), extraction of the cross sections and asymmetries (V, Sulkosky, J. Singh, J. Yuan) and analysis of the first run period (the USTC group).

3.5 E97-111

Systematic Probe of Short-Range Correlations via the Reaction ^{4}He$(e, e'p)$

J. Mitchell, B. Reitz, and J. Templon, Spokespersons,
and
the Hall A Collaboration.

Experiment E97-111 took data in September and October 2000, measuring unseparated cross sections for the (*e,e'p*) reaction on ^{4}He at recoil momenta up to 530 MeV/c. In the plane-wave impulse approximation, many calculations predict a sharp minimum in the cross section for recoil momenta around 450 MeV/c and show that its location is sensitive to the short-range part of the internucleon potential. However, reaction dynamic effects such as final-state interactions (FSI) and meson-exchange currents (MEC) can obscure such a minimum. Many ideas have been formulated about how to suppress contamination from these reaction dynamic processes or how to disentangle these effects. This experiment incorporated several ideas by utilizing parallel kinematics, measuring at high momentum transfers, and taking the data at several different kinematic points.

This experiment used the standard equipment available in Hall A. The main emphasis was on measuring the ^{4}He(*e,e'p*)^{3}H cross section at recoil momenta up to 530 MeV/c in parallel kinematics at two different beam energies 2.389 GeV and 3.170 GeV. Additional data were taken in two quasi-perpendicular kinematics, with ω fixed to 525 and 487 MeV and Q^2 values of 1.78 and 1.82 GeV^2. The exclusiveness of the two-body breakup channel is guaranteed by means of cuts on the missing energy E_m. The ^{4}He(*e,e'p*)^{3}H reaction will only occur at E_m = 19.81 MeV. The continuum is well separated, with a threshold for the three-body breakup of 26.1 MeV and 28.3 MeV for the four-body breakup.

Preliminary results for the reduced cross sections in the PY2 kinematics are shown in Fig. 46. The error bars show the statistical error only. The cross section is divided by the elementary e-p off-shell cross section σ_{CC1} and the recoil factor η, to remove the basic kinematical dependence on the polarization of the virtual photon. The reduced cross section falls monotonically within this momenta range. The experimental data are compared with a set of theoretical predictions from J.M. Laget. The PWIA calculation is plotted as a dashed curve, the calculation including FSI is dotted, and the full calculation (including FSI, MEC and IC contributions) is represented by the solid line. For the FSI at lower energies phase-shift description was used, which describes elastic NN scattering. At higher energies a high-energy parametrization of the NN scattering amplitude was used, its imaginary part representing the absorptive part of the NN interaction.

The full calculations do not preserve the minimum in the spectral function at this kinematical setting. Laget's calculations indicate, that this is mainly due to FSI, whereas the inclusion of MEC and IC has only a small effect on the predicted cross section. These calculations also show that below 280 MeV/c the PWIA cross

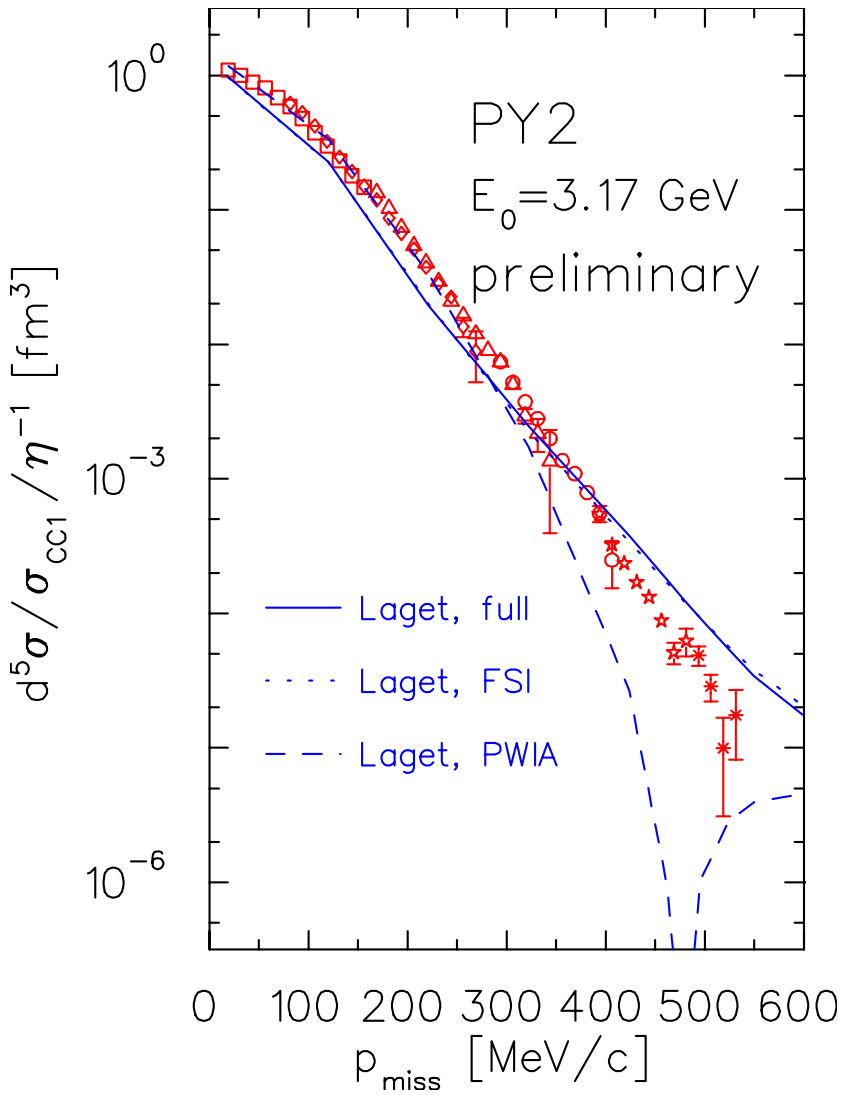

Figure 46: Preliminary results for the reduced cross sections at a beam energy of 3170 MeV. The error bars only show the statistical uncertainty. The dashed line shows the theoretical prediction by Laget in PWIA, the dotted line includes FSI, and the solid line depicts the full calculation.

section is larger than the one of the full calculation, above that value the PWIA cross section is smaller. This indicates that the FSI tends to shift cross section from low p_m (where the spectral function is high) to the dip region (where the PWIA cross section is tiny).

All production data of E97-111 have been replayed, as well as the runs for optics calibration, for the calibration of angular offsets, for target boiling studies, and for the ^{3}He(e, e) elastic reaction. To finalize the results further studies of detector efficiencies are ongoing. The elastic data need further analysis to obtain the absolute normalization. Finally, a careful study of acceptance cuts and other systematic uncertainties are planned.

3.6 E99-114

Real Compton Scattering from the Proton at High Momentum Transfer

Charles Hyde-Wright, A. Nathan, and B. Wojtsekhowski, Spokespersons,
and
the Hall A Collaboration.

Real Compton Scattering (RCS) is an unique tool to study the structure of the nucleon. In the kinematics region where Mandelstam variables s, $-t$, and $-u$ are large compared to the proton mass, RCS has been analyzed within two different theoretical approaches, which are distinguished by the number of quarks participating in the reaction. In the perturbative QCD (pQCD) approach, which is characterized by three active quarks, the transferred momentum is redistributed through the exchange of two hard gluons [42, 43, 44, 45, 46]. The handbag mechanism [47] assumes that there is only a single active quark that couples to the external photons and shares the transferred momentum through the overlap of the soft wave functions. Factorization of hard and soft subprocesses is the main assumption which stands behind the handbag diagram.

Calculations based on the handbag mechanism lead to a very interesting feature, that is factorization of the RCS cross section into a product of the Klein-Nishina (KN) cross section for massless spin 1/2 particle, and a form factor-like object [48]:

$$\left.\frac{d\sigma}{dt}\right|_{\rm RCS} = \left.\frac{d\sigma}{dt}\right|_{\rm KN} [f_V R_V^2 + (1-f_V) R_A^2] \ , \tag{4}$$

where $f_V = \frac{1}{2}(\hat{s}-\hat{u})^2/(\hat{s}^2+\hat{u}^2)$ is a kinematic factor, and $\hat{s} = s - m_p^2$, $\hat{u} = u - m_p^2$. The contribution of the the third RCS form factor R_T is not included in the present analysis, because its magnitude is small compared to those due to R_V, R_A. The RCS form factors R_V, R_A are related to the $1/x$ moments of GPDs in the following way:

$$\begin{aligned} R_V(t) &= \sum_a e_a^2 \int_{-1}^{+1} \frac{dx}{x} \, H^a(x;0,t) \ , \\ R_A(t) &= \sum_a e_a^2 \int_{-1}^{+1} \mathrm{sign}(x) \frac{dx}{x} \, \widetilde{H}^a(x;0,t) \ , \end{aligned} \tag{5}$$

where a denotes quark flavors.

The polarization transfer coefficient is expressed by these form factors according to the following formula:

$$K_{LL} \simeq \frac{R_A}{R_V} K_{LL}^{KN} \left[1 - \frac{t^2}{2(s^2+u^2)} \left(1 - \frac{R_A^2}{R_V^2} \right) \right]^{-1} \tag{6}$$

The goal of this experiment was to distinguish among the aforementioned reaction mechanisms by measuring the RCS cross section and the polarization transfer coefficient.

We present the polarization transfer coefficient K_{LL} in Fig. 47 [51].

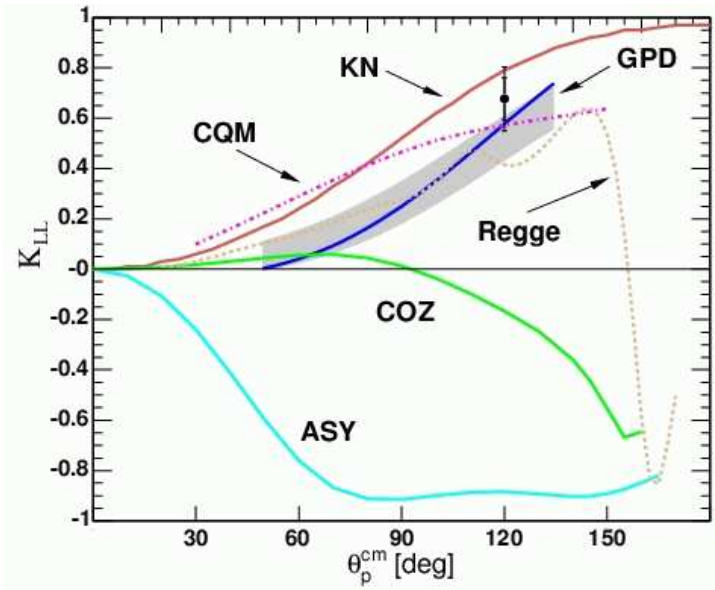

Figure 47: Our result for K_{LL} compared with calculations in different approaches: ASY and COZ both from pQCD [46], GPD [52], extended Regge model [53], and CQM [54]. The curve labeled KN is K_{LL}^{KN}, the Klein-Nishina asymmetry for a structureless proton.

The excellent agreement between the experiment and the handbag-based calculations are consistent with a picture in which the photon scatters from a single quark whose spin is in the direction of the proton spin.

The results for the form factor R_V are shown in Fig. 48 [49]. In this plot, we observe s-independence of the extracted form factors at $s = 8.9$, 11.0 GeV^2, except for the backward angle measurements, where the Mandelstam u variable decreases, especially for $s = 8.9$ GeV^2.

Both the polarization measurement and the cross-section scaling suggest that the handbag mechanism dominates the reaction mechanism. Additional measurements of K_{LL} are approved for experiment E03-003. With the 12 GeV upgrade, we anticipate measurements of equal statistics up to $s = 20$ GeV^2 and $t = 15$ GeV^2.

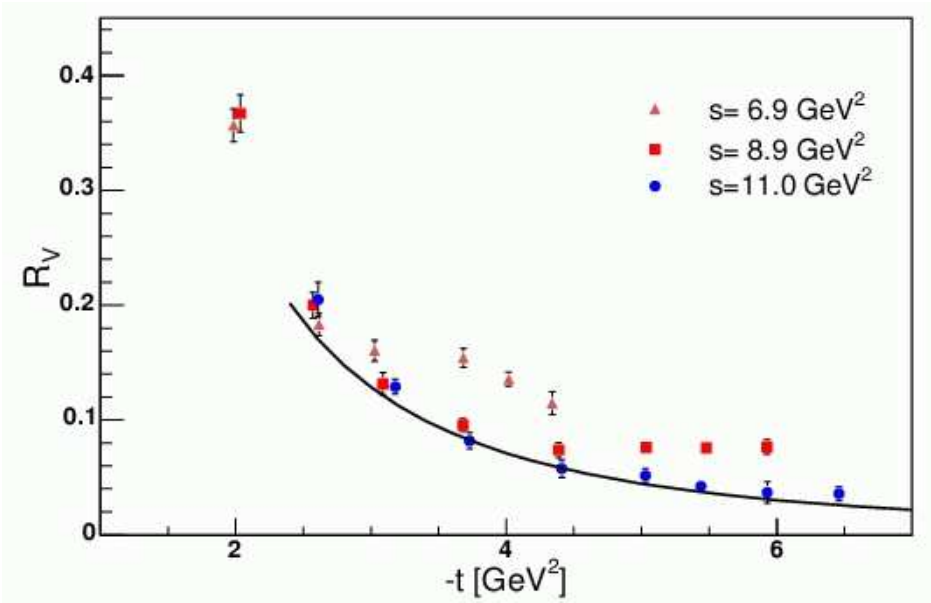

Figure 48: Extracted RCS form factor R_V, the solid line is a calculation [50].

3.7 E99-115 and E00-114

A Study of the Strange Content of the Nucleon via Parity-Violating Asymmetries in the $\vec{e}\,p \to e\,p$ and $\vec{e}\,{}^4\mathrm{H} \to e\,{}^4\mathrm{He}$ reactions.

D. Armstrong, G. Cates, K. Kumar, D. Lhuillier and R. Michaels, spokespersons, and the Hall A Collaboration.

The second-generation HAPPEx experiments measure the parity-violating asymmetry in elastic scattering of polarized electrons from ^{1}H and ^{4}He. This asymmetry is proportional to the Z^0 exchange which is used as a new probe of the nucleon structure. By analogy to the electromagnetic form factors $G_E^{\gamma p}$ and $G_M^{\gamma p}$ the nucleon weak vertex is parametrized by the weak form factors G_E^{Zp} and G_M^{Zp}. Assuming charge symmetry between the proton and neutron one can combine these two sets of form factors with the electromagnetic form factors of the neutron and extract the contribution of the three lightest quark flavors to the vector matrix element of the nucleon. Since the contribution of the strange quarks (G_E^s and G_M^s) comes only from the $s\bar{s}$ fluctuations of the quark sea a clean measurement of these observables provides new insight into the role of the fundamental degrees of freedom of QCD and their dynamics in the non-perturbative structure of the nucleon.

At tree level the parity violating asymmetry from protons is given by

$$\begin{aligned} A^{\mathrm{PV}} &= -\frac{G_F|Q|^2}{4\pi\alpha\sqrt{2}} \times \Bigg[(1-4\sin^2\theta_W) \\ &\quad - \frac{\epsilon G_E^{\gamma p}(G_E^{\gamma n}+G_E^s) + \tau G_M^{\gamma p}(G_M^{\gamma n}+G_M^s) - (1-4\sin^2\theta_W)\epsilon' G_M^{\gamma p} G_A^e}{\epsilon (G_E^{\gamma p})^2 + \tau (G_M^{\gamma p})^2}\Bigg] \end{aligned} \tag{7}$$

where G_A^e is the axial form factor of the nucleon coming from the vector-axial structure of the weak neutral current. This term contributes significantly to A^{PV} only at backward scattering angle (θ) due to the kinematic factors ϵ, τ and ϵ', functions of θ and the beam energy (E). The HAPPEx measurements take place at very forward angles where the main contributions are electric and magnetic. A first experiment occurred in 1998-99 and measured [55] the combination $G_E^s + 0.392\, G_M^s = 0.014 \pm 0.020 \pm 0.010$, compatible with zero at $Q^2 = 0.47\,\mathrm{GeV}^2$. This result has demonstrated the high "parity quality" of the CEBAF beam and prompted a second generation of HAPPEx experiments. The strategy is to seek a possibly larger contribution at a lower Q^2 (0.1 GeV^2) and to separate the electric and magnetic contributions by making measurements on the proton and an isoscalar target, only sensitive to G_E^s. The ^{4}He nucleus is chosen for its small and well-controlled effect of the nuclear structure. The tree level asymmetry is given by

$$A^{\mathrm{PV}} = \frac{G_F|Q|^2}{4\pi\alpha\sqrt{2}}\left(4\sin^2\theta_W + \frac{2G_E^s}{G_E^{\gamma p}+G_E^{\gamma n}}\right) \tag{8}$$

A first run was conducted in summer 2004, collecting approximately 10% of the final anticipated statistics for each target. The figure of merit grows toward high E and small θ leading to optimal kinematics $E = 3$ GeV and $\theta = 6°$. The final expected asymmetries and constraints on the strange form factors are listed in Table 6. The control of the systematic error at the 40 ppb level for hydrogen as well as the normalization at the 2% level for helium are the main challenges taken

	A^{PV}	δA_{stat}	δA_{syst}	Sensitivity
H	-1.60	0.08 (5%)	0.04 (2.5%)	$\delta(G_E^s + 0.08\ G_M^s) = 0.010$
^{4}He	+7.8	0.18 (2.2%)	0.18 (2.2%)	$\delta G_E^s = 0.015$

Table 6: Expected asymmetries and errors for H and ^{4}He targets. When not specified all asymmetries are quoted in ppm units.

up by these experiments. They require a specialized instrumentation in Hall A and an improved control of the noise and asymmetries in the beam parameters.

Figure 49 illustrates the experimental setup. The polarized electron beam is directed onto a 20 cm long cryogenic target and electrons scattered at 6° are detected in the Hall A High Resolution Spectrometers (HRS) configured symmetrically to double the rate. Because the HRS are physically unable to approach closer than 12.5°, an additional superconducting dipole (septum magnet) is installed in front each spectrometer. The expected high statistical precision on tiny physics asymmetries requires to run at very high luminosity leading to huge elastic rates in each spectrometer, up to 65 MHz for hydrogen. The experiments take advantage of the HRS magnetic optics which focuses the elastic events in the focal plane along a line 50 cm away from the pion threshold events, the first inelastic background. The detector is a dedicated total absorption Cerenkov calorimeter, composed of alternating layers of quartz and brass, positioned above the elastic line. A custom-made ADC integrates the light flux, proportional to the total energy deposited, over each helicity gate (33 ms). The standard detection package of the HRS can not operate at high rate in production mode. It is used only during dedicated runs at very low current ($\approx$1 μA) for detailed background studies and measurement of the mean Q^2 intercepted by the detector. In production mode a cross-check and monitoring of the rate distribution across the focal plane is performed by a scanner sweeping the acceptance.

The combination of an intense beam and an extended target can induce density fluctuations inside the target cell which would add to the pure statistical width of the counting rate and potentially affect the accuracy of the measurement. To keep this effect small data were taken with "race track" type target cells. With this new geometry the coolant flow is transverse to the beam axis dissipating the heat load in a more efficient way. To monitor the target fluctuations, eight dedicated luminosity detectors are installed around the beam axis at very forward angle (0.5°), where the statistical width is a lot smaller than in the detectors. It was

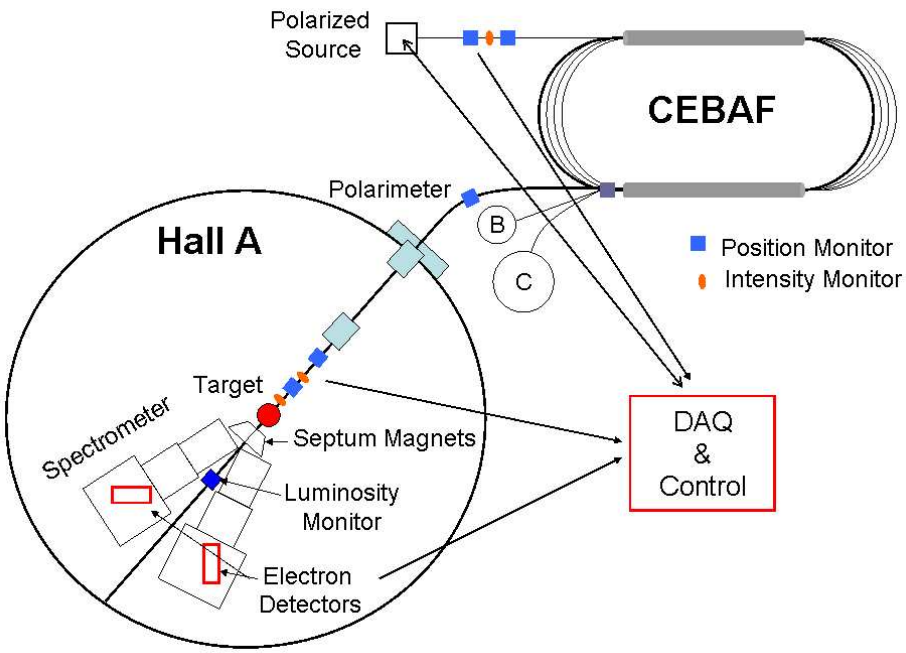

Figure 49: Overview of the HAPPEx-II experiment.

shown these fluctuations can be kept negligible at the high current provided that the raster size is large enough (5x5 mm).

One major challenge for achieving high absolute precision is the control of helicity-correlated changes in the beam parameters which arise primarily from laser optics in the electron source. A feedback loop connecting the beam current readout in Hall A and the laser intensity modulation at the source was used to reduce the charge asymmetry of the electron beam. The HAPPEx collaboration, working closely with the CEBAF Electron Gun Group has dedicated significant resources to identifying sources of position differences and reducing them by a careful setup of polarization and transport system for the laser beam. The positions at the target strongly depend on the beam optics and are more difficult to control via a feedback loop than the intensity. Besides the careful setup at the source the HAPPEx experiments thus rely on the "damping" of the position differences inherent in the acceleration of the electron beam as well as on the control of the beam optics near the target. Position differences of a few nanometers averaged over the run were achieved, meeting the requirements of the experiment.

The beam polarization is continuously monitored by the Hall A Compton polarimeter with few cross-check points from the Møller polarimeter in Hall A and the Mott polarimeter in the injector. For the helium run an impressive mean polarization above 85% was achieved with the first use of the new "supperlattice"

photocathode technology at CEBAF.
The preliminary analysis of the summer 2004 data leads to

$$A_{He}^{PV}(Q^2 = 0.95\,\mathrm{GeV}^2) = +7.40 \pm 0.89_{(stat)} \pm 0.57_{(syst)} \tag{9}$$
$$G_E^s(Q^2 = 0.95\,\mathrm{GeV}^2) = -0.019 \pm 0.041_{(stat)} \pm 0.026_{(syst)}$$

for the helium target and

$$A_H^{PV}(Q^2 = 0.99\,\mathrm{GeV}^2) = -1.10 \pm 0.27_{(stat)} \pm 0.10_{(syst)} \tag{10}$$
$$G_E^s + 0.08G_M^s(Q^2 = 0.99\,\mathrm{GeV}^2) = 0.034 \pm 0.028_{(stat)} \pm 0.010_{(syst)} \pm 0.009_{(FF)}$$

for the hydrogen target. The third uncertainty quoted for $G_E^s + 0.08G_M^s$ accounts for uncertainty in the electromagnetic form factors (mainly $G_E^{\gamma n}$). Data analysis is still proceeding to further reduce the main sources of systematic errors before publication in spring 2005.
The two above combinations of strange form factors draw two bands in the $G_M^s - G_E^s$ plane, illustrated in Fig. 50. Also shown are the results from the PVA4 experiment at MAMI [56] and SAMPLE experiment at MIT-Bates [57] which measure complementary combinations at the same Q^2. Taken together, these

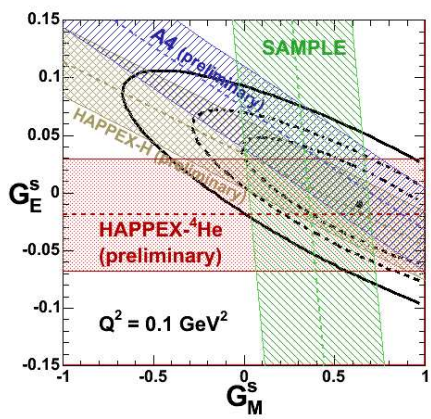

Figure 50: Preliminary HAPPEx-H and HAPPEx-He results from the 2004 run, with results from PVA4 [56] and SAMPLE [57]. The three ellipses correspond to contours at the 68%, 90% and 99% confidence level.

measurements suggest a positive G_M^s although the deviation is not yet statistically conclusive. The final accuracy expected from the concluding run of HAPPEx in late summer 2005 should either establish a deviation from zero or constrain the strange content of the nucleon at low Q^2 to a negligible level.

3.8 E00-007

Proton Polarization Angular Distribution in Deuteron Photo-Disintegration

R. Gilman, R. Holt, X. Jiang, Z.-E. Meziani, and K. Wijesooriya, Spokespersons,
and
the Hall A Collaboration.

The experiment completed data taking in September-October 2002. The data taking consisted of calibrations of the focal plane polarimeter (FPP) analyzing power, at momenta of 2.4, 2.2, 2.0, and 1.7 GeV/c. These measurements used coincident *ep* scattering at 4.056 GeV beam energy. To improve the polarimeter performance, the left arm was configured with two analyzers to improve the efficiency of detecting scattered particles, just as in the Real Compton Scattering experiment. In this configuration, the front straw chambers determine both whether particles have scattered from the front analyzer, and the trajectory into the rear analyzer. By splitting the analyzer into two shorter halves, the inefficiencies that result from absorption of protons in a single thick analyzer are reduced.

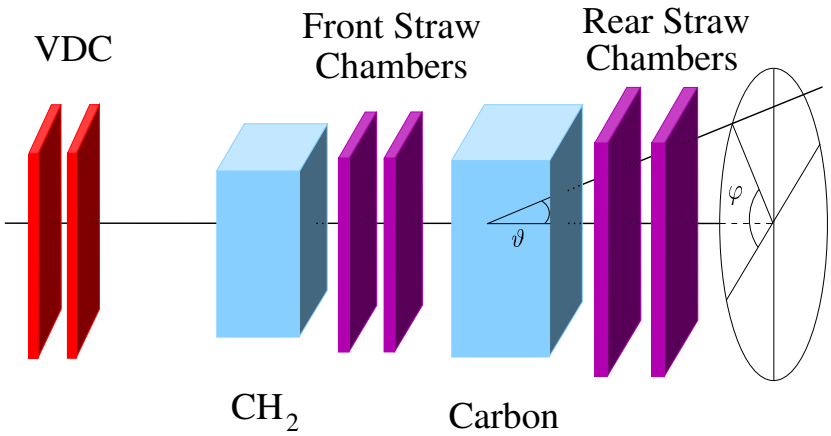

Figure 51: The FPP configuration in E00-007.

The FPP analyzer and chamber configuration in E00-007 are shown in Fig. 51. The software alignment of FPP chambers was done using the straight-through data. There are two steps in the alignment: first the front two FPP chambers were aligned to the VDC, second the rear two FPP chambers were aligned against the front chambers. At each step, software corrections were introduced as functions of the FPP track projection in the x and y direction.

This experiment was the first one to run in Hall A after the beam helicity reporting scheme changed to the G^0 delayed reporting mode. The G^0 scheme of helicity signal from the injector does not report the helicity of the current beam pulse. Instead, it reports the helicity of beam pulse which arrived eight-pulses

earlier. To correctly reconstruct the helicity of the current beam pulse, one needs to rely on a proper beam pulse counting in order to trace back in time.

To help identify the start of each beam pulse, an event-9 trigger was inserted into the data stream at the rate of 30 Hz (every 3515 clock-tics counted by the 105 kHz DAQ-clock). Ideally, if no event-9 triggers ever get lost in the data stream, the reconstruction of current pulse helicity is straight forward. However, occasionally due to a DAQ-busy or some other unknown source of instability, an event-9 time marker was lost in the data stream and one has to rely on other ways to reconstruct the beam pulse structure. In the analysis code, the time stamp of each event and the timing patterns of earlier beam pulses are used to help identify the beam pulse structure when an event-9 trigger failed to show up at the expected time.

Although the G^0 helicity scheme sounds very simple to start with, however, due to the fact that none of the intended time markers in the data stream were 100 percent reliable for E00-007 data taking period, the proper reconstruction of the helicity flag turned out to be the major challenge of the data analysis work.

The clear signature of a focal plane ϕ_{FPP} asymmetry in an *ep* calibration run demonstrated that the beam helicity was correctly decoded. The polarization transfers in *ep* elastic runs are listed in Table 7. The ratio of $\mu_p G_E^p/G_M^p$ from these calibration runs are listed in Table 8.

	P_t			P_l		
Q^2	e.-val.	CH_2	Carbon	e.-val.	CH_2	Carbon
1.85	0.148	0.155 ± 0.015	0.136 ± 0.015	0.394	0.388 ± 0.013	0.403 ± 0.011
2.38	0.148	0.170 ± 0.028	0.155 ± 0.036	0.497	0.483 ± 0.021	0.493 ± 0.023
2.78	0.143	0.154 ± 0.042	0.116 ± 0.041	0.572	0.567 ± 0.022	0.583 ± 0.015
3.10	0.137	0.124 ± 0.035	0.159 ± 0.041	0.629	0.634 ± 0.012	0.620 ± 0.019

Table 7: Polarization transfer components in the reaction plane P_t and P_l. The expected values (e.-val.) at bin-center are calculated based on a fit to the Hall A G_E^p-II data, the extracted values from both the CH_2 analyzer and the Carbon analyzer are listed.

			CH_2		Carbon	
Q^2	P_p	G_E^p-II	$\mu_p G_E^p/G_M^p$	$\langle A_c \rangle$	$\mu_p G_E^p/G_M^p$	$\langle A_c \rangle$
1.85	1.68	0.782	0.833 ± 0.110	0.115 ± 0.009	0.700 ± 0.097	0.129 ± 0.011
2.38	2.00	0.708	0.845 ± 0.176	0.123 ± 0.015	0.745 ± 0.200	0.112 ± 0.017
2.78	2.23	0.652	0.717 ± 0.221	0.089 ± 0.011	0.523 ± 0.200	0.100 ± 0.012
3.10	2.41	0.607	0.553 ± 0.166	0.091 ± 0.007	0.724 ± 0.207	0.084 ± 0.008

Table 8: The extracted form factor ratio $\mu_p G_E^p/G_M^p$ and the averaged analyzing power $\langle A_c \rangle$ are listed for both the CH_2 analyzer and the Carbon analyzer, the expected values of $\mu_p G_E^p/G_M^p$ from a fit to the Hall A G_E^p-II data are also listed .

Recoil polarization data were obtained at five center-of-mass angles, 37°, 53°, 70°, 90°, and 110°. Data for 110° were low enough in momentum to be taken with only the standard carbon FPP analyzer, obviating an *ep* calibration for this point. Estimated absolute statistical uncertainties on the polarization observables p_y, C_x, and C_z are in the range 0.05 - 0.10. The γd data analysis is expected to be completed in the next six to ten months, a final publication is expected to be submitted within a year.

3.9 E00-102

Testing the Limits of the Single Particle Model in ^{16}O $(e, e'p)$

A. Saha, W. Bertozzi, L. B. Weinstein, and K. Fissum, spokespersons

Experiment E00-102 is an update to Hall A experiment E89-003: measurement of the cross section, R_{LT}, and A_{LT} for the ^{16}O $(e, e'p)$ reaction. Experiment E89-003 made measurements at energy and momentum transfer of $\varpi = 0.445$ GeV and $Q^2 = 0.8$ GeV^2, respectively, up to $p_m = 0.345$ GeV/c [68, 69, 70]. This update experiment expands these measurements up to $p_m = 0.755$ GeV/c at $\varpi = 0.449$ GeV and $Q^2 = 0.902$ GeV^2. The goals of these measurements are to determine:

- the limits of validity of the single-particle model of valence proton knockout;
- the effects of relativity and spinor distortion on valence proton knockout using the diffractive character of the A_{LT} asymmetry; and
- the bound-state wave function and spectroscopic factors for valence knockout.

The cross section will be determined for measurements from $p_m = -0.515$ GeV/c to $p_m = 0.755$ GeV/c, in order to determine the point at which single-knockout calculations fail and two-nucleon effects become important. R_{LT} and A_{LT} will be separated for p_m up to ± 0.515 GeV/c to further test the relativistic DWIA calculations. Figure 52 shows anticipated data points from E00-102 for A_{LT} as a function of missing momentum for the $1p$-shell states along with data obtained from E89-003, both compared to calculations from Udias *et al.*

Data were taken at a fixed beam energy of 4.620 GeV/c, $\overrightarrow{q} = 1.066$ GeV/c, and $\theta_q = 56.22°$. Throughout the entire experiment, the electron arm (HRS-L) was also fixed at 12.5° with a central momentum of 4.121 GeV/c, allowing it to be used as a luminosity monitor. The hadron arm (HRS-R) angle varied from 28.3° to 96.1° to cover the necessary missing momentum range. These kinematics are shown in Fig. 53.

Both detector stacks were used in their standard configurations. Each stack, however, contained an additional S0 scintillator for checking trigger efficiency; and the HRS-L contained a pion rejector to be used for addition particle identification of π^-'s. The target used was the Hall A self-normalizing three-foil waterfall target [71, 72]. Each water foil was approximately 200 mg/cm^2 thick and separated by 25.4 mm at an angle of 57.4° with respect to the beam direction. Using the hydrogen in the water, precision calibrations can be made as well as normalization of cross sections to known ^{1}H $(e, e'p)$ and ^{1}H (e, e') cross sections.

All calibrations and corrections have now been performed and the data has been replayed using ESPACE. Hydrogen cross sections will be calculated soon using parallel kinematics data. After that, oxygen cross sections, along with R_{LT} and A_{LT}, will be calculated.

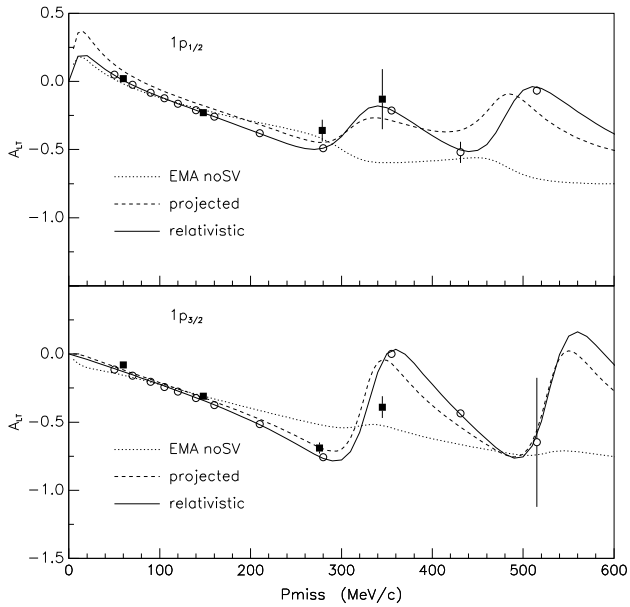

Figure 52: Projected A_{LT} data compared to E89-003 results and calculations of Udias *et al.* Open circles are anticipated data points from E00-102, solid squares are E89-003 data obtained at slightly different kinematics.

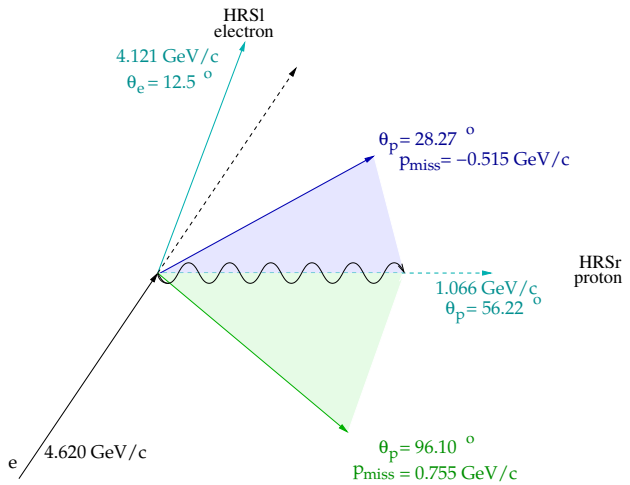

Figure 53: E00-102 kinematics. HRS-L remained fixed at 12.5° throughout the experiment while HRS-R varied around the direction of parallel kinematics.

3.10 E00-110 and E03-106

Deeply Virtual Compton Scattering from the Proton and the Neutron

Charles Hyde-Wright, Pierre-Yves Bertin, Franck Sabatie, Ron Ransome, Eric Voutier, spokespersons,
and
the Hall A Collaboration.

In deeply virtual Compton scattering on the nucleon we study the reaction $eN \to eN\gamma$ at high s, Q^2, and low t. A QCD factorization theorem predicts that the virtual Compton scattering amplitude factorizes into the convolution of a perturbative kernel and a set of ground-state matrix elements (generalized parton distributions, or GPDs) [73, 74, 75, 76]. The GPDs are functions of x, $\xi \approx x_{\rm Bj}/(2-x_{\rm Bj})$, and t. $x \pm \xi$ are the lightcone momentum fractions of the active quark in the initial and final states, with negative values denoting antiquarks. t (or more specifically the component of $q - q'$ perpendicular to $q + q'$) is the Fourier conjugate to the transverse coordinate of the quark relative to the center-of-momentum coordinate [79, 80, 81, 82].

In DVCS Experiments E00-110 [77] and E03-106 [78] we measured the $\mathrm{H}(e, e'\gamma p)$ and $\mathrm{D}(e, e'\gamma N)N$ reactions at Q^2 from 1.5 GeV^2 to 2.5 GeV^2 and $x_{\rm Bj} = 0.35$ and at Q^2=1.9 GeV^2 and $x_{\rm Bj} = 0.35$, respectively. Our goal is to measure the helicity-dependent cross section, which is dominated by the interference of the Bethe-Heitler amplitude (radiation from incident or scattered electron) with the DVCS amplitude constrained to the locus $x = \pm\xi$ [83, 84]:

$$\frac{d^5 \overrightarrow{\sigma}}{dQ^2 dx_B dt d\varphi} - \frac{d^5 \overleftarrow{\sigma}}{dQ^2 dx_B dt d\varphi} = \frac{\alpha^3}{2\pi^2} \frac{(2-y)}{-t} \sqrt{\frac{K^2}{1+e^2}} \left[\frac{A \sin\varphi + B \sin 2\varphi + C \sin 3\varphi}{s' u'} \right]. \tag{11}$$

The variable φ is the azimuth of the hadron plane ($\vec{q}' \otimes \vec{p}'$) with respect to the electron scattering plane. $s'u' = -4(k \cdot q')(k' \cdot q')$ originates from the electron propagators of the BH process. $y = q \cdot p / k \cdot p$ is the invariant inelasticity and in the Bjorken limit the kinematic factor $K^2/(1+e^2) \to (1 - x_{Bj})(t_{\rm min} - t)/\vec{q}^2$. The $A \sin\varphi$ term leading-twist contribution to the cross-section difference. It is the interference of the BH amplitude with three (out of four) quark GPDs:

$$A = F_1(-t)\mathcal{H}(\xi,t) + \xi G_M(-t)\tilde{\mathcal{H}}(\xi,t) + \frac{-t}{4M^2} F_2(-t)\mathcal{E}(\xi,t), \tag{12}$$

$$\mathcal{H}(\xi,t) = \pi \sum_q e_q^2 \left[H_q(x=\xi,\xi,t) - H_q(x=-\xi,\xi,t) \right] \tag{13}$$

where F_1, G_M, and F_2 are the usual elastic form factors, and the definitions of $\tilde{\mathcal{H}}$ and $\tilde{\mathcal{E}}$ are analogous to Eq. 13. While the proton experiment at our kinematics is mostly sensitive to $\mathcal{H}(\xi,t)$, the neutron experiment allows to access the least

known GPD $\mathcal{E}(\xi, t)$, both of them being essential for the determination of the total angular momentum carried by the quarks.

In our experiment, the electron is detected in the HRS-L, the photon is detected in a 132 element PbF_2 calorimeter, and the proton is detected in a 100 element plastic scintillator array. In the deuterium case, an additional detector made out of 57 scintillator strips in two layers in front of the proton array tags charged particles to separate neutrons from protons. Each channel of the photon, proton and tagger arrays is recorded by a 128 sample 1 GHz analog ring sampler (ARS) which is stopped (and subsequently digitized) following a trigger signal from the electron spectrometer. To reduce the random data-acquisition rate, we have a parallel-logic digital trigger which either validates the photon signal in the calorimeter and initiates the digitization and readout cycle, or provides a fast clear signal, allowing the acquisition to resume within 1 μs of each electron trigger. Following the spectrometer trigger, the digital trigger integrates each calorimeter PMT signal in a 40-60 ns window, and then searches all contiguous 4 block clusters for a shower signal above threshold (typically 1 GeV).

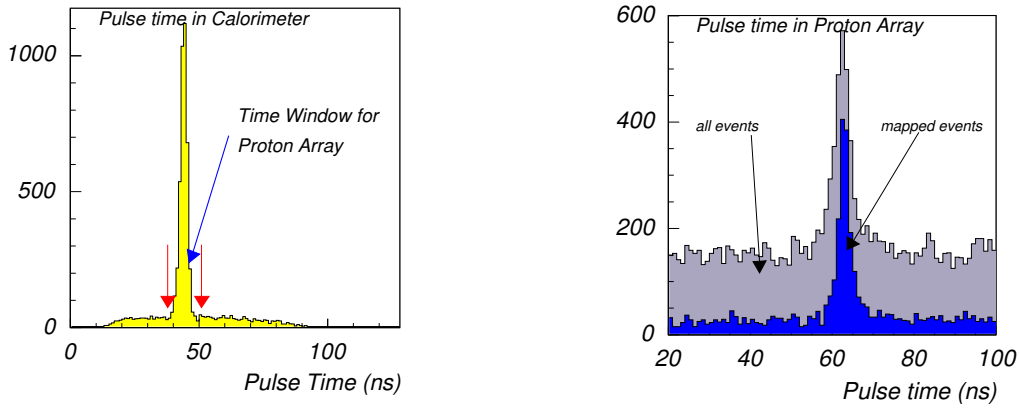

Figure 54: Left: $H(e, e'\gamma)X$ coincidence time spectrum for events with a 1 GeV cut in the calorimeter. Right: Electron-proton coincidence time spectrum for events with a true coincidence time cut on the $H(e, e'\gamma)X$ spectrum. The blue histogram labeled "Mapped Events" is obtained selecting only those blocks in the proton array that lie within a loose footprint of $H(e, e'\gamma p)$ events, as defined by the position of the photon shower in the calorimeter.

Figure 54 shows the coincidence time spectrum between the electron and photon, for shower signals above 1 GeV in the calorimeter. The right-hand panel shows the coincidence time spectra between the electron and the proton array, for $H(e, e'\gamma)X$ coincidence events within the true coincidence window of the left-hand panel.

In Fig. 55 we show preliminary missing-mass spectra for the $H(e, e\gamma)X$ re-

action. The complete histogram (blue) is for all $\mathrm{H}(e, e'\gamma)X$ events. The red histogram is for $\mathrm{H}(e, e'\gamma p)X$ events in which the triple coincidence kinematics satisfies a coplanarity cut for the detected proton direction relative to the plane $q \otimes q'$. Both histograms show a clear exclusive peak at the mass of the proton. The coplanarity cut removes the vast majority of the continuum events without significantly reducing the exclusive signal.

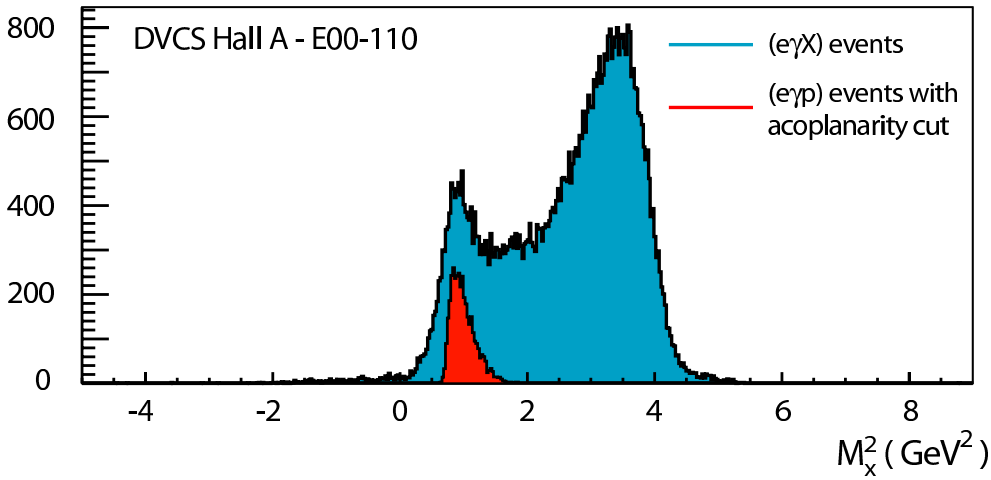

Figure 55: $\mathrm{H}(e, e'\gamma)X$ missing-mass squared spectrum.

3.11 E01-001

New Measurement of (G_E/G_M) for the Proton

J. Arrington and R. E. Segel, spokespersons.

Experiments using the polarization-transfer technique have reported [58, 59] that in the $1 < Q^2 < 5.6$ GeV^2 range the ratio of proton electric to magnetic form factor falls off linearly with increasing Q^2. These results appear to contradict Rosenbluth extractions of the form factor, which yield approximate form factor scaling ($\mu_p G_E/G_M \approx 1$) [60]. However, the uncertainties in the Rosenbluth extractions are larger than those from the polarization-transfer experiments, especially at high Q^2, and in most cases the disagreement between Rosenbluth and polarization-transfer measurements is only 1–2 σ. JLab E01-001 was undertaken with the goal of performing Rosenbluth separations with uncertainties in G_E/G_M comparable to those achieved with polarization transfer.

The experiment was run in May 2002 and the extraction of the form factors has been submitted for publication in PRL [61]. The elastic cross sections used in the Rosenbluth separation were extracted from measurements of the struck proton, as opposed to previous Rosenbluth separation experiments where electrons were detected. Detecting the protons has several important advantages [61]: (1) the momentum of the detected particles is independent of ε for a fixed Q^2 value, (2) the cross sections vary slowly as a function of ε, and (3) the radiative corrections are smaller than for electron detection. Separations were performed at three values of Q^2, 2.64, 3.20 and 4.10 GeV^2, using beam energies of 1.912, 2.262, 2.842, 3.772, and 4.702 GeV. While the left HRS spectrometer was obtaining spectra at the Q^2 of interest, the right spectrometer was set at $Q^2 = 0.50$ GeV^2 and serving as a luminosity monitor. The luminosity monitor is not used in the present left arm results, although the initial analysis of the right arm results was consistent with the assumed uncertainties in the luminosities. At two kinematic settings, coincidence $p(e, e'p)$ data were taken with the right spectrometer detecting the electrons. These data are used to check efficiencies and spectral shapes.

Figure 56 shows the missing momentum (δp) spectrum; measured proton momentum minus the momentum calculated from the measured scattering angle, assuming elastic scattering kinematics. The spectrum is dominated by the elastic peak but there are two backgrounds that have to be subtracted:

1. Reactions, primarily quasi-elastic scattering, in the target end caps. This background was determined by taking data on a dummy target at every setting.

2. Protons from the $\gamma p \to \pi^0 + p$ (and $\gamma p \to \gamma p$) reaction initiated by bremsstrahlung in the target upstream end cap. These protons were significant only at forward angles and, because of the pion's finite mass, their spectrum cuts off below the elastic peak. Nevertheless, they had to be taken into account. Their contribution

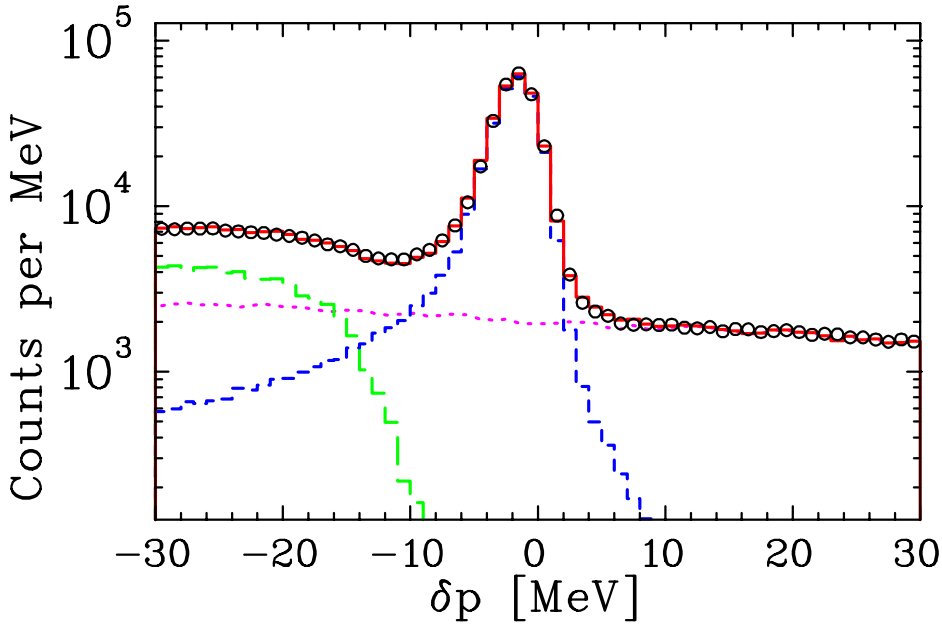

Figure 56: Missing momentum spectrum for the low ε point at $Q^2 = 3.20$ GeV^2. The black circles indicate the data from the LH2 target while the red histogram indicates the total simulated spectrum. The spectrum is decomposed into contributions from the elastic peak (blue), protons from the $\gamma p \to \pi^0 p$ reaction (green) and protons coming from the Aluminum end caps of the target (magenta).

was modeled using a calculated bremsstrahlung spectrum and an s^{-7} cross section dependence, scaled to the measured background below the elastic peak.

The elastic peak was modeled using the Monte Carlo code SIMC. The simulated δp resolution was somewhat narrower than in the data and did not have the small non-Gaussian tails observed in the data. These tails were due to poor track reconstruction for a small fraction of the events. The coincidence measurements allowed us to isolate a clean sample of elastic protons by applying tight cuts on the elastic peak for the electrons and cutting out the end cap contributions. The resolution in the simulation was then adjusted to match the data.

The protons in the elastic peak are isolated by subtracting away the two significant backgrounds. First the dummy target spectrum is normalized to the spectrum from the LH2 target at δp values high enough to be above the tail of the elastic peak. The normalized spectrum is then subtracted from the LH2 spectrum leaving the $\gamma p \to \pi^0 p$ and elastic protons. The spectrum at low δp is used to normalize the simulated $\gamma p \to \pi^0 p$ spectrum to the (LH2-normalized dummy) spectrum with allowance made for the low-energy radiative tail of the elastic peak. The magnitude of the tail is estimated by matching the simulated elastic spec-

trum to the (LH2-normalized dummy) spectrum in a narrow region about the elastic peak. The normalized $\gamma p \to \pi^0 p$ spectrum is then subtracted away leaving only the elastically scattered protons. Reduced cross sections are then obtained as the ratio of the background-subtracted LH2 to the simulated elastic spectrum over a region about the elastic peak. For the final cross sections the width of the window used in determining the data to simulation cross section varied from 15 to 31 MeV (larger windows for settings where the elastic peak was wider). With these windows the protons from the end caps were ∼10% of the elastic yield and pion photoproduction protons less than 2%. The sensitivity of the extracted cross sections to the window widths was tested and even with very wide or narrower windows, yielding larger or smaller corrections for $\gamma p \to \pi^0 p$, the change in cross sections was no more than about 1%. With the windows that were actually used it is estimated that the uncertainty in the peak shape results in an uncertainty of ∼0.3% in the reduced cross sections.

The reduced cross sections are shown as a function of ε for the three Q^2 values in Fig. 57. The uncorrelated errors on the individual points are typically 0.5–0.6%, and there is an additional systematic uncertainty on the ε-dependence (*i.e.* the Rosenbluth slope) of ∼0.6%. The overall normalization uncertainty is ∼3%.

The radiative corrections that are applied to the data [62] are very significant and are built into the Monte Carlo elastic scattering simulation. The ε dependence of the radiative corrections results in a change in G_E/G_M that is comparable to the difference between Rosenbluth and polarization-transfer determinations. When the electrons are detected, the ε dependence of the radiative corrections is about twice as large and of the opposite sign. The fact that the result is the same regardless of which particle is detected is strong evidence that the bremsstrahlung is being correctly handled.

In the one-photon approximation the reduced cross section can be written $\sigma_R = \tau G_M^2 + \varepsilon G_E^2$, where ε is the the virtual-photon polarization parameter. Figure 58 shows the extracted values of $\mu G_E/G_M$ from the present experiment, compared to existing Rosenbluth and polarization-transfer measurements. The present results are consistent with the previous Rosenbluth results and are in significant disagreement with the polarization-transfer determinations.

Accepting the E01-001 results leaves but two alternatives:

1. There is a flaw in the polarization-transfer experiments or formalism. A continuation of the polarization-transfer experiments in Hall C has been approved [64] and this will provide a check on the Hall A results. A separate check on the polarization-transfer results using a polarized proton target in Hall C was deferred with regret by PAC 26 [65].

2. The Rosenbluth data are not being interpreted correctly. The possibility that two-photon exchange corrections could explain the discrepancy is being intensively pursued and calculations [66, 67] have shown that the contributions to the elastic

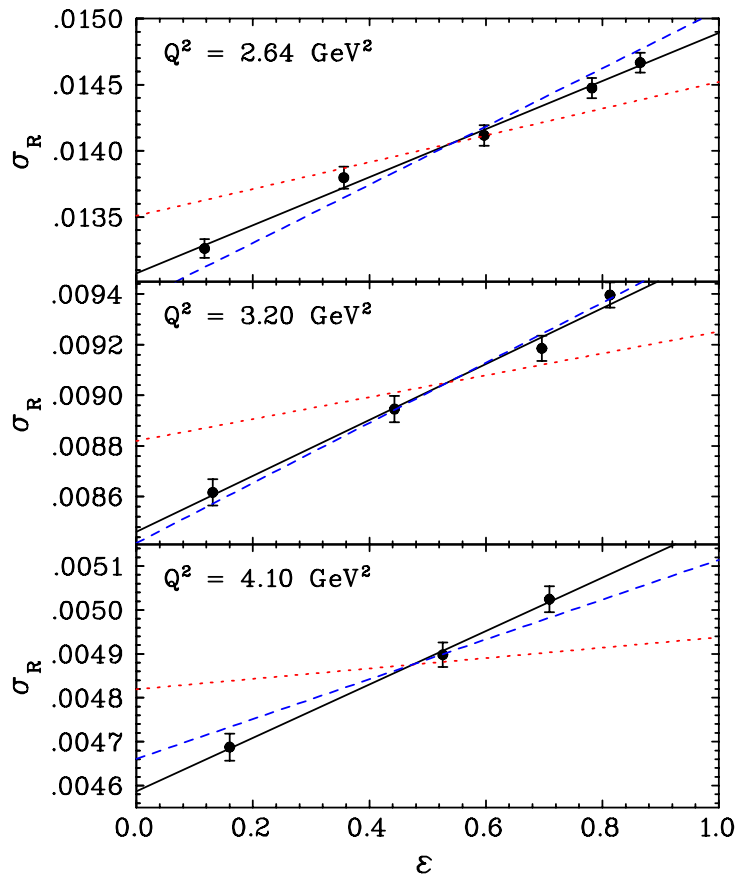

Figure 57: Reduced cross sections as a function of ε. The solid line is the best linear fit to the data, the dashed line gives the slope assuming $\mu G_E = G_M$, and the dotted line is the slope one obtains using the polarization transfer fit to G_E/G_M.

cross section from this mechanism could be significant. Considerable experimental and theoretical efforts are underway to determine if this is indeed the case.

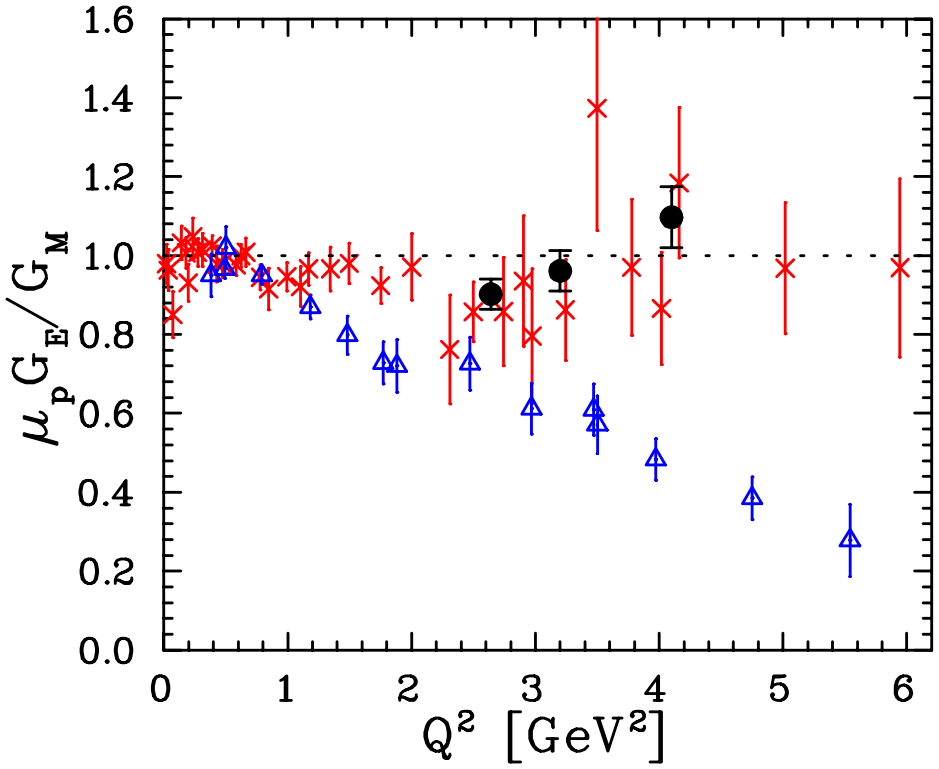

Figure 58: Extracted values of $\mu G_E/G_M$ from the present measurement (solid circles), a global analysis of previous Rosenbluth extractions ('×') [63], and the polarization transfer measurements (triangles).

3.12 E01-012

Measurement of neutron (^{3}He) spin structure functions in the resonance region.

J. P. Chen, S. Choi, N. Liyanage, spokespersons
P. Solvignon, graduate student

Experiment E01-012 ran in January and February, 2003. The goal of this experiment is to perform a precision extraction of the neutron spin structure function g_1^n and the virtual photon asymmetry A_1^n in the resonance region over a moderate Q^2 range (up to $Q^2 = 4$ GeV^2) using Hall A polarized ^{3}He target. The results from this experiment, combined with deep inelastic scattering data, will provide a precision test of quark-hadron (Bloom-Gilman) duality predictions for neutron spin structure function g_1^n and the virtual photon asymmetry A_1^n. The Bloom-Gilman duality has been experimentally demonstrated for the spin-independent structure function F_2. Duality is observed when the smooth scaling curve at high momentum transfer is an average over the resonance bumps at lower momentum transfer, but at the same value of the scaling variable x_{Bj}. Results from E01-012 will enable one of the first precision tests of spin and flavor dependence of quark-hadron duality. The demonstration of duality for the spin structure functions will enable the use of resonance data to study the nucleon spin structure in the very large x_{Bj} region.

In this experiment we used the polarized beam and the polarized ^{3}He target to measure the inclusive $^3\vec{H}e(e,e')X$ reaction. Both Hall A High Resolution spectrometers (HRS) were used in a symmetric configuration in electron detection mode. Three beam energies, 3, 4 and 5 GeV, were used with spectrometer angles of 25° and 32°. At each kinematic setting parallel and perpendicular asymmetries were measured with the target spin parallel and perpendicular to the electron beam respectively. The Q^2/W phase-space covered by this experiment is shown in Fig. 59.

Current Status: In the last year Patricia Solvignon, an E01-012 thesis student from Temple University, has made considerable progress in the data analysis. She has completed the extraction of raw asymmetries and cross sections. The acceptance corrections and detector inefficiency corrections have been throughly studied and applied to the data. The cross sections measured simultaneously on the two HRS spectrometers agree at the 5% level. Particle identification cuts used to reject pions have been studied and optimized.

The measured parallel and perpendicular asymmetries were used to calculate raw virtual photon asymmetries, A_1 and A_2 for ^{3}He. The preliminary results for $A_1^{^3\mathrm{He}}$ are shown in Fig. 60. No radiative corrections have been applied to these results. In the figure $A_1^{^3\mathrm{He}}$ measured in the resonance region in this experiment is compared to $A_1^{^3\mathrm{He}}$ in the DIS region measured in Hall A experiment E99-117. It is interesting to note that the resonance region $A_1^{^3\mathrm{He}}$ measured at all four Q^2 values

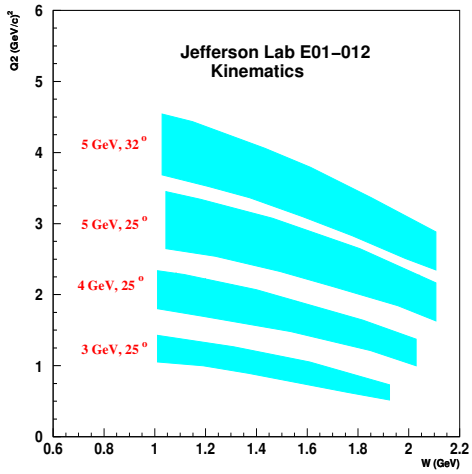

Figure 59: The Q^2 and W coverage for E01-012

of E01-012 seem to show a trend to cross over from negative to positive values in the same x range where DIS-$A_1^{^3\mathrm{He}}$ also crosses over.

The main remaining data analysis tasks for E01-012 are applying radiative corrections and extracting neutron asymmetries from ^{3}He asymmetries.

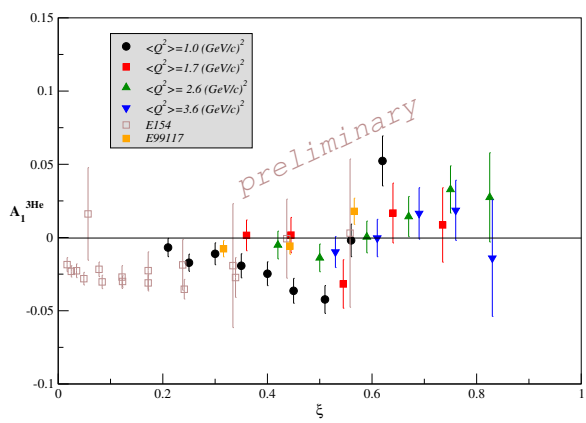

Figure 60: Preliminary results for ^{3}He virtual photon asymmetry A_1 from E01-012. Radiative corrections and Nitrogen dilution corrections have not been applied.

3.13 E01-020

$(e,e'p)$ Studies of the Deuteron at High Q^2

W. Boeglin, M. Jones, A. Klein, P. Ulmer, E. Voutier, spokespersons

Goals of the Experiment The goal of experiment E01-020 is to provide a systematic study of the ^{2}H$(e,e'p)n$ reaction down to very short distance scales. It covers kinematics from below to above the quasi-free peak over a wide range of four-momentum transfers ($Q^2 = 0.8, 2.1$ and 3.5 GeV^2) and missing momenta (p_m up to 0.5 GeV/c).

Each kinematics emphasizes different aspects of the reaction mechanism. For energy transfers below the quasi-free peak (x_{bj}>1), non-nucleonic effects (virtual nucleonic excitations and meson exchange currents) are expected to be minimized since the energy transfer is relatively low. Furthermore, for protons detected along $\vec{q}$, Final State Interactions (FSI) are also expected to be minimized since they would shift strength predominantly from high to low recoil momentum and the one-body response falls off sharply with recoil momentum. Thus, the high x_{bj} parallel kinematics measurements are expected to be mainly sensitive to aspects of the deuteron's short-range structure.

By examining (for fixed Q^2 and p_m) the angular distribution of neutrons in the final hadronic center-of-mass system, one can quantitatively study FSI. Such a quantitative study will be facilitated by a comparison with a generalized eikonal approximation, expected to be especially valid at high momentum transfers (and consequent high neutron-proton relative energies in the final state). The angular distribution is expected to show a large peak near 90° about the $\vec{q}$ direction. The success of theories in predicting this shape will give us confidence in correcting for FSI effects in extracting the deuteron structure. This understanding will also be useful for studies of short-range correlations using $(e,e'p)$ on heavier nuclei.

Finally, a separation of the R_{LT} interference response function will be performed in quasi-free kinematics (x_{bj}=1) at each Q^2 for p_m up to 0.5 GeV/c to test the validity of relativistic models. Proper treatment of relativity is essential at kinematics where we will probe the deuteron's short-range structure.

Status of the Analysis The analysis described here has been carried out by two Ph.D. thesis students, one at Florida International University, L. Coman (W. Boeglin, adviser), and one at Old Dominion University (ODU), H. Ibrahim, (P. Ulmer, adviser), as well as an ODU postdoctoral research associate (R. Roche), and graduate student (K. Foe) and the experiment spokespersons.

The first post-run analysis pass is ready to commence. Various calibrations have been completed in preparation for this pass. The spectrometer optics database has been optimized using sieve-slit data and multi-foil carbon targets. Other aspects of the database have also been optimized: scintillator timing offsets and gain

matching and VDC time offsets. Kinematics calibrations using ^{1}H(e,e'p) have been performed showing good agreement for missing-mass peak position among the various kinematics. Spectrometer pointing offsets have been determined for all kinematics and the absolute spectrometer angles have been obtained using a set of elastic ^{1}H(e,e'p) kinematics at fixed beam energy. All the ESPACE header files have been updated accordingly. A set of tools to facilitate the computation of electronics dead times for a list of runs has been developed [85].

VDC tracking efficiency has been extensively studied [86]. One of the main findings was that secondary peaks in the focal plane spectra for certain kinematics arise from rescattering in the spectrometer exit vacuum window frame. These anomalous peaks are virtually absent in the coincidence data and can be further reduced through R-function [87] cuts. In addition, after visual inspection of many event tracks using a newly developed event display tool [88], we have determined the requisite per-plane hit multiplicities for candidate tracks.

Beam position calibrations have been carried out based on a "bulls-eye" scan in concert with survey data. However, rastered data taken with a thin carbon foil (oriented normally to the beam) shows an anomalous correlation between the lateral beam position and reaction point along the beam inferred using the BPMs and spectrometers. This correlation can be removed if a factor of roughly 1.3 is applied to the lateral beam position as given by the BPMs.

Target boiling studies are now nearing completion. Preliminary results for deuterium (our experiment employed the cigar-shaped cells) are shown in Figs. 61 and 62. Since we normally used a 2mm $\times$ 2mm nominal raster size, we expect a density correction of 9% for a 100 μA beam current. We expect this to result in a roughly 1% systematic uncertainty in the cross sections.

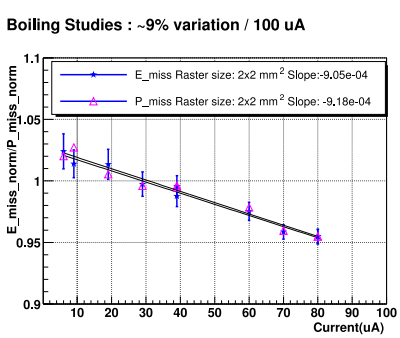

Figure 61: Relative yield normalized to beam charge as a function of beam current for a nominal 2 mm $\times$ 2 mm raster size.

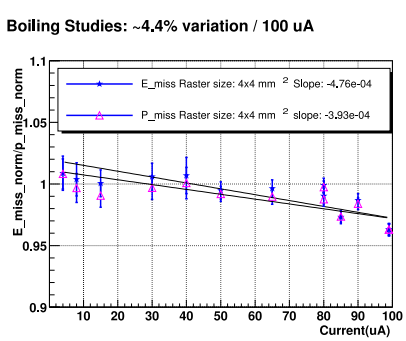

Figure 62: Relative yield normalized to beam charge as a function of beam current for a nominal 4mm $\times$ 4mm raster size.

Remaining Analysis Tasks We are still working on extracting the trigger (*i.e.* scintillator) efficiencies. Following this, we will check the absolute normalization from ^{1}H(e,e'p) elastic scattering. Presently, we expect this to provide merely a cross check giving us confidence in extracting absolute cross sections from the data. Once the cross sections are determined we will proceed with phase-space matching and subsequent extraction of the R_{LT} response function.

Preliminary Results Our yields have not yet been absolutely normalized to produce cross sections, but we have nevertheless produced preliminary distributions of data normalized to a simple PWIA model. The systematic uncertainties should currently be taken to be ±20% until we have performed the necessary cross checks. The distributions are shown in Fig. 63 along with calculations of Laget [89]. The gross features are well reproduced by the calculation indicating that the Glauber treatment may indeed be appropriate for FSI at these outgoing proton energies.

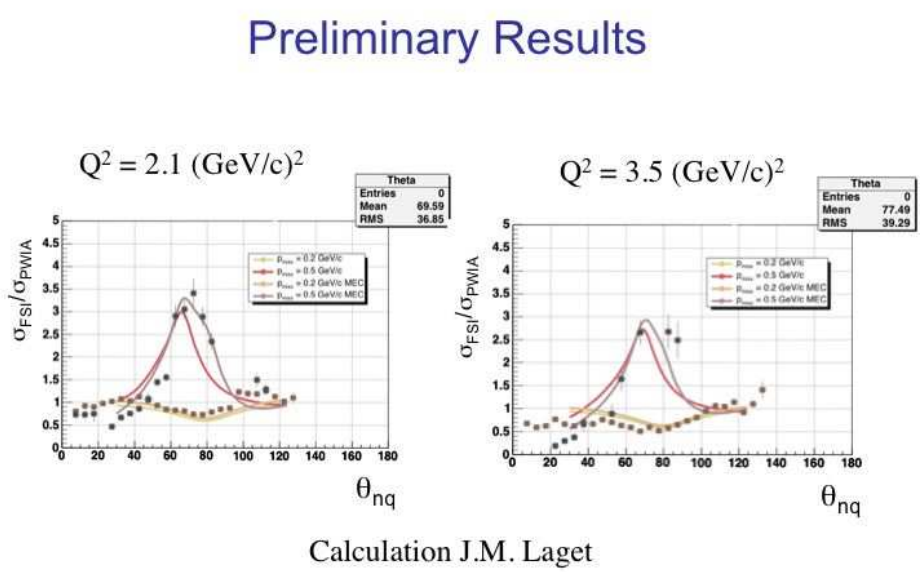

Figure 63: Preliminary distributions *vs.* the neutron angle relative to $\vec{q}$ normalized to a PWIA calculation. The curves are calculations from Laget based on a Glauber treatment of FSI.

3.14 E04-012

High-Resolution Search for $\Theta^+(1540)$ Partners

P. E. Reimer and B. Wojtsekhowski, Spokespersons,
and
the Hall A Collaboration.

Experiment E04-012 carried out a search for possible partners of the speculative $\Theta^+(1540)$ pentaquark. Approved by PAC25 in January, 2004, the experiment took data in late May, 2004, using the same experimental configuration as the preceding Hypernuclear Spectroscopy experiment, E94-107. The septum magnets and the RICH detector were essential for this experiment.

Three reaction channels were studied in which partners of the Θ^+ can be expected to be observed:

- $\mathrm{H}(e, e'K^+)\Sigma^\circ_{\overline{10}}$ in the range $M_{\Sigma^\circ_{\overline{10}}} = 1530$–$1820$ MeV.
- $\mathrm{H}(e, e'\pi^+)N^\circ_{\overline{10}}$ in the range $M_{N^\circ_{\overline{10}}} = 1600$–$1830$ MeV.
- $\mathrm{H}(e, e'K^-)\Theta^{++}$ in the range $M_{\Theta^{++}} = 1500$–1600 MeV.

Here, the $\Sigma^\circ_{\overline{10}}$ and the $N^\circ_{\overline{10}}$ are strange and non-strange members, respectively, of the antidecuplet symmetry group proposed in the framework of a Chiral Quark Soliton Model by Diakonov *et al.* [90] (Figure 64). The Θ^{++} partner is a prediction of an alternative pentaquark model by Capstick *et al.* [91], which proposes an isotensor multiplet, as shown in Table 9.

The experiment used a beam energy of 5 GeV, the standard 15 cm hydrogen cryotarget, and both HRSs, positioned at 6° (Fig. 65). Positively or negatively charged kaons were identified in the left HRS using a combination of the RICH counter, two aerogels, and a coincidence timing cut centered on the kaon coincidence peak. The charged pion channel was measured simultaneously with the kaon data and could be extracted by applying different PID cuts. The right HRS detected electrons and employed a gas Čerenkov for pion rejection.

State	Content	I_z	Strong decay modes
Θ^-	$dddd\bar{s}$	-2	
Θ^0	$uddd\bar{s}$	-1	nK^0
Θ^+	$uudd\bar{s}$	0	nK^+,pK^0
Θ^{++}	$uuud\bar{s}$	1	pK^+
Θ^{+++}	$uuuu\bar{s}$	2	

Table 9: Proposed isotensor multiplet (Capstick *et al.* [91]).

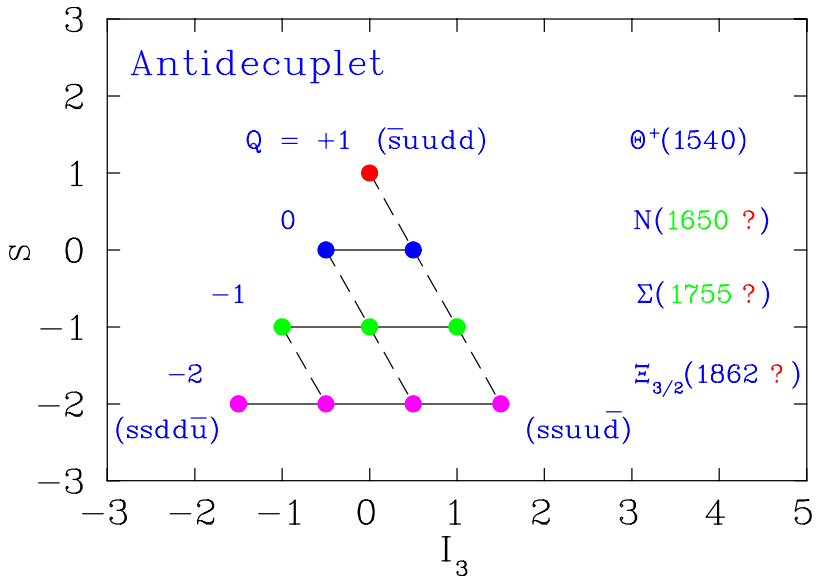

Figure 64: Proposed antidecuplet symmetry group (Diakonov *et al.* [90]).

Potential resonances were identified by reconstructing the missing mass of the unobserved particle(s). The kinematics were chosen to cover missing-mass ranges that included most of the current theoretical predictions for the masses of pentaquark partners. In general, the width of the pentaquark partners is predicted to be comparable to that of the Θ^+, *i.e.* 2–40 MeV; thus, the experiment specifically searched for narrow resonances.

Thanks to the recent installation of the S2m scintillator planes, which offer excellent timing performance, a coincidence time resolution of 600 ps FWHM was achieved. At the kinematics of the experiment, pion and kaon coincidences were separated by more than 2.5 ns, allowing time-of-flight to be used for particle identification as well as accidental rejection. Accidentals were further reduced by applying a vertex cut, requiring the reaction points seen by each spectrometer in a coincidence event to be close to each other. The vertex resolution was 2.5 cm FWHM, significantly smaller than the 15 cm length of the target cell.

The performance of the hadron arm PID system is illustrated in Fig. 66. The upper panel shows the distribution of reconstructed Čerenkov photon angles in the RICH before any PID cuts; one observes a dominant pion peak. The lower panel shows the same distribution after aerogel, coincidence time-of-flight, and vertex cuts; kaons and pions are cleanly separated. The final kaon selection is made by applying the RICH angle cut shown in the figure, resulting in an overall pion rejection factor of $3 \cdot 10^4$ and a K/π ratio of > 20 in the final event sample.

Figure 67 shows two calibration spectra that were obtained in regions of known particles. The upper panel shows the neutron missing-mass peak, demonstrating

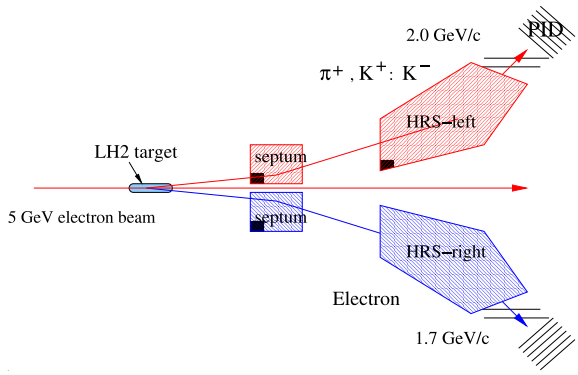

Figure 65: Experimental setup for E04-012.

the achieved resolution of the system, $\sigma = 1.5$ MeV. The lower panel illustrates the ability to identify strange resonances, the $\Lambda(1116)$ and the $\Sigma(1193)$, by detecting coincident kaons.

Results of the $\Sigma^{\circ}_{\overline{10}}$ search are shown in Fig. 68. The upper and lower panels show the same missing-mass spectrum, once with a fit to the background only and once with a fit to the background plus a Gaussian resonance in the region of a candidate peak. In the analysis, the region in which these fits are done is shifted from bin to bin across the entire missing-mass acceptance, and the improvement in χ^2 of the fit is recorded for each step. The most significant peak yields the largest χ^2 improvement. The intrinsic width of the resonance was taken to be $\sigma = 5$ MeV, and an instrumental resolution of $\sigma = 1.5$ MeV was assumed for this particular example; other intrinsic widths were also studied. Similar spectra have been obtained for the other two searches, the one for the Θ^{++} and the one for the $N^{\circ}_{\overline{10}}$. In our preliminary analysis, no statistically significant peaks were found in any of the three reaction channels that we studied.

The analysis is currently ongoing. Open items include a detailed study of the efficiencies, especially of that of the trigger, proper modeling of the background in terms of known broad resonances, and determination of upper limits on production cross sections for the pentaquark partner states. A draft of a publication is in preparation and expected to be circulated in Spring, 2005.

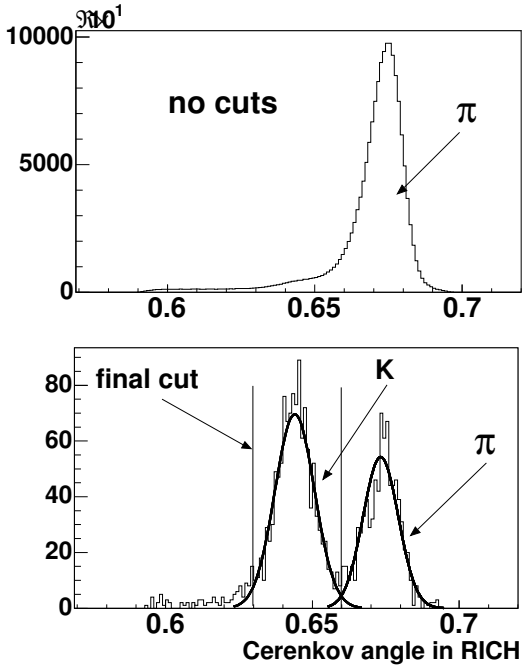

Figure 66: Performance of the hadron PID system for E04-012 (see text for details).

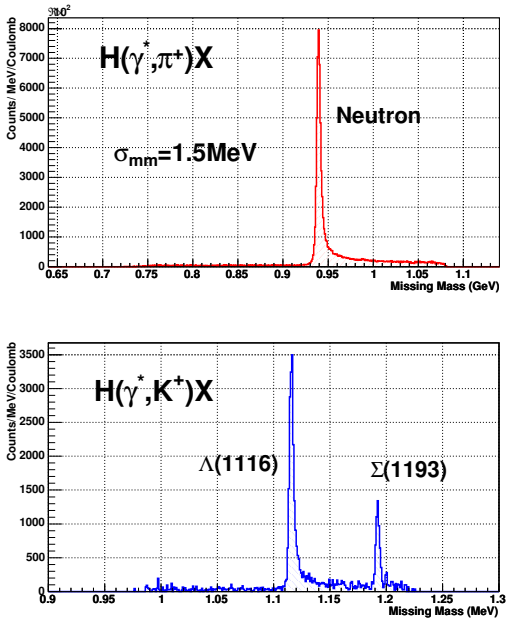

Figure 67: Neutron calibration spectrum (upper panel), illustrating the achieved missing-mass resolution, and mass calibration of the well-known Λ and Σ resonances (lower panel).

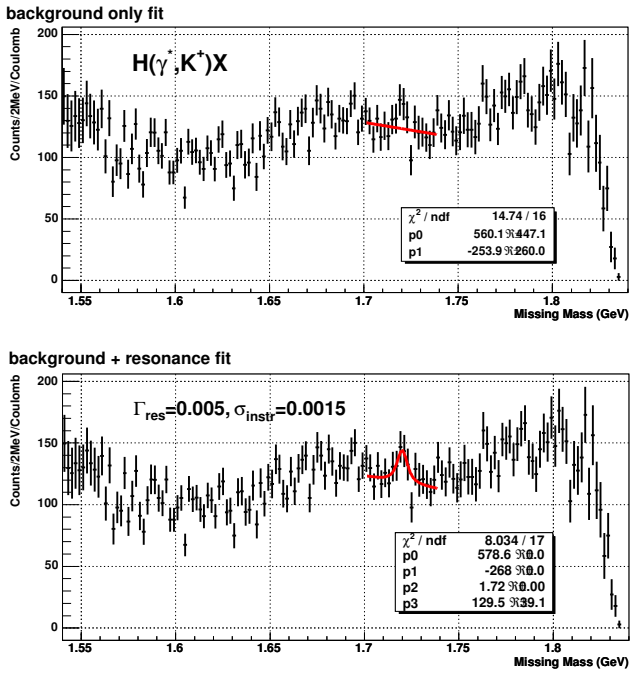

Figure 68: Preliminary missing-mass spectrum obtained in the $\Sigma^{\circ}_{\overline{10}}$ search. The upper and lower panels show a fit to the background and to a candidate peak, respectively, to illustrate the search technique. The broad structures across the region are known wide resonances. No statistically significant narrow peak has been observed in our preliminary analysis.

4 References

[1] Y-C. Chao *et al.*, *Energy Spread Monitoring for the JLAB Experimental Program: Synchrotron Light Interferometers, Optical Transistion Radiation Monitors and Wire Scanners*, in Proc. of the 11th Beam Instrumentation workshop, Knoxville, Tennessee, ed. Thomas Shea, R. Coles Sibley III, AIP Conf. Proc. **732** (2004). 12

[2] T. Mitsuhashi, *Twelve Years of SR Monitor Development at KEK*, in Proc. of the 11th Beam Instrumentation workshop, Knoxville, Tennessee, ed. Thomas Shea, R. Coles Sibley III, AIP Conf. Proc. **732** (2004). 14

[3] P. Chevtsov *et al.*, *Synchrotron Light Interferometer at Jefferson Lab*, in Proc. of the 2003 PAC, http://accelconf.web.cern.ch/accelconf/p03/PAPERS/WPPB068.PDF. 14

[4] Eugene Chudakov, http://www.jlab.org/∼gen/talks/talk_ septum_ heating_ sim_ 1.ps.gz. 19

[5] http://hallaweb.jlab.org/equipment/targets/cryotargets/. 20

[6] D. Armstrong, B. Moffit and R. Suleiman, JLAB-TN-03017. 20

[7] F. Garibaldi, S. Frullani, P. Markowitz and J. LeRose, spokespersons, JLab Experiment E94-107, *High Resolution 1p shell Hypernuclear Spectroscopy.* 22, 59, 67

[8] ELJEN Technology, `http://www.eljentechnology.com`. 22

[9] XP2282B photomultiplier tube, PHOTONIS, `http://www.photonis.com`. 22

[10] Jefferson Lab Hall A Annual report, 2003. 27

[11] S. Nanda and D. Lhuillier, *Conceptual Design Report for Hall A Compton Polarimeter Upgrade*, unpublished. 31, 34, 35

[12] H. Sakai *et al.*, Nucl. Instrum. Methods Phys. Res. A **445** (2000) 113. 32

[13] J. Urukawa *et al.*, Nucl. Instrum. Methods Phys. Res. A **445**, 113 (2000). 32

[14] M. Bregant *et al.*, hep-ex/0202046. 32

[15] D. Berns, Research Electro Optics, http://www.reoinc.com/. 35

[16] I. Freitag, InnoLight GmbH, http://www.innolight.de/. 31

[17] R. W. P. Drever *et al.*, Appl. Phys. B **31**, 145 (1983). 32

[18] W. Bertozzi, E. Piasetzky, J. Watson and S. Wood, spokespersons, JLab Experiment E01-015, *Studying the internal small-distance structure of Nuclei via the triple coincidence (e,e'p+N) measurement.* 36

[19] J. Annand, D.W. Higinbotham, R. Lindgren and V. Nelyubin, spokespersons, JLab Experiment E01-014, *Precision measurement of electroproduction of* π^0 *near threshold: a test of chiral QCD dynamics.* 36, 37

[20] G. Cates, K. McCormick, B. Reitz and B. Wojtsekhowski, spokespersons, JLab Experiment E02-013, *Measurement of the neutron electric form factor* G_n^E *at high* Q^2. 36, 37

[21] W. Bertozzi, B.E. Norum, T. Tamea and K. Wang, spokespersons, JLab Experiment E02-101, *Exclusive study of deuteron electrodisintegration near*

threshold. 36, 37

[22] W. Bertozzi, S. Gilad, D.W. Higinbotham, B.E. Norum and S. Širca, spokespersons, JLab Experiment E02-108, *Measurement of A_x and A_z asymmetries in the quasi-elastic polarized $^3He(\vec{e},e'd)$ reaction*. 36, 37

[23] J.P. Chen, X. Jiang and J.C. Peng, spokespersons, JLab Experiment E03-004, *Measurement of single target-spin asymmetry in semi-inclusive pion electroproduction on a transversely polarized ^3He target*. 36, 37

[24] B. Wojsekhowski, P.E. Reimer and V. Nelyubin, spokespersons, JLab Experiment E05-013, *High Resolution Study of the Resonance in nK^+ System*. 36, 37

[25] J.-C. Peng, L.Y. Zhu, J.-P. Chen and X. Jiang, spokespersons, JLab Experiment E04-114, *A Measurement of the Flavor Asymmetry through Charged Meson Production in Semi-Inclusive Deep-Inelastic Scattering*. 36, 37

[26] `http://hallaweb.jlab.org/root/`. 44

[27] M. Rvachev, F. Benmokhtar, E. Penel-Nottaris *et al.*, nucl-ex/0409005. 54

[28] F. Benmokhtar, M. Rvachev, E. Penel-Nottaris *et al.*, Phys. Rev. Lett. **94**, 082305 (2005). 54

[29] D. Drechsel, O. Hanstein, S. S. Kamalov, L. Tiator and S. N. Yang, www.kph.uni-mainz.de/MAID. 56

[30] D. Drechsel, O. Hanstein, S. S. Kamalov, L. Tiator and S. N. Yang, www.kph.uni-mainz.de/MAID/dmt/dmt2001.html. 56

[31] R. A. Arndt, W. J. Briscoe, R. L. Workman and I. I. Strakovsky, gw-dac.phys.gwu.edu. 56

[32] T. Sato and T.-S. H. Lee, Phys. Rev. C **63**, 055201 (2001). 56

[33] C.B. Dover and D. J. Millener, in Modern Topics in Electron Scattering (Word Scientific Singapore, 1990, B. Frois and I. Sick eds.). 59

[34] H. Bando, T. Motoba and J. Zofka, Int. J. Mod. Phys. A **5**, 4021 (1990).

[35] T. Myioshi *et al.*, Phys. Rev. Lett. **90**, 232502 (2003). 59

[36] R.A. Williams. Chueng-Ryong Ji and C. R. Cotanch, Phys. Rev. C **46**, 1617 (1992). 60

[37] J.C. David, C. Fayard, G.-H. Lamot and B. Saghai, Phys. Rev. C **53**, 2613 (1996); T. Mizutani, C. Fayard, G.-H. Lamot, and B. Sagahi, Phys. Rev. C **58**, 75 (1998). 65

[38] T. Mart and C. Bennhold, Phys. Rev. C **61**, 012201 (2000). 65

[39] A. Deur, J.-P. Chen, F. Garibaldi, spokespersons, JLab Experiment E97-107, *The GDH Sum Rule and the Spin Structure of ^3He and Neutron using Nearly Real Photons*; K. Kumar, D. Lhuillier, spokespersons, JLab Experiment E-99-115, *Constraining the Nucleon Strangeness Radius in Parity Violating Electron Scattering*. 60

[40] J. Alcorn *et al.*, Nucl. Instrum. Methods Phys. Res. A **522**, 294 (2004). 59

[41] F. Cusanno *et al.*, Nucl. Instrum. Methods Phys. Res. A **502**, 251 (2003). 63

[42] S.J. Brodsky and G.P. Lepage, Phys. Rev. D **22**, 2157 (1980). 73

[43] G.R. Farrar and H. Zhang, Phys. Rev. Lett. **41**, 1721 (1990); Phys. Rev.

D **41**, 3348 (1990). 73
[44] A.S. Kronfeld and B. Nizic, Phys. Rev. D **44**, 3445 (1991). 73
[45] M. Vanderhaeghen, P.A.M. Guichon and J. Van de Wiele, Nucl. Phys. **A 622**, 144c (1997). 73
[46] T. Brooks and L. Dixon, Phys. Rev. D **62**, 114021 (2000). 7, 73, 74
[47] A.V. Radyushkin, Phys. Rev. D **58**, 114008 (1998). 73
[48] M. Diehl, T. Feldmann, R. Jakob and P. Kroll, Eur. Phys. J. C, **8**, 409 (1999). 73
[49] V. Mamyan *et al.*, Izvestia National Academy of Sciences of Armenia (submitted for publication). 74
[50] M. Diehl *et al.*, hep-ph/0408173. 7, 75
[51] D. J. Hamilton *et al.*, submitted to Phys. Rev. Lett.(nucl-ex/0410001). 74
[52] H.W. Huang and P. Kroll, unpublished. 7, 74
[53] F. Cano and J.-M. Laget, Phys. Lett. B **551**, 317 (2003). 7, 74
[54] G.A. Miller, Phys. Rev. C **69**, 052201(R) (2004). 7, 74
[55] K. Aniol *et al.*, Phys. Rev. C **69**, 065501 (2004). 76
[56] F.E. Maas, *et al.*, nucl-ex/0412030. 7, 79
[57] T. Ito *et al.*, Phys. Rev. Lett. **92**, 102003 (2004). 7, 79
[58] M. K. Jones *et al.*, Phys. Rev. Lett. **84**, 1398 (2000). 88
[59] O. Gayou *et al.*, Phys. Rev. Lett. **88**, 092301 (2002). 88
[60] J. Arrington, Phys. Rev. C **68**, 034325 (2003). 88
[61] I. A. Qattan *et al.*, nucl-ex/0410010. 88
[62] R. Ent *et al.*, Phys. Rev. C **64**, 054610 (2001). 90
[63] J. Arrington, Phys. Rev. C **69**, 022201(R) (2004). 8, 92
[64] C. F. Perdrisat, V. Punjabi, M.K. Jones and E. Brash, spokespersons, JLab Experiment E04-108, *Measurement of* G_E^p/G_M^p *to* $Q^2 = 9\ GeV^2$ *via Recoil Polarization.* 90
[65] X. Zheng, J.R. Calarco and O.A. Rondon, spokespersons, JLab Proposal PR04-111, *Measurement of* G_E^p/G_M^p *using Elastic Polarized Reaction* $p(e,e'p)$ *up to* $Q^2 = 5.6\ GeV^2$. 90
[66] P. G. Blunden, W. Melnitchouk and J.A. Tjon, Phys. Rev. Lett. **91**, 142304 (2003). 90
[67] Y. C. Chen *et al.*, Phys. Rev. Lett. **93**, 122301 (2004). 90
[68] W. Bertozzi, K. Fissum, A. Saha and L. Weinstein, spokespersons, JLab Experiment E89-003, *Study of the Quasi-Elastic* $(e,e'p)$ *Reaction in* ^{16}O *at High Recoil Momentum.* 83
[69] J. Gao *et al.*, Phys. Rev. Lett. **84**, 3265 (2000). 83
[70] N. Liyanage *et al.*, Phys. Rev. Lett. **86**, 5670 (2001). 83
[71] F. Garibaldi *et al.*, Nucl. Instrum. Methods Phys. Res. A **314**, 1 (1992). 83
[72] E. Cisbani *et al.*, *A Waterfall Target System for Hall A at Jefferson Lab*, INFN/ISS **97/04** (1997). 83
[73] D. Muller, *et al.,* Fortsch. Phys. **42**, 101 (1994). 85
[74] X. Ji, Phys. Rev. Lett. **78**, 610 (1997). 85

[75] A.V. Radyushkin, Phys. Lett. B **380**, 417 (1996). 85
[76] J.C. Collins, L. Frankfurt and M. Strikman, Phys. Rev. D **56**, 2982 (1997). 85
[77] F. Sabatie, P.Y. Bertin, C.E. Hyde-Wright and R. Ransome, spokespersons, JLab Experiment E00-110, *Deeply Virtual Compton Scattering at 6 GeV*; `http://hallaweb.jlab.org/experiment/DVCS/`. 85
[78] F. Sabatie, P.Y. Bertin, C.E. Hyde-Wright and E. Voutier, spokespersons, JLab Experiment E03-106, *Deeply Virtual Compton Scattering on the Neutron*; `http://hallaweb.jlab.org/experiment/DVCS/`. 85
[79] M. Burkardt, Phys. Lett. B **595**, 245 (2004). 85
[80] M. Burkardt and G.A. Miller, hep-ph/0312190. 85
[81] M. Diehl, Eur. Phys. J. C **25**, 223 (2002); [Erratum-ibid. C **31**, 277 (2003)]. 85
[82] A.V. Belitsky, X. Ji and F. Yuan, Phys. Rev. D **69**, 074014 (2004). 85
[83] M. Diehl, T. Gousset, B. Pire and J.P. Ralston, Phys. Lett. B **411**, 193 (1997).
[84] A.V. Belitsky, D. Muller and A. Kirchner, Nucl. Phys. **B 629**, 323 (2002). 85 85
[85] R. Roche (based on the computer code of B. Reitz), http://www.physics.odu.edu/∼ulmer/experiments/e01020/tools/edt/ (2004). 96
[86] P. Ulmer, *VDC Tracking in Experiment E01-020*, http://www.physics.odu.edu/∼ulmer/experiments/e01020/vdc/vdc.ps (2004). 96
[87] V.L. Rvachev, T.I. Sheiko, V. Shapiro and I. Tsukanov, *On Completeness of RFM Solution Structures*, Computational Mechanics **25**, 305 (2000); http://sal-cnc.me.wisc.edu/publications/completeness.html. 96
[88] R. Roche, http://hallaweb.jlab.org/software/tools/rroche_event_display.tar (2004). 96
[89] J.-M. Laget, private communication (2004). 97
[90] D. Diakonov, V. Petrov and M. Polyakov, Z. Phys. A **359**, 305 (1997). 8, 98, 99
[91] S. Capstick, P. R. Page and W. Roberts, Phys. Lett. B **570**, 185 (2003). 9, 98

5 Hall A Collaboration Member List

Bryon Anderson	*Kent State University*
Mattias Andersson	*University of Lund, Lund*
Konrad A. Aniol	*California State University*
John Annand	*University of Glasgow, Glasgow*
David S. Armstrong	*College of William and Mary*
John Arrington	*Argonne National Laboratory*
Todd Averett	*College of William and Mary*
Maud Baylac	*Jefferson Laboratory*
Elizabeth Beise	*University of Maryland*
Fatiha Benmokhtar	*Rutgers, The State University of New Jersey*
Jacques Berthot	*Université Blaise Pascal, Clermont-Ferrand*
Pierre Bertin	*Université Blaise Pascal, Clermont-Ferrand*
Bill Bertozzi	*Massachusetts Institute of Technology*
Louis Bimbot	*Institut de Physique Nucléaire, Orsay*
Tim Black	*Massachusetts Institute of Technology*
Werner Boeglin	*Florida International University*
Alexander Borissov	*University of Glasgow, Glasgow*
Ed Brash	*Christopher Newport University*
Vincent Breton	*Université Blaise Pascal, Clermont-Ferrand*
Herbert Breuer	*University of Maryland*
Etienne Burtin	*DAPNIA/SPhN, CEA, Saclay*
John Calarco	*University of New Hampshire*
Alexandre Camsonne	*Université Blaise Pascal, Clermont-Ferrand*
Larry Cardman	*Jefferson Laboratory*
Gordon D. Cates	*University of Virginia*
Christian Cavata	*DAPNIA/SPhN, CEA, Saclay*
Zengwei Chai	*Massachusetts Institute of Technology*
George Chang	*University of Maryland*
Ting Chang	*University of Illinois*
Nicholas Chant	*University of Maryland*
Jian-Ping Chen	*Jefferson Laboratory*
Seonho Choi	*Temple University*
Eugene Chudakov	*Jefferson Laboratory*
Steve Churchwell	*Duke University*
Evaristo Cisbani	*INFN/Sezione Sanità, Rome*
Leon Cole	*Hampton University*
Marius Coman	*Florida International University*
Benjamin Crowe	*North Carolina Central University*

Francesco Cusanno	*INFN/Sezione Sanità, Rome*
Dan Dale	*University of Kentucky*
Areg Danagoulian	*University of Illinois*
Nathalie Degrande	*Gent State University, Gent*
Raffaele De Leo	*INFN/Sezione Bari, Bari*
Alexandre Deur	*University of Virginia*
Nicole d'Hose	*DAPNIA/SPhN, CEA, Saclay*
Rachele di Salvo	*INFN/Sezione Roma2, Rome*
Pibero Djawotho	*College of William and Mary*
Frank Dohrmann	*Argonne National Laboratory*
Jean-Eric Ducret	*DAPNIA/SPhN, CEA, Saclay*
Dipangkar Dutta	*Massachusetts Institute of Technology*
Kim Egiyan	*Yerevan Physics Institute, Yerevan*
Martin B. Epstein	*California State University*
Stephanie Escoffier	*DAPNIA/SPhN, CEA, Saclay*
Robert Feuerbach	*Jefferson Lab*
Mike Finn	*College of William and Mary*
Kevin Fissum	*University of Lund, Lund*
Helene Fonvieille	*Université Blaise Pascal, Clermont-Ferrand*
Bernard Frois	*DAPNIA/SPhN, CEA, Saclay*
Salvatore Frullani	*INFN/Sezione Sanità, Rome*
Haiyan Gao	*Duke University*
Franco Garibaldi	*INFN/Sezione Sanità, Rome*
Ashot Gasparian	*Hampton University*
Olivier Gayou	*Massachusetts Institute of Technology*
Shalev Gilad	*Massachusetts Institute of Technology*
Ron Gilman	*Rutgers, The State University of New Jersey*
Alexander Glamazdin	*Kharkov Institute of Physics and Technology, Kharkov*
Charles Glashausser	*Rutgers, The State University of New Jersey*
Javier Gomez	*Jefferson Laboratory*
Victor Gorbenko	*Kharkov Institute of Physics and Technology, Kharkov*
Tim Gorringe	*University of Kentucky*
Keith Griffioen	*College of William and Mary*
David Hamilton	*University of Glasgow, Glasgow*
Ole Hansen	*Jefferson Laboratory*
David Hayes	*Old Dominion University*
Bill Hersman	*University of New Hampshire*
Doug Higinbotham	*Jefferson Laboratory*
Wendy Hinton	*Old Dominion University*
Richard Holmes	*Syracuse University*
Harry Holmgren	*University of Maryland*

Maurik Holtrop	*University of New Hampshire*
Edik Hovhannisyan	*Yerevan Physics Institute, Yerevan*
Calvin Howell	*Duke University*
Garth Huber	*University of Regina, Regina*
Charles Hyde-Wright	*Old Dominion University*
Hassan Ibrahim	*Old Dominion University*
Ru Igarashi	*University of Saskatchewan, Saskatoon*
Sebastian Incerti	*Temple University*
Mauro Iodice	*INFN/Sezione Sanità, Rome*
Riccardo Iommi	*INFN/Sezione Sanità, Rome*
Dave Ireland	*University of Glasgow, Glasgow*
Kees de Jager	*Jefferson Laboratory*
Stephanie Jaminion	*Université Blaise Pascal, Clermont-Ferrand*
Steffen Jensen	*California Institute of Technology*
Xiaodong Jiang	*Rutgers, The State University of New Jersey*
Yi Jiang	*USTC, Hefei*
Cathleen Jones	*California Institute of Technology*
Mark K. Jones	*Jefferson Laboratory*
Seigo Kato	*Yamagata University, Yamagata*
Mina Katramatou	*Kent State University*
Lisa Kaufman	*University of Massachusetts*
James Kellie	*University of Glasgow, Glasgow*
James Kelly	*University of Maryland*
Sophie Kerhoas	*DAPNIA/SPhN, CEA, Saclay*
Armen Ketikyan	*Yerevan Physics Institute, Yerevan*
Kouichi Kino	*Tohoku University, Sendai*
Norm Kolb	*University of Saskatchewan, Saskatoon*
Ioannis Kominis	*Princeton University*
Wolfgang Korsch	*University of Kentucky*
Serge Kox	*Laboratoire de Physique Subatomique et de Cosmologie, Grenoble*
Alexander Kozlov	*University of Regina, Regina*
Kevin Kramer	*College of William and Mary*
Laird Kramer	*Florida International University*
Krishna S. Kumar	*University of Massachusetts*
Gerfried Kumbartzki	*Rutgers, The State University of New Jersey*
Geraud Lavessiere	*Université Blaise Pascal, Clermont-Ferrand*
John LeRose	*Jefferson Laboratory*
Mark Leuschner	*University of New Hampshire*
David Lhuillier	*DAPNIA/SPhN, CEA, Saclay*
Richard Lindgren	*University of Virginia*
Ken Livingston	*University of Glasgow, Glasgow*

Nilanga Liyanage	*University of Virginia*
George Lolos	*University of Regina*
Hai-Jiang Lu	*USTC, Hefei*
Robert Lourie	*Renaissance Technology*
Bin Ma	*Massachusetts Institute of Technology*
Richard Madey	*Kent State University*
Kazushige Maeda	*Tohoku University, Sendai*
Vahe Mamyan	*Yerevan Physics Institute, Yerevan*
Mark Manley	*Kent State University*
Demetrius Margaziotis	*California State University*
Pete Markowitz	*Florida International University*
Jacques Marroncle	*DAPNIA/SPhN, CEA, Saclay*
Jacques Martino	*SUBATECH, IN2P3, Nantes*
Samvel Mayilyan	*Yerevan Physics Institute, Yerevan*
Kathy McCormick	*PNNL*
David Meekins	*Jefferson Laboratory*
Zein-Eddine Meziani	*Temple University*
Bob Michaels	*Jefferson Laboratory*
Brian Milbrath	*Eastern Kentucky University*
Wilson Miller	*University of Virginia*
Joseph Mitchell	*Renaissance Technology*
Bryan Moffit	*College of William and Mary*
Peter Monaghan	*Massachusetts Institute of Technology*
Jean Mougey	*Laboratoire de Physique Subatomique et de Cosmologie, Grenoble*
Pierre Moussiegt	*Laboratoire de Physique Subatomique et de Cosmologie, Grenoble*
Carlos Munoz-Camacho	*DAPNIA/SPhN, CEA, Saclay*
Sirish Nanda	*Jefferson Laboratory*
Alan Nathan	*University of Illinois*
Vladimir Nelyubin	*St. Petersburg Nuclear Physics Institute, Gatchina*
Damien Neyret	*DAPNIA/SPhN, CEA, Saclay*
Dima Nikolenko	*Budker Institute of Nuclear Physics, Novosibirsk*
Blaine Norum	*University of Virginia*
Zisis Papandreou	*University of Regina*
Kent Paschke	*University of Massachusetts*
Emilie Penel-Notarris	*Laboratoire de Physique Subatomique et de Cosmologie, Grenoble*
J.C. Peng	*University of Illinois*
Lubomir Penchev	*College of William and Mary*
Charles Perdrisat	*College of William and Mary*
Gerassimos G. Petratos	*Kent State University*
Artush Petrosyan	*Yerevan Physics Institute, Yerevan*
Eli Piasezky	*Tel Aviv University, Tel Aviv*

Stephane Platchkov	*DAPNIA/SPhN, CEA, Saclay*
Roman Pomatsalyuk	*Kharkov Institute of Physics and Technology, Kharkov*
Dan Protopopescu	*University of Glasgow, Glasgow*
Vina Punjabi	*Norfolk State University*
Thierry Pussieux	*DAPNIA/SPhN, CEA, Saclay*
Issam Qattan	*North-Western University*
Gilles Quéméner	*Laboratoire de Physique Subatomique et de Cosmologie, Grenoble*
Igor Rachek	*Budker Institute of Nuclear Physics, Novosibirsk*
Ronald Ransome	*Rutgers, The State University of New Jersey*
Brian Raue	*Florida International University*
Juerg Reinhold	*Florida International University*
Bodo Reitz	*Jefferson Laboratory*
Yves Roblin	*Jefferson Laboratory*
Rikki Roché	*Florida State University*
Mike Roedelbronn	*University of Illinois*
Oscar Rondon	*University of Virginia*
Guenther Rosner	*University of Glasgow, Glasgow*
David Rowntree	*Massachusetts Institute of Technology*
Gary Rutledge	*TRIUMF*
Marat Rvachev	*Massachusetts Institute of Technology*
Franck Sabatie	*DAPNIA/SPhN, CEA, Saclay*
Arun Saha	*Jefferson Laboratory*
Teijiro Saito	*Tohoku University, Sendai*
Adam J. Sarty	*Saint Mary's University*
Ralph Segel	*Northwestern University*
Andrei Semenov	*Kent State University*
Albert Shahinyan	*Yerevan Physics Institute, Yerevan*
Simon Sirca	*Massachusetts Institute of Technology*
Karl Slifer	*Temple University*
Timothy Smith	*University of New Hampshire*
Patricia Solvignon	*Temple University*
Pavel Sorokin	*Kharkov State University, Kharkov*
Paul A. Souder	*Syracuse University*
Steffen Strauch	*George Washington University*
Riad Suleiman	*Massachusetts Institute of Technology*
Vincent Sulkovsky	*College of William and Mary*
Jeff Templon	*NIKHEF, Amsterdam*
Tatsuo Terasawa	*Tohoku University, Terasawa*
Luminita Todor	*Carnegie Mellon University*
H. Tsubota	*Tohoku University, Sendai*
Hiroaki Ueno	*Yamagata University, Yamagata*

Paul E. Ulmer	*Old Dominion University*
Guido Urciuoli	*INFN/Sezione Sanità, Rome*
Antonin Vacheret	*DAPNIA/SPhN, CEA, Saclay*
Luc Van de Hoorebeke	*Gent State University, Gent*
Robert Van de Vyver	*Gent State University, Gent*
Pascal Vernin	*DAPNIA/SPhN, CEA, Saclay*
Branislav Vlahovic	*North Carolina Central University*
Hakob Voskanyan	*Yerevan Physics Institute, Yerevan*
Eric Voutier	*Laboratoire de Physique Subatomique et de Cosmologie, Grenoble*
Richard Walter	*Duke University*
Kebin Wang	*University of Virginia*
John Watson	*Kent State University*
Dan Watts	*University of Glasgow*
Larry Weinstein	*Old Dominion University*
Richard Wilson	*Harvard University*
Krishni Wijesooriya	*Argonne National Laboratory*
Bogdan Wojtsekhowski	*Jefferson Laboratory*
Hong Xiang	*Massachusetts Institute of Technology*
Feng Xiong	*Massachusetts Institute of Technology*
Wang Xu	*Massachusetts Institute of Technology*
Yunxiu Ye	*USTC, Hefei*
Jianguo Zhao	*General Electric*
Xiaochao Zheng	*Massachusetts Institute of Technology*
Shuhua Zhou	*China Atomic Energy Institute, Beijing*
Zilu Zhou	*Massachusetts Institute of Technology*
Jindong Zhu	*Massachusetts Institute of Technology*
Lingyan Zhu	*Massachusetts Institute of Technology*
Xiaofeng Zhu	*College of William and Mary*
Piotr Zolnierczuk	*University of Kentucky*

6 Publications

- *Basic Instrumentation for Hall A at Jefferson Lab*, J. Alcorn *et al.*, Nucl. Instrum. Meth. A **522**, 294 (2004).
- *Measurement of the generalized polarizabilities of the proton in virtual Compton scattering at Q^2 = 0.92 GeV^2 and 1.76 GeV^2*, G. Laveissiere *et al.*, Phys. Rev. Lett. **93**, 122001 (2004).
- *The dynamics of the quasielastic ^{16}O(e,e'p) reaction at Q^2 = 0.8 GeV^2*, K. G. Fissum *et al.*, Phys. Rev. C **70**, 034606 (2004).
- *Precision measurement of the neutron spin asymmetry A_n^1 and spin-flavor decomposition in the valence quark region*, X. Zheng *et al.*, Phys. Rev. Lett. **92**, 012004 (2004).
- *Backward electroproduction of π^0 mesons on protons in the region of nucleon resonances*, G. Laveissiere *et al.*, Phys. Rev. C **69**, 045203 (2004).
- *Measurement of the generalized forward spin polarizabilities of the neutron*, M. Amarian *et al.* Phys. Rev. Lett. **93**, 152301 (2004).
- *Parity-violating electroweak asymmetry in $\vec{e}, p$ scattering*, K. A. Aniol *et al.* [HAPPEX Collaboration], Phys. Rev. C **69**, 065501 (2004).
- *Q^2 evolution of the neutron spin structure moments using a ^3He target*, M. Amarian *et al.*, Phys. Rev. Lett. **92**, 022301 (2004).
- *Precision measurement of the neutron spin asymmetries and spin-dependent structure functions in the valence quark region*, X. Zheng *et al.*, Phys. Rev. C **70**, 065207 (2004).
- *Experimental determination of the evolution of the Bjorken integral at low Q^2*, A. Deur *et al.*, Phys. Rev. Lett. **93**, 212001 (2004).
- *Electromagnetic form factors of the nucleon and Compton scattering*, Charles Hyde-Wright and Kees de Jager, Annu. Rev. Nucl. Part. Sci. **54**, 216 (2004).

7 Theses

i. Experiment E89-044 on the Quasielastic ^{3}He(e,$e'p$) Reaction at Jefferson Laboratory
Emilie Penel-Nottaris, Laboratoire de Physique Subatomique et de Cosmologie, Grenoble, Jul. 2004.

ii. Spin structure of ^{3}He and of the neutron at low Q^2, A measurement of the extended GDH intergral and the Burkhardt-Cottingham sum rule
Karl Slifer, Temple University, Aug 2004.

iii. Measurement of the ^{3}He(e,$e'p$)pn Reaction at High Missing Energies and Momenta
Fatiha Benmokhtar, Rutgers University, Oct 2004.

iv. Polarisation Transfer in Proton Compton Scattering at High Momentum Transfer
David Hamilton, University of Glasgow, Nov. 2004.